



HAL
open science

Quantitative X-ray tomography

Éric Maire, Philip John Withers

► **To cite this version:**

Éric Maire, Philip John Withers. Quantitative X-ray tomography. *International Materials Reviews*, 2014, 59 (1), pp.1-43. 10.1179/1743280413y.0000000023 . hal-01538208

HAL Id: hal-01538208

<https://hal.science/hal-01538208>

Submitted on 17 Jan 2019

HAL is a multi-disciplinary open access archive for the deposit and dissemination of scientific research documents, whether they are published or not. The documents may come from teaching and research institutions in France or abroad, or from public or private research centers.

L'archive ouverte pluridisciplinaire **HAL**, est destinée au dépôt et à la diffusion de documents scientifiques de niveau recherche, publiés ou non, émanant des établissements d'enseignement et de recherche français ou étrangers, des laboratoires publics ou privés.

Quantitative X-ray tomography

E. Maire*¹ and P. J. Withers²

X-ray computer tomography (CT) is fast becoming an accepted tool within the materials science community for the acquisition of 3D images. Here the authors review the current state of the art as CT transforms from a qualitative diagnostic tool to a quantitative one. Our review considers first the image acquisition process, including the use of iterative reconstruction strategies suited to specific segmentation tasks and emerging methods that provide more insight (e.g. fast and high resolution imaging, crystallite (grain) imaging) than conventional attenuation based tomography. Methods and shortcomings of CT are examined for the quantification of 3D volumetric data to extract key topological parameters such as phase fractions, phase contiguity, and damage levels as well as density variations. As a non-destructive technique, CT is an ideal means of following structural development over time via time lapse sequences of 3D images (sometimes called 3D movies or 4D imaging). This includes information needed to optimise manufacturing processes, for example sintering or solidification, or to highlight the proclivity of specific degradation processes under service conditions, such as intergranular corrosion or fatigue crack growth. Besides the repeated application of static 3D image quantification to track such changes, digital volume correlation (DVC) and particle tracking (PT) methods are enabling the mapping of deformation in 3D over time. Finally the use of CT images is considered as the starting point for numerical modelling based on realistic microstructures, for example to predict flow through porous materials, the crystalline deformation of polycrystalline aggregates or the mechanical properties of composite materials.

Keywords: Three dimensional metrology, X-ray microscopy, Quantitative metallography, Digital image correlation (DIC), Image based modelling, Particle tracking, Diffraction imaging, Damage accumulation, Self-healing

Introduction

X-ray computer tomography (CT) has seen a period of rapid growth over the last 15 years with considerable improvements in spatial resolution and image reconstruction times such that it is now a commonly available tool within materials labs. Indeed, two excellent reviews have been published in IMR on the topic^{1,2} together with a number of books.³⁻⁵ Initially, it was used predominantly as a means of acquiring 3D images from which diagnoses could be made based on visual judgement. More recently, there has been an increasing move towards extracting key materials science parameters from these images, through quantitative analysis. This has radically improved the level of information that can be gleaned from 3D imaging. In some cases this is focussed on the quantitative characterisation of microstructure from a single 3D volume. In other cases comparisons are made between successive 3D images in

order to quantify structural evolution in materials science and to support micromechanics experiments and modelling. This review will attempt to outline the major strands of quantitative analysis that are beginning to emerge for both these aspects.

The first part of this review examines recent imaging advances that, we believe, have significantly increased the power of the method for quantifying the evolution of materials, many of which have not received much attention to date. For example, it is now feasible to achieve spatial resolutions below 100 nm or, largely due to advances in synchrotron X-ray tomography, to acquire thousands of projections (radiographs) sufficiently quickly to obtain many 3D images per second. Further, one can obtain high resolution images from specific regions of interest (RoI), even from within large objects by local tomography. It is also possible to go beyond attenuation imaging, for example to reveal the crystallographic orientation in 3D, thanks to methods such as 3D X-ray diffraction microscopy (3DXRD) and diffraction contrast tomography (DCT), or to image spatial variations in chemistry by X-ray Absorption Near Edge Structure (XANES) imaging⁶ or colour imaging.⁷

The review then focuses on the static analysis of 3D volumes as a basis for the quantitative characterisation

¹Université de Lyon, INSA-Lyon, MATEIS, CNRS UMR5510, F-69621 Villeurbanne, France

²Manchester X-ray Imaging Facility, School of Materials, Manchester, M13 9PL, UK and also The Research Complex at Harwell, Rutherford Appleton Laboratory, Didcot, Oxfordshire OX11 0FA, UK

*Corresponding author, email Eric.Maire@insa-lyon.fr

of many aspects of materials microstructure using illustrative examples from the literature. In such cases it is important to identify the added value of 3D images over conventional quantitative metallography based on 2D sections. Good examples where 3D images are invaluable include cases where the samples are too fragile to be sectioned (e.g. powders), or too valuable (e.g. art treasures or archival materials), or where 2D analysis is inadequate, for example for the quantification of the connectivity and/or the tortuosity of the different phases in the material (e.g. when considering the potential for fluid flow through porous solids).

Increasingly, X-ray tomography is being used to follow the evolution of a microstructure under controlled environmental conditions (load, temperature and corrosive environment) through the collection of time lapse sequences to create 3D movies, a technique sometimes called 4D (3D plus time) imaging. Here the possibilities for quantification expand beyond microstructural quantification into dynamic quantities such as flow, deformation mapping and damage accumulation. Again the review will focus on those studies where this has been used to obtain quantitative information, for example to map displacements or strain fields induced by loading. Currently this is done either by tracking the movement of individual features or objects, or by the digital correlation of the full grey level signature of each image onto its predecessor, or some reference image. Both approaches give a measurement of the heterogeneous strain field in the sample.

Finally, the 3D images obtained by X-ray tomography can be used to extract a faithful representation of the geometrical structure, phase or grain microstructure for numerical modelling purposes by so-called image based modelling. In the case of time lapse (4D) imaging it can be used to validate numerical predictions of structural or microstructural evolution.

Emerging avenues in tomographic imaging

The word tomography derives from the Greek 'tomos', to slice or section, and 'graph', an image or representation. While experimental practice, in materials science at least, has mostly moved away from using a fan beam to collect a cross-sectional slice through a body, to collecting full 3D volumes using cone or parallel beam illumination, we have yet to define a word for a 3D volume. Consequently, the word 'tomogram' will be used here to refer to a 3D virtual volume reconstructed from hundreds or thousands of 2D images (commonly referred to as radiographs in medicine and more generally as projections). Such 3D attenuation based tomography has been extensively reviewed elsewhere.^{1,2,4} In this section, we focus on new techniques and methods that make X-ray CT increasingly well suited to quantitative analysis.

Phase imaging

Phase imaging⁸ has been reviewed in detail elsewhere.² This imaging mode is especially useful as a way of increasing the contrast between objects that attenuate the beam similarly, for example soft solids and fossils. Provided the effects of phase contrast are not too pronounced, the enhanced edge contrast means that phase images can be much easier to process and segment. This enables one to retrieve quantitative information on

low contrast microstructures that would be impossible to achieve with attenuation contrast. Extensive phase contrast can lead to additional features in the image that cannot be understood unless phase retrieval approaches are employed. Various phase contrast methods are described below; the relative merits of the first three of these are discussed by Diemoz *et al.*⁹

Propagation phase contrast: Traditionally used for propagation (or in-line) phase contrast, it exploits the Fresnel diffraction of X-rays to enhance the visibility of edges and boundaries within an object. Phase retrieval procedures normally require that images of the same sample are recorded at multiple sample to detector distances, with the extent of phase contrast increasing with distance.^{10,11} Rather than take multiple images, the trend for retrieval of the phase content is towards a more frequent use of the Paganin solution¹² and the associated unsharp mask filtering.¹³ This solution, based on a specific filtering of the projections, is less time consuming because it allows one to reconstruct the phase of the object from a set of projections collected at a single distance. While the highly coherent beams characteristic of long synchrotron beamlines makes them well suited to phase contrast imaging,¹⁴ the technique is not restricted to synchrotron sources. Indeed it has proved invaluable in imaging fossils using lab sources.^{15,16} However because the incident beam is polychromatic, phase retrieval is not as effective as for synchrotron X-ray imaging.¹⁷

Analyser-based diffraction enhanced imaging^{18,19} involves the reflection of the transmitted beam from a Bragg crystal which acts as an angular filter converting refractive effects caused by the object into intensity effects in the detector plane. Early work focussed on the imaging of pellets used in thermonuclear fusion experiments.^{20,21}

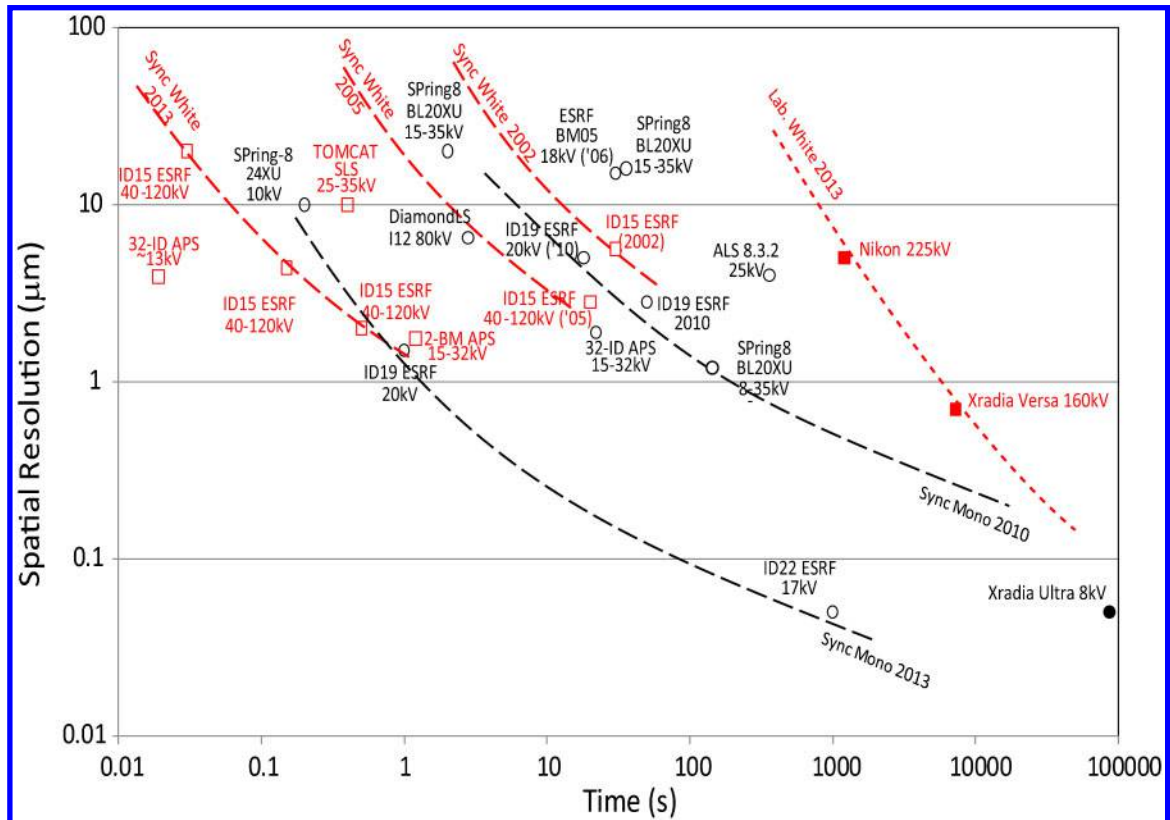
Grating interferometry^{22,23} is a rapidly emerging area for both lab^{23,24} and synchrotron sources²⁵ whereby one or more gratings act as wave-front modulators and/or analyzers. While rather slow because one of the gratings must be scanned, it has the advantage that it can be employed on low brightness sources.

Zernike contrast is one of the oldest techniques for generating phase contrast being taken directly from optical light microscopy whereby a phase shift between diffracted and undiffracted light from a sample is introduced by a phase shifter. It can be employed on X-ray microscopes both in the lab²⁶ and at the synchrotron^{27,28} usually for nanotomography.

Coherent diffractive imaging (CDI) The recent drive towards ultra-high resolution imaging has finally led to CDI, which uses a highly coherent beam to obtain diffraction patterns from very small samples enabling high spatial resolution images by computationally converting the diffraction pattern into an image rather than with a lens, for example to image the 50 nm wide twins in gold nanocrystals.²⁹ While very high resolution images have been obtained so far, it has not been practical to computationally reconstruct complex objects and structures such that this remains something of a niche method at present.

Improvement in temporal resolution

The move to faster and faster 3D imaging frame rates is opening up a whole avenue of imaging applications that cannot be studied easily by other means. In experimental X-ray tomography a basic principle is that the sample



1 Plot showing the historical development of fast X-ray tomography. In many cases the spatial resolution is not cited and an estimated resolution twice the pixel size has been used. Open symbols denote synchrotron sources, while filled ones represent laboratory sources, red squares denote white beam and black circles monochromatic beam scanners.^{26,31–42} The database on which this figure is based can be added to and is available in Ref. 43

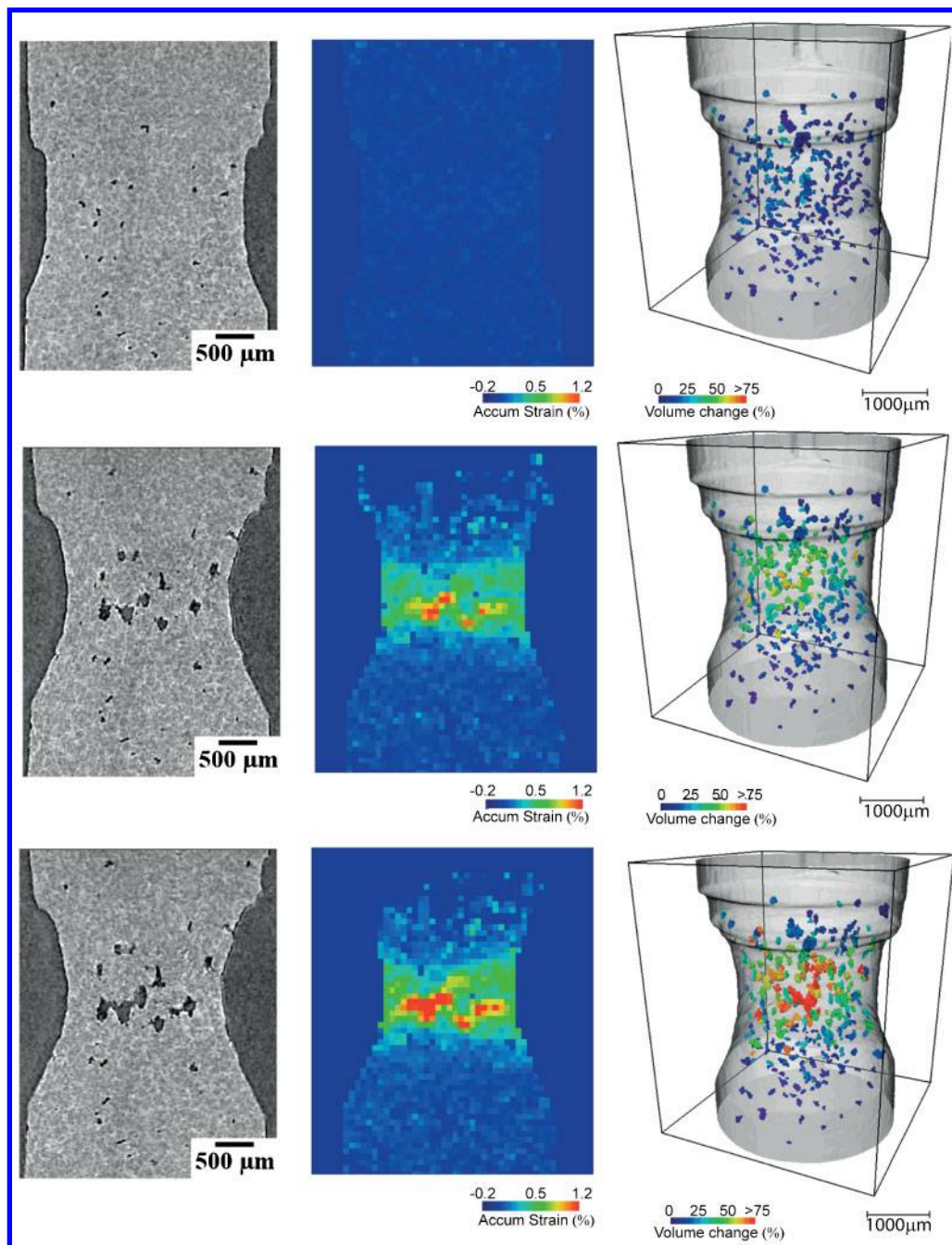
should remain unchanged during the acquisition of the projections to enable a sound reconstruction (although our capability to reconstruct images that move during acquisition is improving, see ‘Novel reconstruction strategies’ section). Until recently, it was not possible to acquire a scan in less than 5 min, even at intense synchrotron sources (see Fig. 1). When studying fatigue crack propagation or microstructural changes induced by stress or temperature, for example, it was thus necessary to maintain the loading conditions at a constant level (quasi-static) during the acquisition period, or in the case of a thermal stimulus, to quench the specimen in order to freeze its microstructure. These restrictions precluded evolutionary studies of many interesting structural changes. As Fig. 1 illustrates considerable improvements have been made in recent years, for example by combining high efficiency phosphor screens and fast read-out charge coupled device (CCD) or complementary metal oxide semiconductor (CMOS) detectors with the very intense white (all wavelengths) or pink (part of wavelengths) beams.³⁰ Indeed the flux can be so great that local damage can occur in some instances, especially when imaging with white synchrotron beams.

Long timescale events (days/months): As illustrated by Fig. 1, laboratory sources are typically two orders of magnitude slower than synchrotron sources, but since they are competitive on resolution (see ‘Very high resolution imaging’ section), they are well suited to following structural changes that occur over periods of days or months. Examples range from the degradation of rechargeable batteries during their operating life⁴⁴ to

the metamorphosis of butterflies.⁴⁵ For quantitative work it is important to remember that the accuracy is significantly influenced by the spatial stability of the X-ray focal spot^{46,47} and that a stable position can take up to 2 hours to develop in certain circumstances. Rockett employed a UHV LaB₆ source to circumvent stability issues associated with tungsten sources⁴⁸ specifically for long timescale quantitative studies. Such time varying effects need to be accounted for when quantitatively correlating or comparing images over extended timescales (see ‘Quantifying time lapse CT’ section).

Short timescales (minutes): There are numerous potential applications for imaging at the seconds-to-minutes timescale, for example Babin *et al.*³⁵ applied fast tomography to study the evolution of pores during bread making and showed that a gas cell structure first develops during fermentation. Afterwards, coalescence rapidly prevails leading to a heterogeneous structure. In a similar study Mokso *et al.*³² have studied the dynamics of foam on beer. Pyzalla *et al.*⁴⁹ have coupled *in situ* fast imaging (one tomographic scan per 2 min) with *in situ* diffraction to study the creep deformation of copper samples. Imaging gave access to the evolution of the size of the cavities while diffraction was used to assess crystallographic texture, changes in domain size, dislocation density, and internal stresses. Vagnon *et al.*⁵⁰ employed fast imaging (1 min per scan) to study the deformation of steel powders during sintering.

This timescale is also ideal for following many damage accumulation processes, for instance to identify damage events in real time during the tensile testing of model metal matrix composites (spherical ceramic

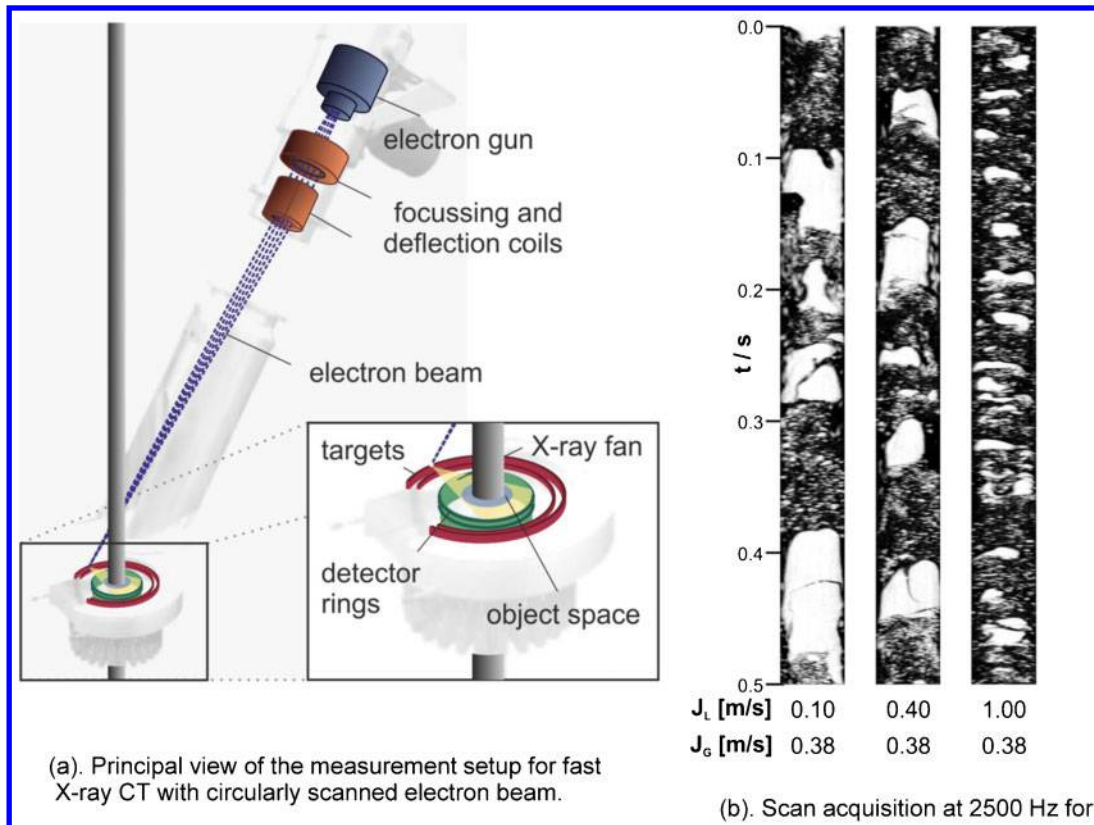


2 Fast imaging acquired during a high temperature tensile test of a semi-solid aluminium alloy. In this example, fast imaging is combined with digital volume correlation and image processing bringing new insights.⁵⁵ *a* A virtual section during the hot tearing of partially solidified metal, *b* the local variation in strain determined by digital volume correlation and *c* the volume change of the voids between steps, which shows the internal growth of the voids in the localised deformation region

particles embedded in aluminium) coupled to acoustic emission measurements.⁵¹ Here the deformation speed was set to a very low value (10^{-5} s^{-1}) to prevent motion blurring of the reconstruction during the acquisition time (40 s). In this slow strain case it was found that continuous acquisition gave the same results, both in terms of imaging and acoustic emission acquisition, as interrupted straining. The same conclusions were drawn by Suery⁵² for the ductile fracture of dual phase steels.

Second timescales: An extensive body of work has exploited fast imaging on the seconds timescale to study the coarsening, melting, solidification, and remelting of semi-solid metals.^{34,36,37,53–55} For example special

thermomechanical rigs have enabled the study of hot tearing, e.g. Terzi *et al.*⁵⁶ and Puncreobutr, Lee *et al.*⁵⁵, which is important for solidification shrinkage during casting. It occurs during the final stages of metal solidification when the solid fraction becomes high, so that liquid is present only as a thin film when the liquid flow necessary to prevent tearing cannot occur. Direct observations of the evolution of hot tearing (Fig. 2*a*) can be correlated with the measurement of the local strain field by digital volume correlation (Fig. 2*b*) between successive images in the sequence and complemented by quantitative measurements of the void volume change (See Fig. 2*c*).⁵⁵ Such *in situ* work has also shown that the



3 **a** Ultrafast electron beam X-ray CT system with two tomography planes and **b** example of imaged water–air two-phase flow. The flow has been imaged at 2500 fps, while the system is capable of a maximum frame rate of 8000 fps. The images show axial cuts through the three-dimensional data sets, where the vertical axis is time (adapted from Ref. 65)

results (e.g. the variation in the measured specific surface) obtained when characterising coarsening using a standard *ex situ* quenching and sectioning procedure are very different to what is observed under real time *in situ* continuous observation of the semi-solid microstructure. This is because significant changes in microstructure occur during quenching so that conclusions drawn based on observation of samples at room temperature can be misleading.³⁶

Recently Deville *et al.*⁵⁷ have studied the solidification of ice crystals in a ceramic aqueous slurry in a process called freeze casting to produce lamellar porous ceramics with tomograms acquired in 1 second and a voxel size in the reconstruction of 1.7 μm . This can provide valuable information from a materials design viewpoint because of the scope for microstructural tailoring via control of the solidification conditions.⁵⁸

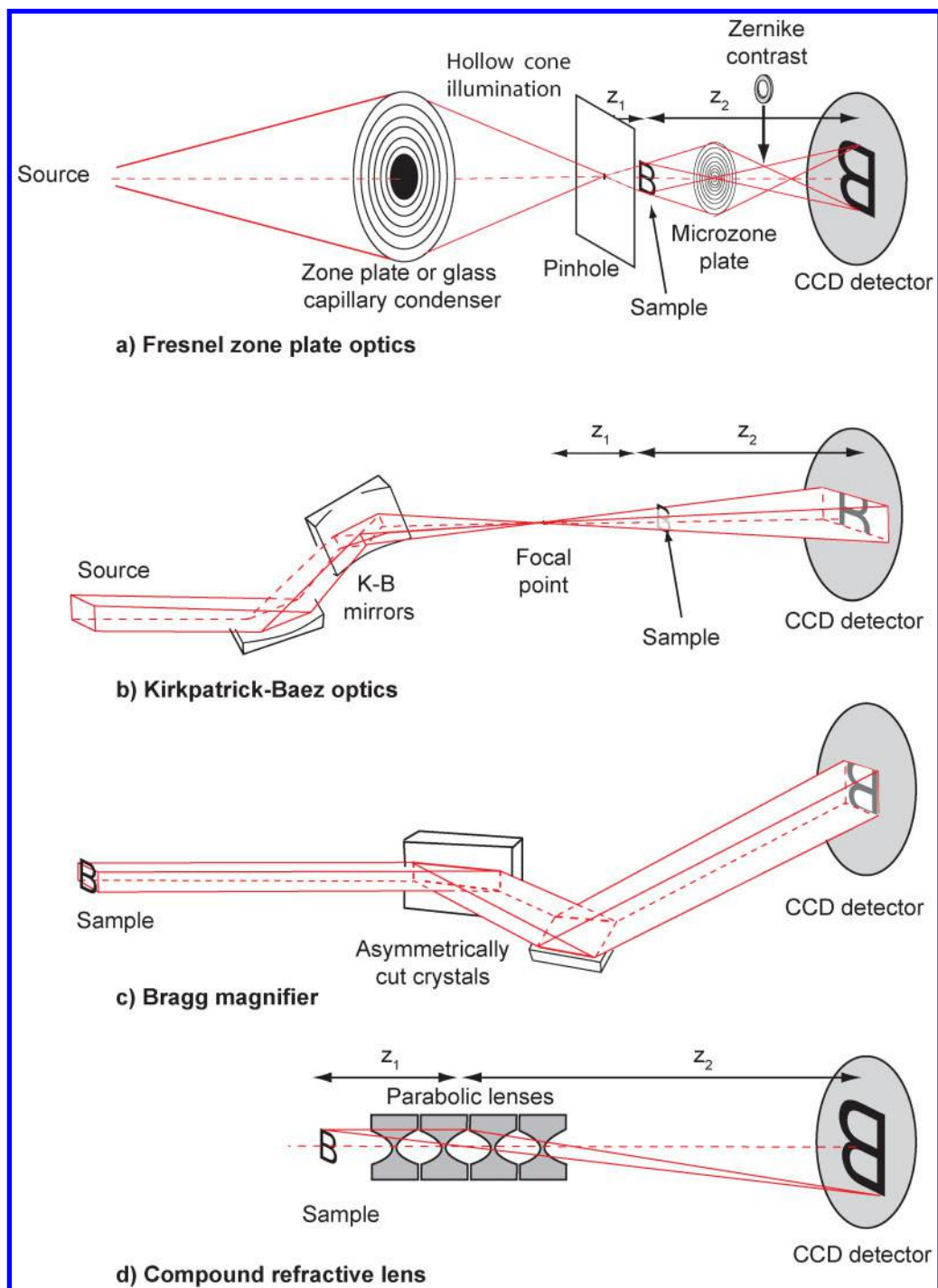
In this frame rate regime most of the work to date has been undertaken at synchrotron sources because of the greater flux. Nevertheless, recent advances in liquid metal lab sources promise to achieve nearly $10\times$ the brilliance of standard X-ray tubes (achieving up to 300 projections per second⁵⁹), which may open up this area to laboratory imaging.

Sub-second timescales: Synchrotron sources can now acquire as many as 270 000 frames per second for radiography with tomographic frame rates moving towards tens per second (Fig. 1). The development of a special ultra-fast laboratory based X-ray scanner capable of acquiring one or two tomographic slices (i.e. not a full 3D tomogram) in one thousandth of a second has also been reported.^{60–62} For this type of ultra-fast device, an electron beam is scanned very

rapidly across a target to form a moving X-ray source used to illuminate a fixed sample in front of a fixed circular line of detectors (see Fig. 3a). If the acquisition is synchronised with the scanning, it is possible to reconstruct tomography slices. In the device demonstrated in Ref. 60, the electron beam is scanned on a linear target. Acquisition is only partial and iterative algebraic reconstruction techniques (ART) are used for the reconstruction. The final image suffers from standard ‘partial angular view’ artefacts but the acquisition of single slices is nevertheless operated at a 1 kHz frequency. In Ref. 61, the images are of better quality as the acquisition arrangement is able to span 360° . The acquisition is again ultrafast, allowing the authors to study bubbles in a liquid for an air–water flow in a vertical pipe. In a new example, kindly provided for the present review, an acquisition speed of 2.5 kHz is reported while the system is potentially able to operate at 8 kHz (see Fig. 3b). In fact a similar method was developed as long ago as the 1990s to undertake fast medical imaging⁶³ and a 3D scanner for airport luggage has just been commercialised.⁶⁴ In this case, up to 480 frames per second are collected with over 700 projection angles and a voxel size of 1 mm for an 800-mm inspection circle. All these lab systems have the advantage that the illumination moves rather than the sample, since the need to rotate the sample can limit the tomographic acquisition speed³² or disturb the process being monitored.

Very high resolution imaging

Until recently micron resolution represented the state of the art. Sub-micron (nano) tomography is now available



4 Lens based systems, often called X-ray microscopes, can achieve sub-micron resolution; *a* Fresnel Zone Plate system, *b* Kirkpatrick–Baez (K–B) optics system, *c* Bragg multiplier system, *d* compound refractive imaging system (adapted from Ref. 66)

using both synchrotron and laboratory sources, although at markedly different acquisition rates (see Fig. 1). For nanotomography, optical elements are often used to focus the beam to a sub-micron point source from which the sample is illuminated as shown in Fig. 4.

The majority of nanotomography experiments to date have either exploited:⁶⁶

- Fresnel zone plates (FZPs)
- Kirkpatrick–Baez (K–B) optics
- Scanning electron microscope (SEM) beams.

Fresnel zone plates: FZPs have been employed for high resolution imaging for many years.⁶⁷ As illustrated in

Fig. 4, for soft X-rays (0.25–1.8 keV), extremely small focal spots can be produced.⁶⁸ Chao *et al.*⁶⁹ have used an overlay nanofabrication technique to make a composite FZP comprising two coarser complementary FZPs aligned to within 2 nm to give an outer zone width of 15 nm achieving a spatial resolution of around 12 nm at 0.815 keV at the Advanced Light Source (ALS), Berkeley. These energies are well suited to biological applications with the K and L edges of many elements including C, N, O, Fe and Al lying in this range. At a magnification of 2500, the field of view was only 10 μm . This in itself is not a serious limitation because at such

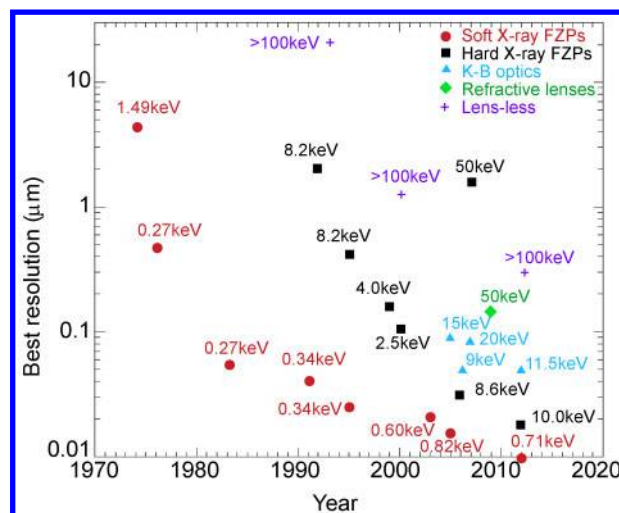
low energies the method is limited to very thin samples anyway, for all but the lightest elements.

With increasingly hard X-rays the difficulty of making FZPs increases. Working in the 8–11 keV energy range opens up the edges of Cu, Zn, Ga, Ge, As, Ta, W, etc., appropriate to the semiconductor industry. Yin *et al.*⁷⁰ used 890-nm thick gold FZPs to image defects in W plugs at 60 nm resolution. These plugs interconnect the different layers of an integrated circuit and ‘keyhole’ defects formed during the electroplating process can cause the breakdown of the circuit. Fresnel zone plates begin to become impractical much above 10 keV though recent advances have seen 30 nm microscopes operate in the 3–30 kV range⁷¹ with stacked FZPs being used right up to 50 keV.⁷² Recently, commercial laboratory systems with sub-50 nm resolution have become available based on FZPs using Cu anode (8 keV) X-rays.⁷³

In view of the fact that it can take as long as a few minutes to acquire each very high resolution image, such tomographic datasets generally comprise only 50–200 radiographs. As the filtered back-projection reconstruction method does not perform well with such coarse angular spacing, algebraic reconstruction techniques (ART) are typically used (see ‘Novel reconstruction strategies’ section). Given that the exposure time is inversely proportional to the fourth power of the spatial resolution, and noting that their 30-nm FZP system takes minutes to acquire a single image, Yun *et al.*⁷⁴ suggest that X-ray tomography at resolutions significantly better than 30 nm is likely to be confined to synchrotron sources unless new lab. X-ray sources with greater brightness can be developed.

Kirkpatrick–Baez mirrors: FZPs become increasingly difficult to manufacture for X-rays above 8 keV. This has led to a number of harder X-ray microscopes based on K–B optics (see Fig. 4) including a zoom microscope capable of 90 nm resolution working at 20.5 keV using K–B mirrors⁷⁵ and a 50-nm microscope operating at 9 keV.⁷⁶ Harder X-rays are particularly well suited to the study of metals and matrix composites. Requena *et al.* used 17.5 keV for Al-based systems and 29 keV for Ti systems⁷⁷ at around 100 nm.

Electron microscope optics: Horn and Waltinger⁷⁸ were perhaps the first to realise that a SEM could be used for X-ray projection microscopy exploiting the highly focussed spot formed by the electron beam. With the arrival of field emission gun sources and improvements in detector technology, the method can come close to the capability of the high performance FZP X-ray microscopes, but at much more modest investment and greater accessibility. The spatial resolution and X-ray flux is dependent upon the choice of target (e.g. Au, Ag, Ta and Ti). The target determines the interaction volume, as well as the X-ray generating efficiency (increases with atomic number). By choosing targets such as Ag (or Ti) it is possible to obtain essentially monochromatic X-rays exploiting the 2.9 keV L_{α} (or 4.5 keV K_{α}) characteristic line. The thinner the target foil (<1 μm) the smaller the electron interaction volume and hence the effective source size. Strong phase contrast has been observed in images collected in this way⁷⁹ and a resolution better than 60 nm has been reported.⁸⁰ Burnett *et al.*⁸¹ have combined non-destructive in-SEM X-ray tomography with destructive serial section FIB tomography to provide both time and



5 Landmark achievements in focussing for soft Fresnel zone plates (FZPs),^{69,82–89} hard FZPs,^{72,89–94} Kirkpatrick–Baez (K–B) optics,^{75,76,95,96} refractive compound lenses⁹⁷ and lens-less projection systems (building on the figure adapted from Ref. 98)

high spatial resolution grain boundary information to study intergranular corrosion in Al alloys, coining the term ‘correlative tomography’. This combination of 3D imaging modes has considerable potential either to bridge scales or to provide complementary information.

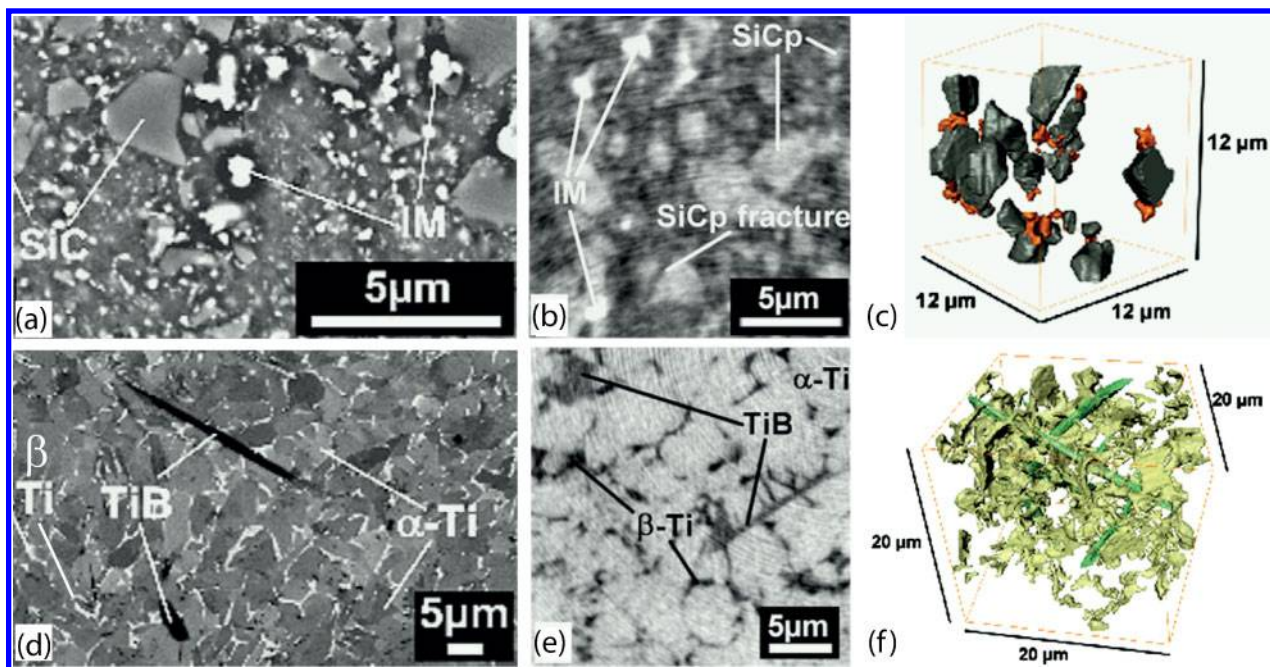
Figure 5 summarises the resolution achieved using all these systems in the last five decades.

Nanotomography is beginning to have a very significant impact on materials science quantifying both materials fabrication and degradation processes. It helps quantify void nucleation and growth,⁹⁹ porosity and pore connectivity,^{100,101} metal^{77,102} (Fig. 6) and polymer¹⁰³ composite microstructures, fuel cells,^{104–108} multiphase alloys,^{109,110} self-healing materials,¹¹¹ and corrosion.¹¹² In the context of nanotomography the field of view is usually around 1000 \times the spatial resolution, which means that nanotomography is often synonymous with very small samples (see ‘Local tomography and lamino-graphy’ section), presenting both statistical sampling and engineering relevance issues, see ‘Caveats and cautions’ section.

Crystal grain imaging

In crystalline solids, the microstructure is often of key importance, influencing a wide range of material properties, including strength, toughness and corrosion resistance. For that reason, understanding and controlling the structure and evolution of grain boundaries is one of the central tasks of materials science today. This has led to the rapid emergence of electron back scattered diffraction (EBSD) analysis, providing detailed 2D maps of surface grain orientation.

While conventional absorption contrast cannot delineate crystal grains, new synchrotron X-ray techniques have recently opened the way to the non-destructive 3D imaging of grain structure. A number of methods have been developed, most notably one termed 3DXRD at the European Synchrotron radiation facility (ESRF), in collaboration with the Risø National Lab¹¹³ and another at the Applied Photon Source (APS).¹¹⁴



6 (Top) 2124 Al/25% SiC particle composite and (bottom) Ti64/5% TiB whisker metal matrix composites. Compared to back scatter electron images taken in the scanning electron microscope (SEM) (left), nanotomography images (centre) are of low resolution (100 nm) despite being at the current limits of X-ray tomography, however they do allow the 3D analysis of the spatial relationships (right) between the Fe–Cu intermetallics (orange) and the SiC reinforcement (grey), and the TiB needles (green) and irregularly shaped β grains (yellow) for the Al/SiC and Ti/TiB composites, respectively,⁷⁷ not so apparent from the 2D SEM images

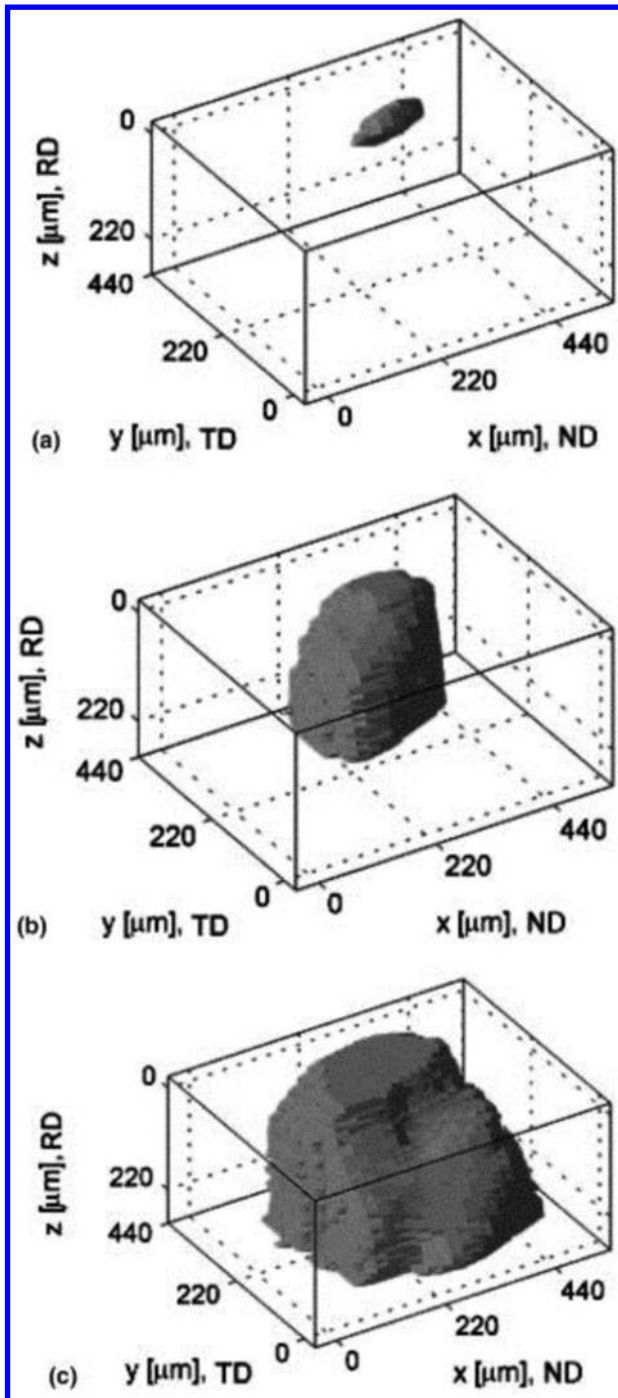
In the former a small, usually letter-box shaped, monochromatic beam is sent through a sample and, as in absorption tomography, the sample is rotated around an axis perpendicular to the beam. Each irradiated grain diffracts part of the incident beam. These diffracted spots are recorded by an appropriate detector. The experiment is repeated at three increasing distances between the sample and the detector so as to geometrically backtrack each spot to provide the position, shape and orientation of every diffracting grain. Such instruments have been used for mapping grains,^{115–117} for studying lattice rotation during plastic deformation,^{118,119} phase changes,¹²⁰ the nanostructure of materials¹²¹ and for analysing recrystallization^{122–131} as shown in Fig. 7.¹³² In a variant, only a far field detector is used so that rather than doing real space imaging, only the centre of mass positions, relative volumes, mean orientations and full stress tensors for each grain within the illuminated volume is monitored. This was first achieved for a rather limited number of grains.^{133–135} Recent progress has made possible a mapping of the stress field in a representative volume within the bulk of a polycrystalline sample using the individual grains as probes.^{136–139}

In the latter a second technique used at the APS synchrotron,¹⁴⁰ a flat beam irradiates a slice of the sample and the diffraction pattern acquired at several distances. It involves a different approach in terms of reconstruction named forward modelling reconstruction (FMR). In this approach, the experiment is modelled in the computer. The irradiated sample plane is meshed with equilateral triangles and, in each triangle, a fundamental zone of crystal orientations is ‘searched’ so as to generate Bragg scattering that optimally overlaps that seen in the measurement. This procedure is computer intensive but gives robust results including in the case of deformed

grains,^{140–144} for studying lattice rotation during plastic deformation^{118,119} and for mapping local strains.¹⁴⁵ Figure 8 shows a slice reconstructed at different strain levels using this method.

A third variant capable of providing grain maps is called DCT.^{147–150} The set-up is rather similar to the one used for absorption or phase contrast tomography (PCT), the main difference being that a standard wide field imaging detector is used to acquire both the X-rays transmitted through the sample, but also those diffracted to wide angle by the grains currently satisfying the Bragg condition for a given angular rotation. Just as for absorption tomography, the sample is rotated around a vertical axis parallel to the detector. The rotation is achieved in very small increments to capture all the Bragg conditions. During a 360° rotation in 0.1° increments, each grain diffracts for about 10 angular positions. At these positions, the contribution of the grain falls in the direct image leaving a dark region because the X-rays are diffracted away and a corresponding wide field bright spot. From all the dark and bright spots the shape of each grain from this small number of shades can be reconstructed. The analysis of Friedel pairs of these diffraction spots allows one to determine the crystallographic orientation of the grains in the sample.^{149,151} This method has been used to study intergranular corrosion,¹⁵² the structure of snow,¹⁵³ of deformation,¹⁵⁴ and of fatigue cracking in titanium alloys¹⁵⁵ (see also Fig. 9). The approach tends to be limited to relatively low strains because the diffracted spots gradually broaden with plasticity making it increasingly difficult to infer the grain shapes.

An alternative method is micro-beam Laue diffraction. It uses a narrow (20 × 20 μm say) polychromatic X-ray beam to illuminate a sampling volume within



7 Illustration of the analysis of the shape and size of grains during recrystallisation using the capabilities of the 3DXRD method. The figure shows 3D maps of a growing grain in deformed Al. Three of the 73 recorded pictures are shown. *a* Picture 1, *b* picture 39 and *c* picture 59. In the coordinate system given, x-axis coincides with the normal direction (ND) (spatial resolution is $22\ \mu\text{m}$), the y-axis coincides with the transverse direction (TD) (spatial resolution is $4.3\ \mu\text{m}$) and the z-axis coincides with the Rolling Direction (RD) (spatial resolution of $6\ \mu\text{m}$) (adapted from Ref. 132)

individual grains. The resulting single crystal Laue diffraction patterns consist of a number of Laue spots, which can be indexed to provide the grain orientation and elastic strain.¹⁵⁶ For thin slices, 2D mapping is relatively easy. For 3D scanning, vertical and horizontal

fine wires of tungsten must be traversed just downstream of the sample in order to triangulate the location of the diffraction spots for each beam position making the process somewhat time consuming.

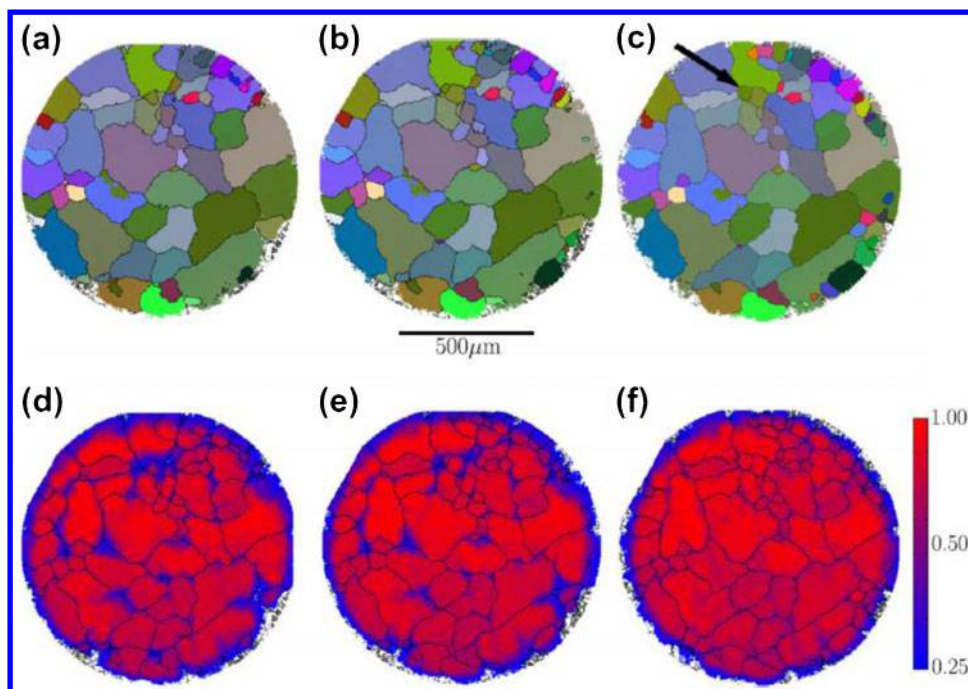
Novel reconstruction strategies

For materials science, most X-ray tomography datasets are collected by acquiring 2D projections as the object is rotated about an axis normal to the incoming beam using either a cone beam (normally lab.) or parallel beam (normally synchrotron) source. In the vast majority of cases these datasets are reconstructed to form an image using filtered back projection (FBP). Analysis suggests that $q\pi/2$ projections are required where q is the number of detector pixels horizontally,¹⁵⁷ such that for a 2048-pixel detector around 3200 projections are recommended. This has developed from the original fan beam technique providing a single tomographic slice. The Feldkamp, Davis and Kress (FDK)¹⁵⁸ algorithm is a widely used cone beam FBP algorithm that can be regarded as a natural extension of the fan beam case. However, a circular cone beam scan is an incomplete data set for reconstructing the volume since Tuy's condition¹⁵⁹ is not satisfied, so that any reconstruction will be approximate except for the mid-plane slice. By contrast, parallel beam, helical and horizontal circle+vertical line scans all satisfy Tuy's condition with medical CT systems employing helical scans. Consequently for cone beam imaging the approximation becomes increasingly inaccurate for large cone angles. As a result, the image quality degrades with blurring in the axial direction.

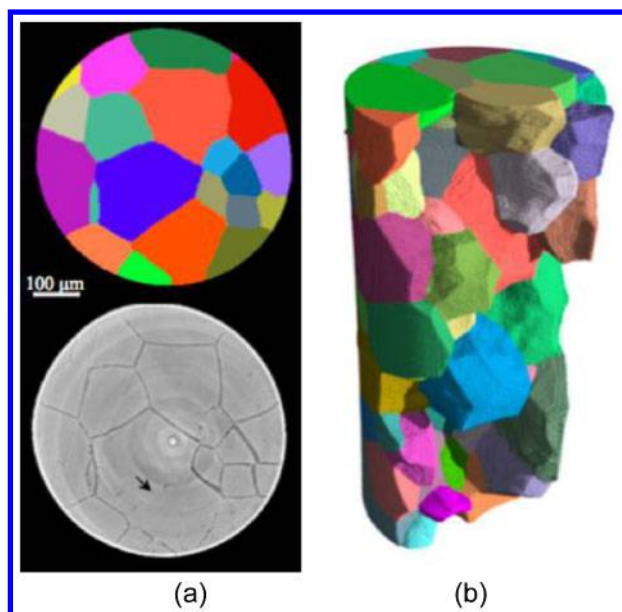
Beam hardening corrections: Artefacts can significantly affect quantification, for example ring artefacts and beam hardening (for polychromatic illumination) can lead to incorrect segmentation using simple thresholding strategies (Figs. 10 and 13). There are a number of experimental methods and procedures to reduce artefacts,¹⁶⁰ however special reconstruction algorithms can significantly reduce ring artefacts¹⁶¹ and account for beam hardening.^{162,163}

Segmentation-oriented reconstruction: In cases where an object comprises a few homogeneous phases, and the primary intention is to distinguish these, it is not sensible to reconstruct the volume image using the full range of greyscales and then to apportion voxels in the image according to arbitrarily chosen threshold ranges. Rather it is more sensible to reconstruct the object with the prior knowledge that only a small number of grey levels are expected. Discrete tomography¹⁶⁴ considers the reconstruction of images from a small number of projections, where the set of pixel values is known to have only a few discrete values. It tends to deliver images that are more easily segmented than traditional FBP algorithms because the recovered image solutions are weighted towards a discrete number of more physically realistic grey scales, see Fig. 11¹⁶⁵ 'Compressed sensing' (see below) works in a similar fashion; it aims to represent many signals using only a few non-zero coefficients in a suitable basis. Clearly an image made up of a few intensity levels is simpler than one comprising the complete range of grey scales.

Under-sampled imaging: There are many cases where 180° rotation is not possible (e.g. due to X-ray attenuation through environmental rig components, or by long path lengths through flat samples), or where too



8 Illustration of the analysis of the shape and size of grains during annealing using the capabilities of the forward reconstruction modelling method. Grain maps for high purity aluminium (maps of the central layer of the measured volume) are shown. *a–c* show orientation maps in the initial, $\sim 50^\circ\text{C}$ and $\sim 70^\circ\text{C}$ anneal states, respectively. Each mesh triangle, or voxel, is coloured by mapping orientation components (Rodrigues vector representation) to the red-green-blue (RGB) colour space. Black lines are drawn between adjacent triangles that have mis-orientations $> 2^\circ$. *d–f* show maps of the confidence metric, corresponding to the orientation maps in *a–c* with the same black lines. The arrow in *c* indicates a nucleated grain¹⁴⁶

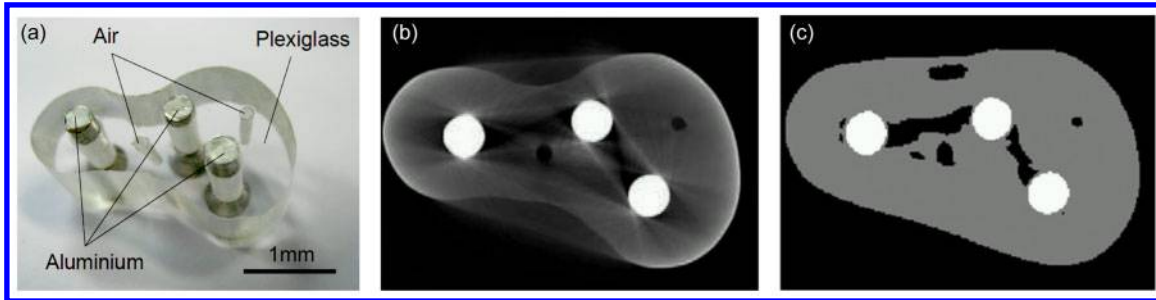


9 *a* Illustration of the capabilities of diffraction contrast tomography (DCT) to non-destructively produce a grain map of a polycrystal. Comparison of grain microstructure reconstruction of the same slice obtained from DCT and phase contrast tomography (PCT) in a beta Ti alloy. Layer-like precipitation of alpha Ti (hcp) reveals part of the grain boundaries in PCT. *b* 3D rendition of grain microstructure as reconstructed from DCT for the same sample¹⁵⁵

few projections are collected because the time to collect the recommended number is prohibitively long, or where the X-ray dose must be limited to safe levels.¹⁶⁷ In such under-sampled cases iterative algorithms can produce substantially better images than FBP methods.¹⁶⁸

For few-phase objects, discrete tomography and compressed sensing algorithms can be very effective at reconstructing images from low numbers of projections. Compressed sensing has shown that an $N \times N$ image can be accurately reconstructed using on the order of $S \ln N$ samples provided that there are only S significant pixels in the image.¹⁶⁶ Tomography images can be rendered more sparse by a number of means, for example by creating a new image in which the value of each pixel has been subtracted from its neighbours in x and y to create a 'gradient pixel'. Chen *et al.*¹⁶⁶ have shown that when reconstructing a dynamic series it is possible to use a variant where the target image is subtracted at each time frame from the prior image (obtained by FBP using many projections) using a so-called prior image constrained compressed sensing method (PICCS) showing very promising results using an under-sampling of 32 (20 projections) as shown in Fig. 11. This method could find application when the number of projections needs to be restricted to capture short timescale events, or to reduce X-ray dose. Similarly the method is appropriate for sparse datasets comprising a few homogeneous phases that require segmentation.

Spatio-temporal reconstruction: Conventionally, a time sequence of tomograms is obtained by reconstructing each image independently. This frame-by-frame approach fails to exploit the inherent correlations along



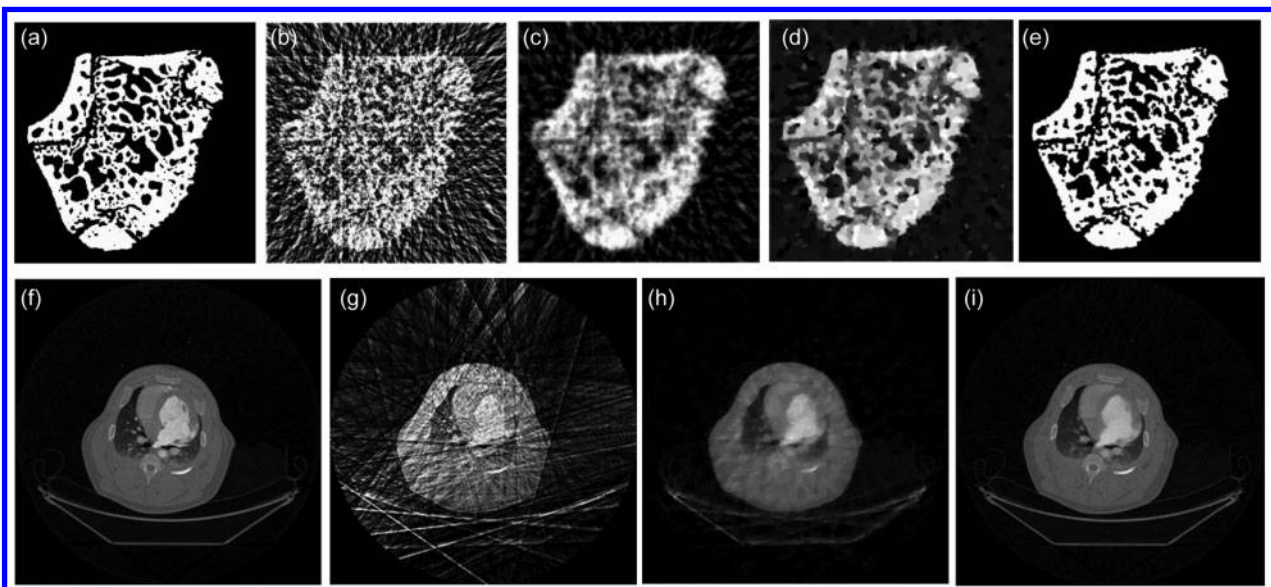
10 **a** 'Barbapapa' phantom comprising air, plexiglass and aluminium regions, **b** filtered back projection (FBP) image reconstructed from 300 projections acquired at 60 kV using a SkyScan 1172 computer tomography (CT) scanner showing significant beam hardening artefacts and **c** simple thresholding incorrectly segments the three phases in the phantom¹⁶³

the time axis associated with measuring a real evolving object. Ideally, one should treat all the data from an imaging sequence as a whole, rather than as a collection of individual time frames. Clearly to reconstruct the whole sequence in one go would be a significant computational challenge, however there are significant benefits when the data is noisy or under-sampled. This challenge has started to be tackled in neutron CT¹⁶⁹ where the flux is characteristically lower such that only a few noisy projections are often collected, but the technique is equally promising, if computationally challenging, for X-ray CT.

Possible future directions: By reducing the signal required to create a satisfactory image, iterative imaging promises to significantly increase the rate at which 3D images can be obtained, benefitting fast imaging ('Improvement in temporal resolution' section), lowering exposure levels and widening the range of subjects that can be followed by time lapse CT. Further, iterative imaging can deal with blurring artefacts caused by motion.¹⁷⁰ One area that has not been explored significantly at present is metric-focussed reconstruction.

For example if the ultimate aim is to quantify the pore morphology, then perhaps the reconstruction should be configured so as to identify iteratively the pore morphology present in the 3D image that is consistent with the projection data, rather than reconstruct the image without regard for the questions being posed and then extract the quantities by subsequent 3D analysis of the reconstructed images. This might also allow the iterative derivation of uncertainties in metrics associated with the image, e.g. cell connectivity in foams or the degree of crack face contact, whereas at present image reconstructions come with no associated error bars or morphological likelihood estimates.

It should also be noted that while iterative reconstruction techniques offer real advantages in a wide range of sub-optimal imaging reconstruction cases, their application is not straightforward and this has limited their uptake at the present time. In particular each iteration involves the forward-projection of the intermediate 3D image for comparison with the acquired projection data and subsequent iteration to minimise the difference between the two. However, commercial CT systems



11 **Top:** **a** Phantom based on a rat bone and a comparison of reconstructions using 20 projections made by **b** filtered back projection (FBP) **c** Simultaneous Algebraic Reconstruction Technique (SART) **d**, Total Variation Minimization (TVMin) and **e** Discrete Algebraic Reconstruction Technique (DART);¹⁶⁵ **Bottom:** **f** FBP reconstruction using 642 projections of the body of a 47 kg swine acquired at 120 kV, **g** FBP with 20 projections, **h** compressed sensing (CS) using gradient image with 20 projections **i** prior image constrained compressed sensing method (PICCS) using 20 projections¹⁶⁶

involve considerable calibration and correction of the detected data, and in some cases, proprietary optics. As Hsieh *et al.*¹⁷¹ point out, model based iterative reconstruction requires an accurate forward model containing the optics, a noise model incorporating the detector sensitivity and calibration and an image model of the subject. Consequently this currently presents a significant barrier to the uptake of iterative methods such that most of the iterative algorithm development to date has been on simulated phantoms.

Chemical tomography

While conventional attenuation contrast tomography exhibits different levels of contrast according to the atomic number related contrast, it is not possible to distinguish chemical compositions with any certainty because many elemental compositions could give the same overall attenuation contrast. There are many cases in materials science where analysing the exact chemical composition in 3D (i.e. achieving chemical tomography) is of outmost importance to understand the mechanisms at play.

Like absorption, X-ray fluorescence is a well-known phenomenon. When irradiated by incident X-rays at a sufficient energy, electrons of inner shells of the constituent atoms can be ejected leading to chain rearrangements during which electrons from outer shells replace the ejected ones, in turn being replaced by other electrons, etc. X-rays of very well-defined energies are emitted during these rearrangements, and are known as the characteristic K_{α} , K_{β} , etc. By scanning a pencil beam across a sample, and recording the number of photons emitted for these very particular values of energy, it is possible to record a sort of projection, the intensity being proportional to the local chemistry along the irradiated line. If such a projection is recorded for different angular positions of the sample, a tomographic reconstruction of the local chemical composition of the sample can be obtained. Such an experiment takes a very long time as the sample has to be scanned in one direction for each individual slice and each orientation. This has however been attempted using synchrotron radiation.^{172,173}

The same sort of experiment using a pencil beam has also been carried out coupled with a 2D detector to record the diffraction pattern. This was used to non-destructively reconstruct the map of the diffraction pattern in the acquired slice. This method is named diffraction tomography,^{174,175} an earlier variant has been described using an energy dispersive detector.¹⁷⁶ It has been applied recently with a reasonable speed (acquisition of a slice in 20 min) for the study of structural change during high temperature modification of catalysts.¹⁷⁷ Alvarez-Murga *et al.*¹⁷⁸ reviewed some recent results on diffraction/scattering computed tomography. They showed that the method yields an enhancement in the detection of the weak signals coming from minor phases. In the same volume of the same journal, Stock *et al.*¹⁷⁹ report on a diffraction tomography study of an Al/SiC composite showing that the transmitted-intensity reconstruction agreed with that of higher resolution, absorption-contrast synchrotron micro-computed tomography. The reconstruction using the diffraction peak of aluminium (spotty rings) showed the presence of large grains, and the SiC reconstructions revealed the anticipated presence of two microstructural

zones in the fibres. Korsunsky *et al.* used a similar approach to map residual strain after quenching a metallic sample.¹⁸⁰ Finally, in Basile *et al.*¹⁷² both fluorescence and diffraction tomography have been carried out on the same sample.

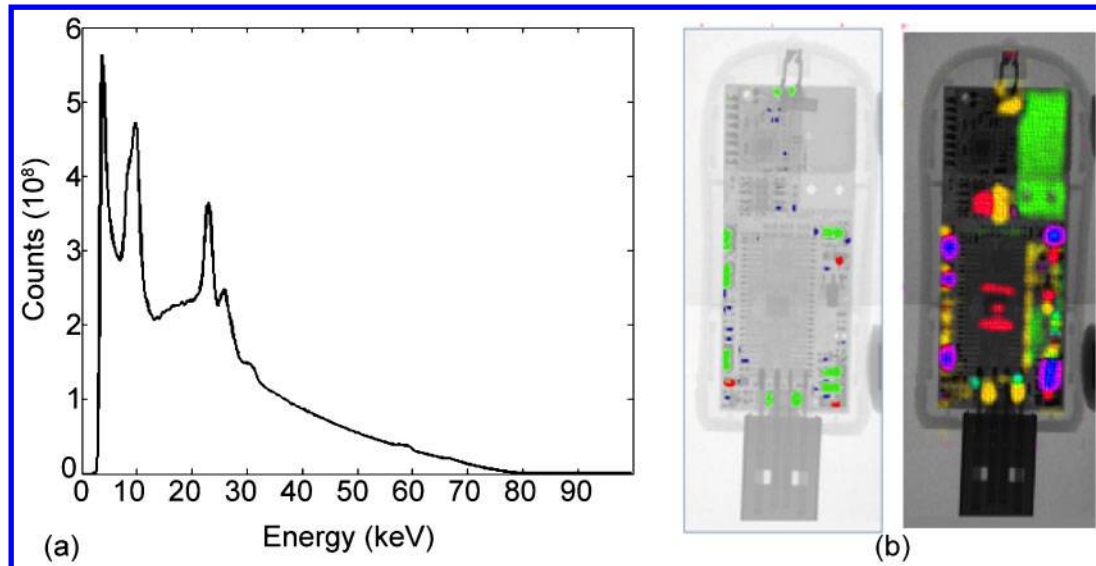
All these methods require extremely long exposure times and are restricted today to long experiments at synchrotron sources. Previously, some level of elemental differentiation has been obtained using lab. sources by comparing multiple images collected using different X-ray energies^{181,182} and using sudden changes in attenuation due to characteristic absorption edges as a function of energy to identify elements. Recent developments in energy sensitive area detectors⁷ open up the possibility for this method to be applied quickly and efficiently in one imaging step using a polychromatic beam such as might arise from a laboratory source. We see a lot of potential in many applications for this new emerging technology. Nothing has been published so far in the field of engineering materials but Fig. 12 shows an example of such an energy sensitive image in the case of a USB memory stick.

Local tomography and laminography

The faithful reconstruction of a 3D image by FBP strictly requires the whole width of the object to remain within the field of view, and sufficiently illuminated, throughout the 180° rotation.¹⁵⁷ If this is not the case, there will be some missing data (some or all rows in the sinograms will be truncated) indicating that the standard FBP method is no longer strictly valid. This is known to give rise to artefacts in the reconstructions, most notably a centre-to-edge 'glow' artefact.¹⁸³

Given that CCD detectors usually have between 1000 and 4000 pixels across their width and the spatial resolution is a few pixels, this requirement to image the whole sample places a limit on the smallest feature observable to around a thousandth of the sample width. In many cases, for example, when imaging impact damage in thin plates, this means that the features of interest are too small to be observed by whole sample tomography. This problem can be countered to some extent by stitching together multiple images acquired side by side to create a large composite image as if a more pixelated detector were available¹⁸⁴ but this can be time consuming.

Local (or RoI) tomography refers to the acquisition of a tomographic scan under conditions where at least part of the sample is not projected onto the detector for at least some projections acquired during the scan. There are experimental approaches as well analytic and iterative reconstruction algorithms that can be implemented in such cases. One experimental approach to overcome this problem, termed here 'zoom-in tomography' is to combine low resolution information of the whole sample with the high resolution data within the RoI to produce a best estimate reconstruction.¹⁸⁵⁻¹⁸⁷ This method has been demonstrated to be successful,¹⁸⁸ but can be difficult to apply in practice, both in terms of collecting the different magnification images and the subsequent accurate registration (both spatially and in terms of voxel values) of the low and high resolution projections.¹⁸⁹ Other analytic and iterative local tomography reconstruction methods are discussed in Ref. 190.



12 New possibilities are offered by energy sensitive area detectors as illustrated in this figure for a USB memory stick. Instead of a single image for one projection, a complete X-ray spectrum such as this shown in *a* is collected at each individual pixel. This allows many radiographs like that shown in *b* with regions showing specific absorption edges (red=tellurium, blue=barium and green=neodymium) to be reconstructed. *b* (right) Reconstructed X-ray fluorescence mapping of the dongle showing: bromine (green), tin (yellow), zirconium (turquoise), barium (blue) and silver (red)⁷

It has been shown that for a wide range of objects, the effect of truncation of the sinogram on feature detection in the RoI is negligible if (i) the truncated rows are extended by using an average value derived from the row that is extended and (ii) the number of projections ($Q\pi/2$) is calculated not on the basis of the number of pixels on the camera, q , but on the number of pixels, Q , that would be required to scan the whole sample at the chosen pixel resolution.¹⁸⁹

There are also situations where the RoI reconstruction is straightforward without any correction because the missing region is isotropic in all directions, for example the X-ray transparent tubes used as a structural part of many *in situ* loading or environmental rigs, e.g. Ref. 191. In some cases, samples larger than the RoI are needed to ensure the images are representative of the bulk (either geometrically as for cellular solids, or in terms of stress state). Even if these materials are not completely isotropic, their effect on the projections may be effectively so. For example when loading cellular materials, uncorrected local tomography gives good reconstruction results, e.g. Ref. 192, because the effect of the foam cells outside the RoI is essentially the same in all projections.

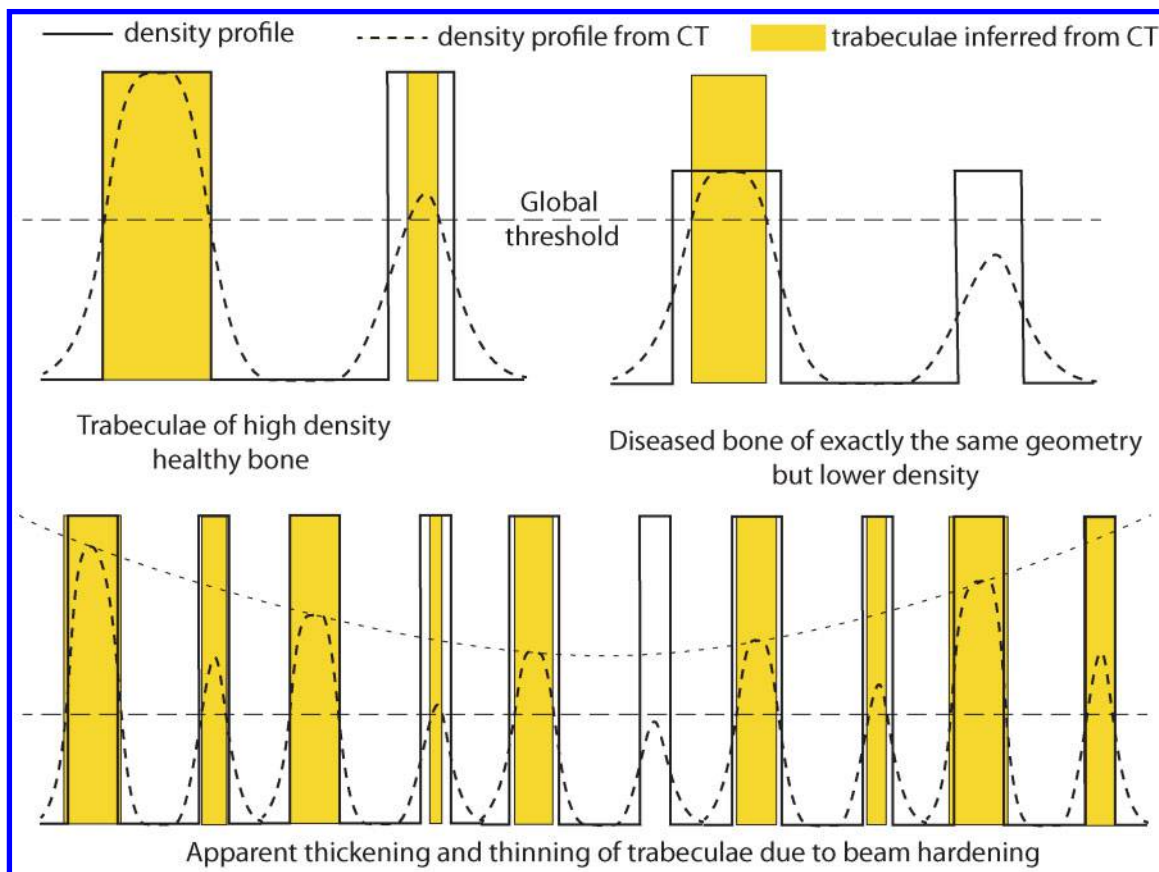
There are many cases in materials research where the sample is extended in two dimensions (electronic devices, metal plates or composite sheets, etc.). For the same reason as those explained just above, high resolution tomography acquisition is not possible for 2D extended geometries. Laminography is an alternative to tomography in this case. Laminography, having been used rather early in medicine,¹⁹³ has been applied more recently in engineering science^{194,195} using laboratory sources^{194,195} and even nanoCT laboratory systems.¹⁹⁶ Traditionally laminography can be thought of as the collection of radiographs with the object being rotated about an axis normal to the plate but inclined to the incident beam, although in purpose built machines, the source and detector precess around the sample. More recently, laminography has also been implemented on synchrotron

sources, allowing high resolution RoI images in the middle of very large sheet-like samples to be acquired focussing on specific regions near the centre of flat samples. This opens doors for the observation of damage processes during *in situ* loading of sheets.¹⁹⁷ Damage evolution ahead of a crack in composite laminates has been successfully observed using this technique in laminography experiments at similar resolutions as typically obtained by tomography.¹⁹⁸

Quantifying 3D images

Extracting quantitative parameters from 3D images requires appropriate image processing, segmentation and analysis. These three procedures have been applied extensively for the analysis of 2D images. Image *processing* is generally applied to 'improve' the image. It mainly involves grey level modification (equalisation, normalisation, brightness and contrast adjustment, etc.) and filtering (to remove noise or to subtract background) in the spatial or frequency domains. *Segmentation* is the procedure by which a continuous grey scale is apportioned to certain discrete groups, usually based solely on their grey levels. The aim is to define which regions of the image belong to the different phases present in the material. The grey level in the reconstruction being proportional to the local attenuation level corresponding to the appropriate phase, segmentation can often be made by simple thresholding but when the contrast between phases is faint, more sophisticated automated methods based on thresholds, clustering techniques or deformable models¹⁹⁹ can also be used. Image processing and segmentation in 3D are directly analogous to the same processes in 2D and so we will not focus on these two aspects in the present review except for some remarks at the end of this section.

Image *analysis* is probably the step where the most significant differences arise between 2D and 3D. It is devoted to the determination of meaningful measures of



13 Diagrams of density profiles across trabeculae of various wall thicknesses and densities aid in understanding the problems that can occur in using uniform thresholds in the case of density variations (top) and beam hardening (bottom). The attenuation contrast profiles recorded by CT are shown dashed and reflect the spatial resolution of the method. The actual borders are given by the solid lines, the yellow regions, the borders inferred by CT using a global threshold (modified from Ref. 200)

the constituent phases and their geometries, for example to quantify their number, fraction, size, distribution and surface topography. The development of many 3D tools has emerged as extensions of existing 2D methods. One easy way to exploit existing 2D approaches is to sequentially apply existing 2D tools to a volume slice by slice. Thresholding for phase fraction measurement, for example, can be done by pseudo 2D analysis, often with little impact on the results. By contrast, when the features in the microstructure have a complex morphology, such as corrosion cracks, coalesced cavities or cellular materials (foams, entangled materials, etc.), it is also important to use algorithms that are fully implemented in 3D.

Both global and local thresholding methods are used to quantify microstructure. In global thresholding, a single global greyscale value is selected to segment regions. 2D histogram methods where segmentation is done, (i) with respect to range of grey scale values or, (ii) with respect to the gradient of grey scale values are readily available in many commercial and non-commercial 3D processing software packages (e.g. Drishti, <http://code.google.com/p/drishti-2/>). In many cases these give good results, although because the phase fractions can often be linearly related to the choice of the threshold value chosen independent calibration of the threshold value may be necessary.

It was recognised early on,²⁰⁰ in the context of bone mineral density measurement, that density variations

and the poor resolving of thin cell walls could lead to spurious wall thickness measurements if global thresholding is used (Fig. 13 (top)). Measurements by global thresholding can be particularly sensitive to beam hardening if unaccounted for; increasing the apparent density towards the perimeter and decreasing it towards the centre causing particular problems for bone density measurement and other quantification procedures (Fig. 13 (bottom)). Rather than using global threshold values it has been found advantageous to select a local cut-off value using the frequency–distribution graph and a half-maximum height (HMH) measure.²⁰¹

Suitable algorithms have been developed both commercially and within the framework of open source packages.²⁰² The sections below discuss a range of archetypal 3D analysis problems performed on static 3D reconstruction of the microstructure. We also consider in this section examples where the authors have studied statistically the evolution of the microstructure from *ex situ* observation of several different samples. The quantification of changes in the microstructure over time during *in situ* experiments is further described in the ‘Quantifying time lapse CT’ and ‘Modelling based on X-ray tomography images’ sections.

Dimensional measurements

While the major focus of this review is on quantifying materials science microstructures, it is important to quantify the dimensional accuracy of parameters

obtained from CT images, whether to ensure components lie within geometrical manufacturing tolerances, or to assess critical materials science metrics (e.g. the distribution of defect sizes across a casting). It should be borne in mind that for cone beam tomography, the Feldkamp, Davis, Kress reconstruction algorithm¹⁵⁸ is an approximation outside of the mid-plane (see 'Novel reconstruction strategies' section). The result is image quality degradation at high cone angles, often giving rise to blurring in the axial direction. As a result, features measured close to the mid-plane may be measured more accurately than those significantly above or below the plane perpendicular to the rotation axis, including the source.

As regards dimensional metrology, an international round robin was held recently drawing the following conclusions:²⁰³

- (i) only a minority of expert users participating in the inter-comparison were able to perform length measurements with errors below the specification of their CT systems. However, the CT audit results indicate that length measurement errors in the order of 1/10th of the voxel size are achievable.
 - in the case of unidirectional length measurements, only 50% of the participants who quoted a maximum permissible error of length measurement $E_{L,MPE}$ were able to perform actual length measurement errors within their $E_{L,MPE}$
 - in the case of bidirectional length measurements, only 33% of the participants who declared an $E_{L,MPE}$ were able to perform actual length measurement errors within their $E_{L,MPE}$.
- (ii) the participants had difficulties in evaluating measurement uncertainty appropriately: almost half quoted uncertainties that were smaller than their measurements would suggest and that traceability of dimensional measurements is still a major challenge in CT scanning, even for expert users.
- (iii) a new testing method has been proposed for quantifying the structural resolution, based on an 'Hourglass' standard sample comprising two spheres in contact and measuring the apparent contact diameter, d : a smaller d value indicates a higher spatial resolution. A tetrahedral stack of equisized balls has been suggested as a standard sample elsewhere.²⁰⁴

Inclusion/matrix morphologies

For bulk materials, the morphological character of second phases, inclusions or cavities are often of critical importance. In such simple cases the matrix fully embeds inclusions or voids, the parameters of which (size, elongation, surface, etc.) should be determined. This has been one of the major outputs of early tomography measurements on particulate composites^{205,206} subsequently refined to quantify the local particle volume fraction^{206,207} since clustering can have a detrimental effect on the fracture properties of composites. In Ref. 208 the authors have measured the size of clusters of reinforcing TiB_2 particles and shown, using static imaging, that the size and number of clusters were reduced as the holding time at high temperature was increased. Toda *et al.*²⁰⁹ have measured the growth of micropores in pure Al and Mg samples during high

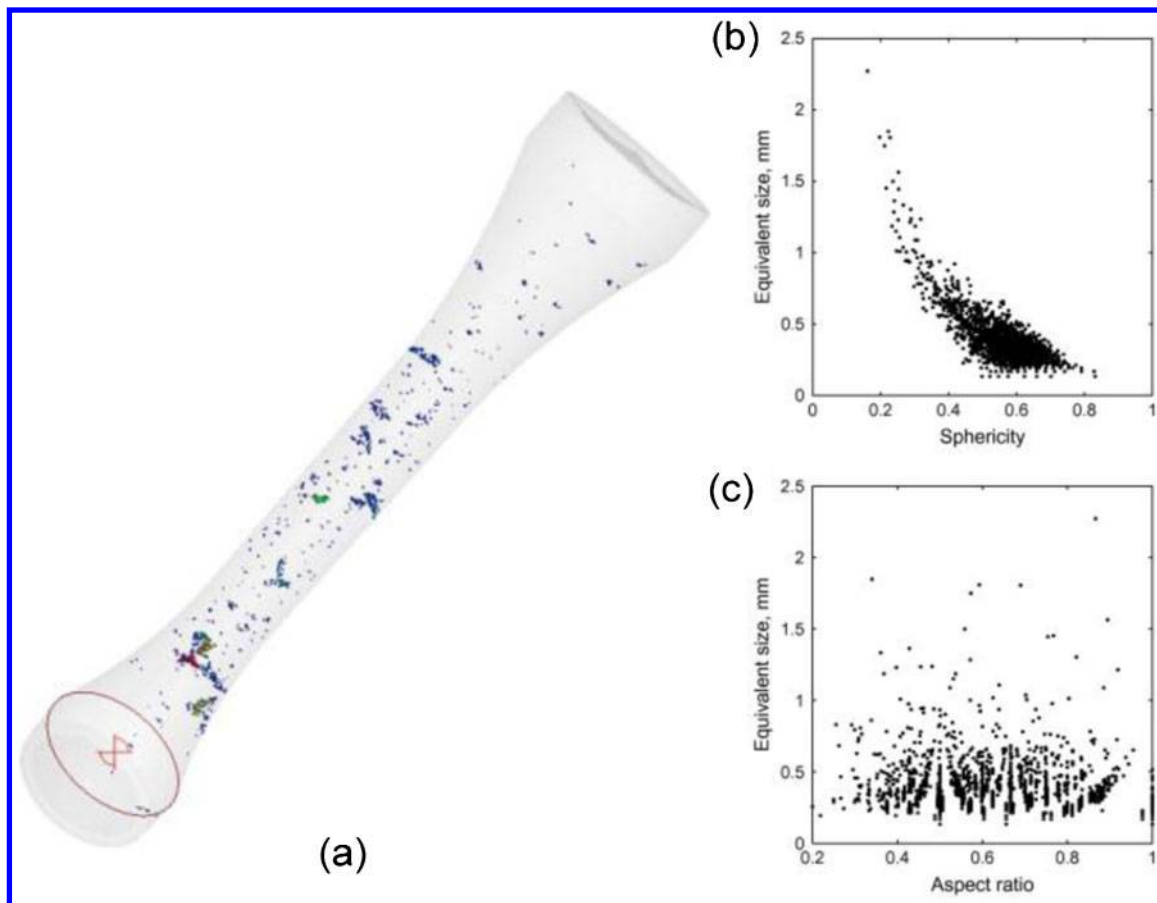
temperature exposure using a relatively high resolution (0.47 and 0.088 μm voxel sizes) clarifying that their growth is dominated by Ostwald ripening. Generally, it is better to quantify such populations from 3D images rather than 2D ones provided that precautions are taken regarding segmentation, resolution, etc., since it obviates the need for transforming a 2D size histogram into a 3D one. However, in all the cases listed above, where the shape of the inclusions is rather simple, 2D analysis coupled with stereology remains a cost-effective and useful tool. In our opinion, a systematic investigation of the bias induced by 2D imaging on the determination of 3D metrics is probably still required for specific morphologies. Conversely, tomography can also lead to quantification errors, for example the effect of insufficient resolution on the quantification of the nucleation stage of ductile damage has been highlighted in Ref. 210. The results at low resolution are strongly biased, due to the failure to detect a high number of small cavities while the largest cavities are faithfully recorded. Examples have also been given in the preceding section showing that bad segmentation or beam hardening effects can bias quantification.

When the shape of inclusions or voids becomes more complex, one can no longer rely on surface (2D) observation. Unreinforced aluminium alloys (AAs), for example contain a lot of so-called 'intermetallic particles'; the size and morphology of these (including sphericity, local curvature radii and connectivity in cases of intermetallic content) has been quantified in Refs. 38 and 211–215. In cast metals (aluminium and magnesium), the complex shape of the initial morphology of the shrinkage pores is the key parameter determining their tensile²¹⁶ and fatigue properties.^{217–220} In all these cases, the size of each cavity, as well as its sphericity, distance to the interface and projected surface perpendicular to the tensile direction, has been used for a better prediction of the fatigue crack initiation probability on each cavity. An example of such a quantification in Ref. 219 is shown in Fig. 14. This is also sometimes coupled with a Finite Element simulation of the stresses around each pore.^{218,221}

Complex attributes such as the local orientation of anisotropic features (rod- or plate-like second phases in a matrix) have also been measured in metallic materials based on the so-called 'grey level texture' in the images. For this, it is necessary to calculate the gradient in the neighbourhood of each voxel. In Ref. 222 this value of the local orientation was needed to understand the structure of 'Widmanstätten' like microstructures in dual phase titanium alloy.

Cellular and highly porous morphologies

X-ray tomography is making a significant contribution in terms of 3D analysis for cellular materials: information that is not easy to capture using standard surface microscopy techniques. The major problem has been the availability of the software tools capable of performing the appropriate measurement on these connected systems. This is now largely solved, thanks to commercial and open source software suites (ImageJ, Avizo, VGStudiomax, Morpho+, Pore3D, Blob3D, Imorph). Some of the earliest studies were of trabecular bone morphology and were reported in 1989,²²³ providing a measure of the three-dimensional connectivity in cancellous bone, local thresholding was used²⁰⁰ to avoid



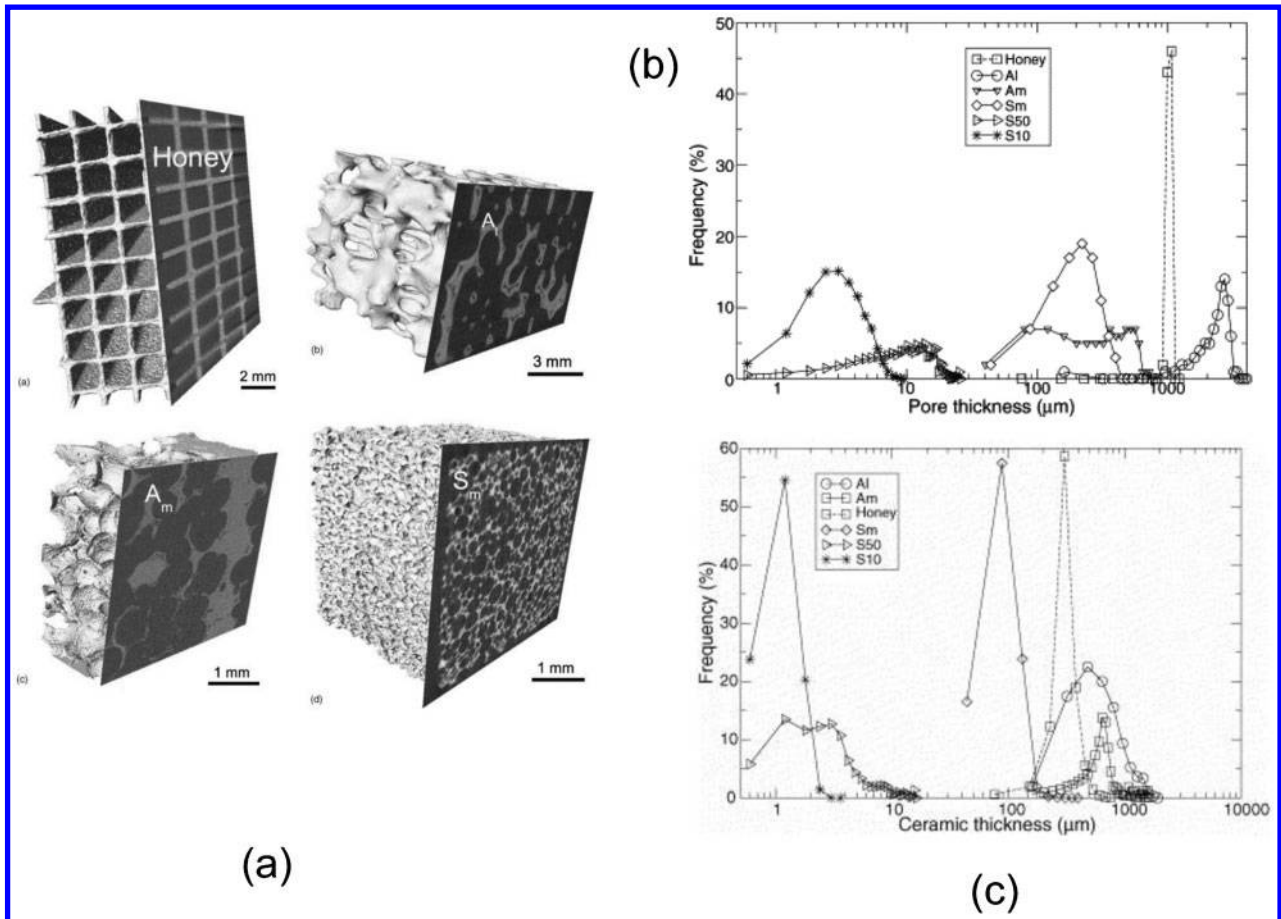
14 Illustration of the capabilities of X-ray tomography to quantify the morphology of pores in a metal. *a* Qualitative 3D view of defects detected by X-ray CT in a fatigue specimen in a cast aluminium alloy.²¹⁹ *b* and *c* Quantification performed using the 3D dataset (size, sphericity and aspect ratio)

spurious thickening or thinning of trabeculae either due to variations in mineral content or due to poor resolution of thin trabeculae. A rather complete investigation of many different morphological parameters (volume fraction spatial distribution, pore size and solid phase thickness, tortuosity, etc.) has been presented in Ref. 224, where a selection of different cellular ceramics exhibiting various morphologies (from honeycombs to stochastic foams) and pore size (from nanometres to millimetres) was imaged and subsequently quantified. In the case of closed cell foams, the same types of procedures as those used for inclusions in matrices described in 'Inclusion/matrix morphologies' section can be applied but in the case of interconnected pore networks, this analysis cannot be made as easily because in this case the notion of an inclusion vanishes and the sample often effectively contains a single large interconnected pore. For measuring the typical size of the pore in interconnected networks, specific 3D Image Analysis procedures based on sequential erosion/dilation operations applied to the binary images with structural elements of increasing size (this procedure is also named 3D granulometry) have been implemented. In Ref. 224 the implementation is performed in ImageJ,²⁰² an open source platform using the java language. Figure 15 shows (a) the materials investigated and (b) the cell size and wall thickness measured by such 3D granulometry operations. Other important parameters can be measured from these images like the specific surface and the tortuosity of the porous network

(the ratio of the length of the path between two points in the porous phase over their distance in straight line).

The paper by Brabant *et al.*²²⁵ is a similar, more recent example where many porous samples were analysed and compared. The examples were also chosen to exhibit very different structures and scales: Euville limestone, pine wood, and two different grades of aluminium foam (20 and 10 pores per inch (PPI)). Rather than preserving the connectivity of the porous network and using granulometry, the pores were systematically separated in this latter paper using a watershed algorithm so that the fully connected network of pores was divided into subdomains. Different parameters could then be quantified: porosity, equivalent diameter and maximum opening distributions, orientation of the pores etc. This separation procedure also facilitates a simplified representation of the skeleton of the pore or of the solid phase. This is useful input for the modelling of transport properties and is available as an output from analysis software (imporh, avizo, Morpho+). After separation of the network into different pores, the pore throats can also be analysed (i.e. measured and used for the modelling of transport properties such as permeability). This has been achieved in Refs. 226–229 and is shown in Fig. 16.

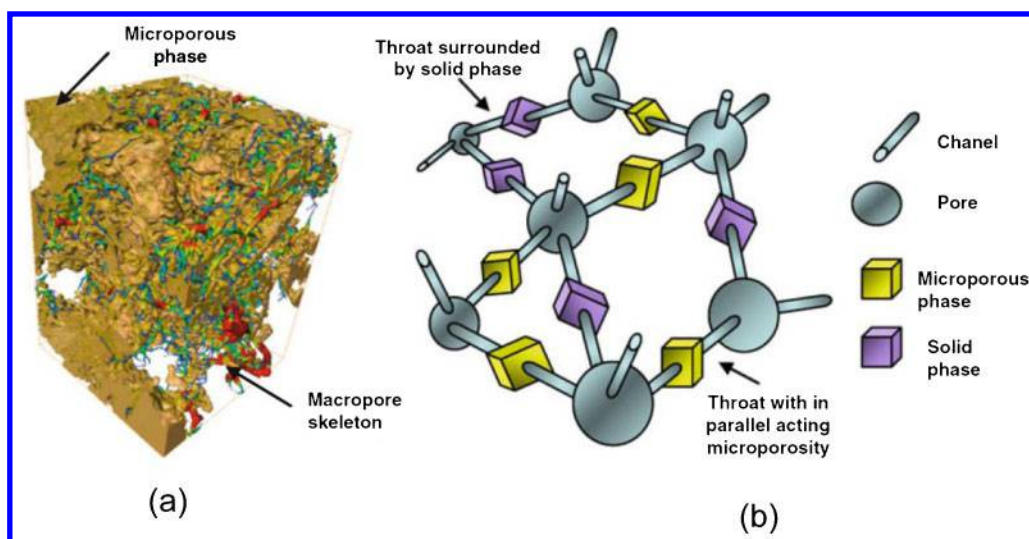
Others have focussed on the pore size distribution.^{230–233} In Ref. 234 this distribution was measured over several length scales using a suite of 3D imaging methods (X-ray CT, focussed ion beam serial sectioning, electron tomography) and is compared with Mercury intrusion measurements. Wall thickness measurement can also be achieved



15 Quantification of the morphology of connected pores or solid phase in highly porous materials. The difficulty is that the phases are fully connected and special image processing methods like mathematical morphology granulometry have to be employed. *a* Qualitative 3D view of several cellular ceramics analysed in Ref. 224 and *b* the corresponding cell size and *c* wall thickness distribution

using 3D images. Foam strut thickness has been measured in Refs. 100 and 235. In Ref. 236 porous Ti alloys were analysed morphologically using interface shape and interface normal distributions and in Ref. 232 circularity was also measured.

It should always be borne in mind that most of these measurements are performed using approximations calculated using discretised (voxelised) images. This discretised nature can have a strong influence on the results, especially in terms of surface length and surface



16 The description of a complex pore network can be simplified by the creation of a geometrical graph composed of nodes and tunnels. The specific dimensions of these simple elements have to be measured from the images. The figure shows as an example the transcription of *a* porous network into *b* a network graph in a carbonate reservoir rock^{226,228}

area, these parameters being overestimated for smooth objects (e.g. spheres).

Finally, it should also be remembered that some quantities are fractal such that their measured extent increases as the resolution of measurement increases; this is the classical ‘length of the coastline’ paradox.²³⁷ An illustration of this effect is the finding that the measured surface area of porosity within a solid oxide fuel cell increased as the spatial resolution of the tomographic scan was increased.²³⁸

Fibrous structures and other morphologies

Fibrous materials encompass polymer, ceramic or metals reinforced with elongated fibres, and also porous entanglement of fibres (like rock, glass or steel wools). In these materials, the size distribution is only rarely of interest²³⁹ because the fibres often have a fixed diameter. The focus is more often the distribution of fibre orientations.^{239,240} The structure can be rather complex in fibrous materials and was analysed in detail in Ref. 241 where 3D image analysis was carried out to skeletonise (simplified representation of the centrelines of the fibres) and construct a graph (determination of the coordinates of the nodes in the skeleton). Once such a graph is constructed it becomes rather easy to calculate parameters such as tortuosity and the distance between fibres. In Ref. 242 composites were studied but the fibres size and orientation were of no interest and the authors have rather focussed on porosity and its connectivity. Paper is a good example of entangled fibrous material where the knowledge of the microstructure helps to explain the macroscopic properties. Paper has been widely studied using X-ray tomography. For this type of material, (non-woven fibre mats) the interest is often on the distances between fibre to fibre contacts. This is a non-trivial measurement, fibre to fibre contact can be difficult to quantify.

In Refs. 243 and 244, auto-correlation functions were measured. This was used to analyse the isotropy in different directions for composite preforms and paper respectively. The auto-correlation functions are calculated from the correlation of a 2D image with a shifted version of itself of a given distance, d . This is generally done on binary images to analyse the spatial distribution of the white phase embedded in the black one. These functions are widely used in 2D image processing and their definition in 3D is directly analogous, by just changing the direction in which the sample is shifted. For instance, for a woven textile of carbon fibres, Badel²⁴³ found that the correlation function of the fibres in the yarns measured in the plane transverse to the yarn remained very isotropic despite the progressive anisotropic deformation of the preform. This conclusion allowed the authors to significantly simplify the textile modelling strategy.

Density measurements

Davis *et al.*¹⁶⁰ point out ‘When Elliott and Dover first described X-ray microtomography in 1982,²⁴⁵ they had one aim in mind: To devise a means of quantifying and mapping mineral concentration in biological hard tissue’. Further, they remind us that in many ways, today’s full-field scanners are not well suited for the quantification of the linear attenuation coefficient, which requires a well-defined source, the collection only of photons that travel in straight lines and a simple

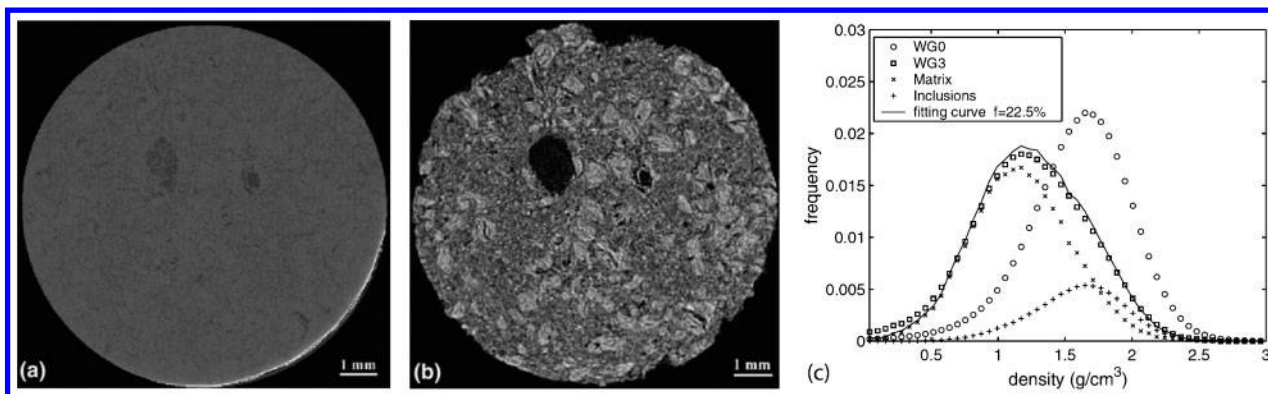
application of Beer’s law for attenuation. In trading discrimination for speed, today’s scanners collect scattered photons, often employ white radiation such that Beer’s Law is not obeyed (giving beam hardening) while CCD systems are prone to uneven pixel responses (ring artefacts) and charge bleeding. Indeed errors of up to 30% can be incurred due to beam hardening in estimating bone densities for 10 mm samples at 80 kV.²⁴⁶ Consequently, it is very important for quantitative densitometry to make sure that the grey level fluctuation observed is only due to the change in density rather than compositional changes or imaging artefacts. Some artefacts, such as beam hardening can be corrected for (see Quantifying 3D images section), or avoided altogether by using a monochromatic beam, such as found on many synchrotron tomography beam lines. Uneven pixel responses can be normalised for, or removed by translating the detector during acquisition (so-called time delay integration²⁴⁷).

The earliest quantitative voxel value measurements were aimed at measuring bone density^{245,248} and carious teeth enamel²⁴⁹ with demineralisation measured to better than 0.2 g cm^{-3} . In materials science the technique has been used to measure the density variations across pressed and sintered powder metallurgy products,²⁵⁰ the degradation of carbon–carbon composites²⁵¹ oxidised to different degrees over time, the reaction kinetics and morphological evolution mineral phases in cements.²⁵² In providing spatially and time resolved densitometric measurements the method provides much more information than simple conventional volume averaged densitometry measurements. By way of example, consider the loss of carbon during thermal degradation of nuclear graphite.^{209,210} This graphite is extruded and medium textured, containing a mixture of coal–tar pitch binder and filler phase. The filler phase is composed of large needle coke particles (or grains), with an equivalent diameter in the range of 1 mm, and small crushed calcined particles, usually called ‘flour’, whose diameters are smaller than $300 \mu\text{m}$. This kind of graphite was developed for use as the moderator in UK Magnox reactors. As illustrated in Fig. 17, tomography shows that the carbon oxidises preferentially, and not uniformly, in the binder regions made of pitch and small coke grains, rather than the filler carbon particles.^{243,244,253,254} As the matrix phase loses weight disproportionately, this could have significant implications were structural integrity assessments based on average density change. Analytical models of the behaviour of the degraded graphite have been established based on the microstructural tomography data.²⁵⁵

Caveats and cautions

It should be emphasised that 3D imaging should be the first choice option over 2D imaging only in special cases, since:

- there are fewer instruments available,
- the spatial resolution cannot compete with the highest resolution electron microscopes (see Fig. 6),
- unlike the SEM it is not possible to examine regions of large objects at high resolution,
- micro-CT necessarily leads to much larger datasets than for 2D imaging using optical or electron microscopes; this can leave all but the expert overwhelmed and struggling to reduce the volume of 3D data down to simple metrics,



17 Comparison of virtual slices of a Pile Grade A nuclear graphite sample *a* before (WG0) and *b* after 30% weight loss (WG3) by thermal oxidation and *c* the histograms of the matrix and inclusions in their proportions corresponding to the best fit (77.5% matrix, 22.5% inclusions)²⁵³ showing weight loss to be much more significant in the matrix phase

- except in special cases it provides no elemental identification,
- few scanners can combine diffraction and imaging information, as is commonplace in electron microscopes, so provides little crystallographic information,
- it is difficult to use anything other than FBP reconstruction codes on commercial scanners because of the lack of software available to the novice and the fact that proprietary information is needed to create the necessary forward model of the instrument,
- the subsequent analysis typically takes at least an order of magnitude longer than it takes to acquire 3D data; consequently experiments should be embarked upon fully aware of the investment needed to analyse the results. Further results can be difficult to visualise and to interrogate,
- while some basic analysis tools are available, either free or as part of commercial packages, analysis routines must generally be written by the user and so two users may obtain quite different results.

A continual problem with increased spatial resolution from an engineering point of view is the limitation this usually places on the size of the sample to be investigated (see ‘Very high resolution imaging’ and ‘Local tomography and laminography’ sections). Given that samples size is usually $1000 \times$ the spatial resolution or so, this can compromise the scientific or engineering merit of the observation; either from the perspective of a statistically representative volume point of view, or from a mechanically representative point of view. A good example of the former is the need for high resolution of geological cores, (which can be as long as 200 m), which for very fine microstructures such as those associated with shales, necessitates the imaging of millimetre sized volumes. A good example of the latter is the imaging of fatigue cracks in Ti/140 μm diameter SiC fibre composite. In this case micron resolution is required to quantify the crack opening displacement, but samples must contain a significant number of fibres for the crack growth to be representative of growth through the bulk from an engineering viewpoint. In this case image stitching strategies¹⁸⁴ were employed to allow a sample, 4 mm in size, to be viewed using a 1.4 μm pixel size.²⁵⁶

Often, 3D imaging is best considered as part of a multi-scale imaging strategy. For example, micro-CT has been powerfully complemented by FIB serial sectioning and electron tomography to characterise the pore

structure in catalysts across four orders of magnitude²⁵⁷ as well as clays.²⁵⁸ Similarly taken together, X-ray and serial sectioning electron tomography can provide both time dependent information and high resolution microstructural information. This has been termed ‘correlative tomography’ in Ref. 112 where non-destructive X-ray and destructive electron tomography were undertaken sequentially, both within a SEM. The non-destructive nature of X-ray tomography allowed the progress of corrosion of an AA 2024 to be followed over time at 100–200 nm resolution, but detailed examination of the localised corrosion (both chemical and crystallographic) was better performed by destructive serial sectioning and scanning electron microscopy (20 nm resolution).

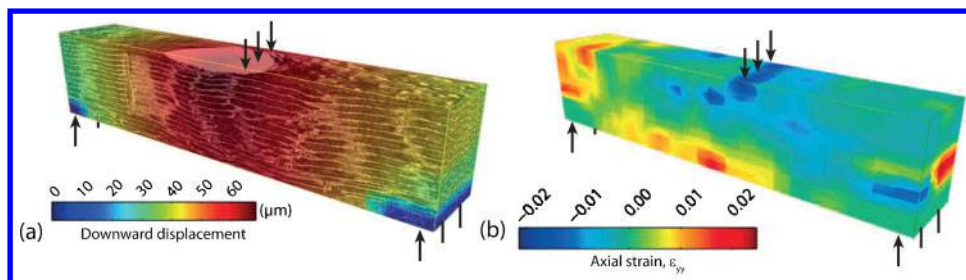
In conclusion, X-ray CT should be restricted to situations where:

- 3D imaging brings superior information (e.g. the connectivity of 3D pore networks),
- where the sample is very delicate (e.g. powder aggregates) and not amenable to 2D sectioning,
- where the sample must be retained for archiving (e.g. museum artefacts),
- where it must be observed *in situ* under conditions that make standard microscopy difficult (e.g. the microstructure of semi-solid metals) and finally,
- where one needs to follow structural evolution in the bulk over time (e.g. damage accumulation under harsh environments).

In this regard as a non-destructive high spatial resolution method, X-ray imaging is particularly well suited to the quantification of structural evolution over time, as discussed in the following section.

Quantifying time lapse CT

In materials science and experimental mechanics, the evolution of structure can be very important during fabrication, throughout service life and as failure approaches. While observing the surface can be useful, in many cases structural changes occur hidden from view. Repeated (time lapse) 3D X-ray imaging allows one to follow the evolution of structure non-destructively in 3D giving rise to so-called 3D movies or 4D imaging.²⁵⁹ While a pictorial understanding is often sufficient, in many cases a more quantitative view is required. Increasingly, this may be to evaluate the predictive capability of analytical or numerical models to describe behaviour.



18 **a** The vertical-displacement field (in microns) determined by digital volume correlation (DVC) for a central region of interest (RoI, $0.44 \times 2.69 \times 0.56$ mm) of a Scots pine sample ($1.57 \times 3.42 \times 0.75$ mm, tangential \times longitudinal \times radial) loaded in three point bending with the exterior loading points 2.51 mm apart on the underside (arrows). The 3D microstructure of the wood is overlaid. **b** The corresponding 3D axial strain field²⁶⁸

It is often useful to quantify the structural changes that take place by static analysis of each 3D image in turn. However, it is also possible to quantify in 3D the distortions of the body through the 3D image sequence. By extension the spatial variation in displacement gives the local strain alongside any local rotations. There are a number of ways of extracting the displacement and hence strain field by comparing successive images. For 2D image sequences, particle tracking (PT) and digital image correlation (DIC) have become standard quantification tools. From surface images, it is only possible to retrieve the surface displacement/strain field. Recently these methods have been extended so that 3D movies of processes recorded *in situ*, can be used as inputs to deliver 3D strain or displacement fields. The capabilities of these methods are reviewed before going on to examine their use for the fracture mechanics assessment of crack propagation and the accumulation of other types of damage from time lapse image sequences.

Digital volume correlation (DVC)

Surface DIC is now well established, both for flat (2D) surfaces using one camera and curved (3D) surfaces using two, providing displacement vectors mapping an array of points from one image to the next. From these displacement vectors strain maps can then be inferred. Over time the technique has been successively improved in terms of displacement measurement accuracy (better than 0.05 of the pixel size) and calculation time.^{260,261}

Although DIC is now used extensively in the analysis of 2D optical microscope and SEM images (see Ref. 262 for a review of the topic), its extension to 3D tomograms (as reviewed by Bay²⁶³) has only recently been gaining momentum despite the fact that the first example of 3D image correlation looking at bone was published many years ago.²⁶⁴ This is probably because the availability of DVC software has been a problem and the first studies were made by direct collaboration between the developers of DVC codes and experimentalists. Recently commercial codes such as that produced by Lavisoin (www.lavisoin.de) have become available so this will surely accelerate the dissemination of the technique. Further, new correlation procedures such as that based on a global consideration of the entire sample rather than on sub-regions,^{265,266} are being reported.

Just as for DIC, it has been shown²⁶⁷ by quantifying the spatial resolution of DVC that the displacement uncertainty is related to the patch size by a -3/2 power law relation. The patch size itself has to be chosen as a compromise between the desire for high spatial resolution of displacement changes and the precision of the

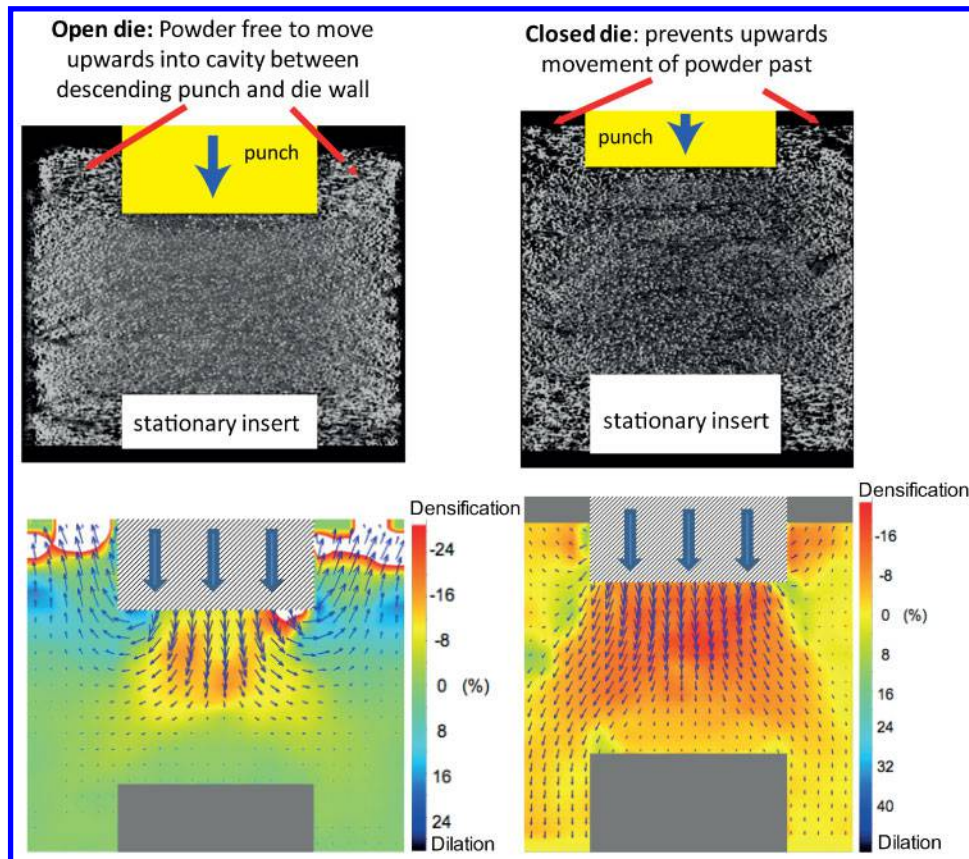
strain vectors. Provided the characteristic wavelength of the grey scale variation in the image is not too long, a typical lateral patch size of 8 or 16 pixels is generally a good compromise. One of the strengths of these methods is that the 3D displacement or strain field can be superimposed on top of the microstructure in order to relate heterogeneities in strain to the underlying microstructure as illustrated in Fig. 18.

Germaneau *et al.*²⁶⁹ have compared strain measurement using X-ray CT and optical scanning tomography (OST) in transparent samples. They concluded that the displacement measurement uncertainty is around 0.037 voxels for OST and 0.049 voxels for X-ray CT. As the algorithms are complex, the computation time for full-field strain calculation can be rather large. This problem is addressed in Ref. 270 where strategies are applied to reduce this computation time. In this respect, graphical process unit (GPU) programming is likely to play a significant role in the future.

Digital volume correlation analysis has been undertaken on both laboratory or synchrotron tomography images of polymer foams,^{192,265,271} the deformation of rock wool,²⁷² of wood,²⁶⁸ of granular materials²⁷³ and of geomaterials.^{274,275} Besides materials deformation, the approach is able to monitor flow, for example the flow of powders during powder metallurgy processes. An example is given in Fig. 19 showing the movement of an Al powder during die compaction. Tracking the flow was aided by the inclusion of 20% of attenuating Sn marker particles. The higher levels of compaction achieved for a closed die as well as low compaction in the shear regions emanating from the corners of the moving punch are evident.

Digital volume correlation is most appropriate for cases where the contrast varies continuously in space and grey levels, whereas feature-based tracking can be more appropriate in cases where the contrast is more discontinuous, for example isolated particles or precipitates in a homogeneous metal matrix. This is because in the latter case, the markers are too isolated to serve as 'contrast support' for a correlation measurement. To improve volume correlation, Bornert *et al.*²⁷⁷ included a high proportion of fine Cu precipitates as markers when studying the deformation of AAs by DVC. A minimum volume fraction of 4% of these particles was necessary for precise DVC measurement.

Digital volume correlation is particularly well suited to dynamic studies as against pseudo-static tracking. It has been used to study the deformation of rocks^{278,279} and the solidification of AAs.^{56,280} The use of DVC in



19 The displacements of an Al powder (grey) containing 20 vol.-% of Sn particles (white) during compaction by the downward movement (by 4 mm) of 10 mm dia. punch (left) for an open 20 mm dia. cylindrical die and (right) for a closed die.²⁷⁶ The arrows indicate the displacements as the punch is moved downwards, while the colours represent the volumetric strains (densification negative)

quantifying deformation around cracks is covered specifically in 'Quantifying damage accumulation and crack growth' section.

3D Particle Tracking (PT)

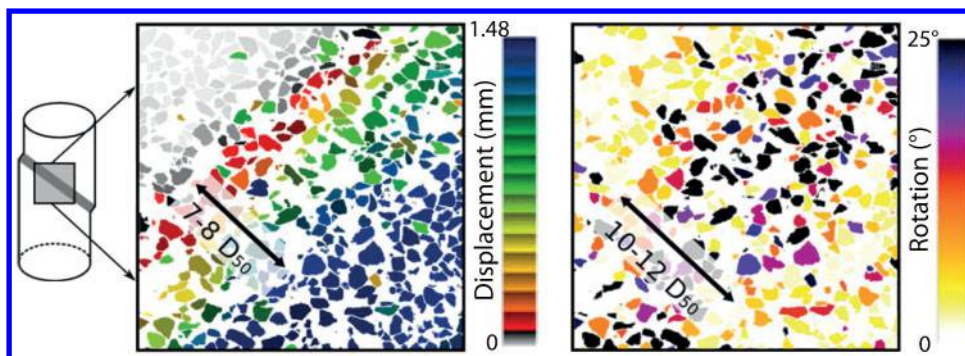
While image correlation focuses on correlating the grey level contrast across a patch with that in successive images, PT is more appropriate when images comprise discrete features against a homogeneous background, such as particles moving in a fluid or precipitates within a metallic alloy. For dynamic studies, PT can be carried out simply using just two projections (X-ray stereography),²⁸¹ but full CT provides much more spatially accurate information.

Tracking the centre of mass of particles or pores in a reconstructed tomographic scan at different states during the deformation of a material is a straightforward way of mapping the displacement and hence local strain field. The extension of standard PT techniques to 3D tomographic image sequences was implemented over 10 years ago. Initially standard video PT methods were extended to 3D.²⁸² Subsequently, a number of purpose designed algorithms have been proposed either focussed on observable features intrinsically present in the microstructure,²⁸³ or added X-ray absorbing marker particles²⁸⁴ (made of tungsten in their case). In both methods, the morphological characteristics of each microstructural feature, e.g. surface area, volume and centre of gravity, are measured precisely using techniques similar to these described in 'Inclusion/matrix morphologies' section. Strain is calculated from the

physical displacement of each microstructural feature that is observed and recognised between two consecutive loading steps.

As for strain measurement, when a sufficient number of markers are dispersed in the 3D volume, the Delaunay tessellation algorithm,²⁸⁵ which generates an aggregate of space-filling irregular tetrahedrons, is used to obtain the local strain distribution. The vertices of each simplex objectively define the four nearest neighbour marker microstructural features. Local strain is calculated in each tetrahedron, assuming a linear displacement field inside the tetrahedrons.

Numerous efforts have been made to improve the accuracy to a better level. A high resolution 3D surface construction algorithm, such as the marching cube algorithm, which gives a pentagonal faceted iso-intensity surface, is often used to improve accuracy to a sub-voxel level. The concept of cluster matching has also been applied by Kobayashi *et al.*²⁸⁶ and shown to perform well in the presence of microstructural agglomeration. Nakazawa *et al.*²⁸⁷ proposed a two-step tracking method that does not require the image registration step. Ando *et al.*²⁸⁸ have recently published a version of the method applied to agglomerates of sand grains. They use the shape of each grain to map their kinematics, and detect local rotation and displacements (see Fig. 20). In this manner they found that the displacements progressively concentrate into localised bands (here 7–8 grains wide). The rotations were largely disorganised until the peak stress after which the



20 In contrast to digital volume correlation (DVC), discrete particle tracking (PT) does not treat the material as a continuum and so can identify individual particle rotations for example. Here approx. 1–2 mm grains of Hostun HN31 sand are subjected to a triaxial compression tests on dry material, performed at 100 kPa confining pressure²⁸⁸

rotations appear to be concentrated in a band somewhat wider than for the displacements. The width of the bands were found to vary with grain morphology, possibly as a result of grain interlocking for the more angularly shaped grains extending the rotations over a wider band. The use of PT for monitoring cracks is discussed in the next section.

Quantifying damage accumulation and crack growth

As a non-destructive technique, X-ray CT can provide a very detailed picture of the evolution of damage through the life of a component. Furthermore the opportunity to host environmental stages means that damage can be followed *in situ* under a range of demanding conditions representative of those experienced in service. Consequently CT enables the quantification of a very wide range of failure mechanisms from transverse ply cracking in composites, to radiation induced cavitation in nuclear components at the tens of nanometre scale. Research focussed initially on ‘static’ measurements of crack length,²⁸⁹ but advantage is increasingly being taken of the DVC or 3D PT techniques described above to quantify crack opening displacements.

In the move to develop materials that are both tough and strong, a range of crack-tip shielding mechanisms can be engineered into new materials, from crack bridging to self-healing. Such mechanisms mean that the crack-tip driving force experienced locally can no longer be related simply to the global parameters normally used to assess the propensity for crack growth (load, crack length and nominal crack-tip stress intensity factor). X-ray CT provides one way to both observe the activation of crack-tip shielding mechanisms and to quantify their efficacy.

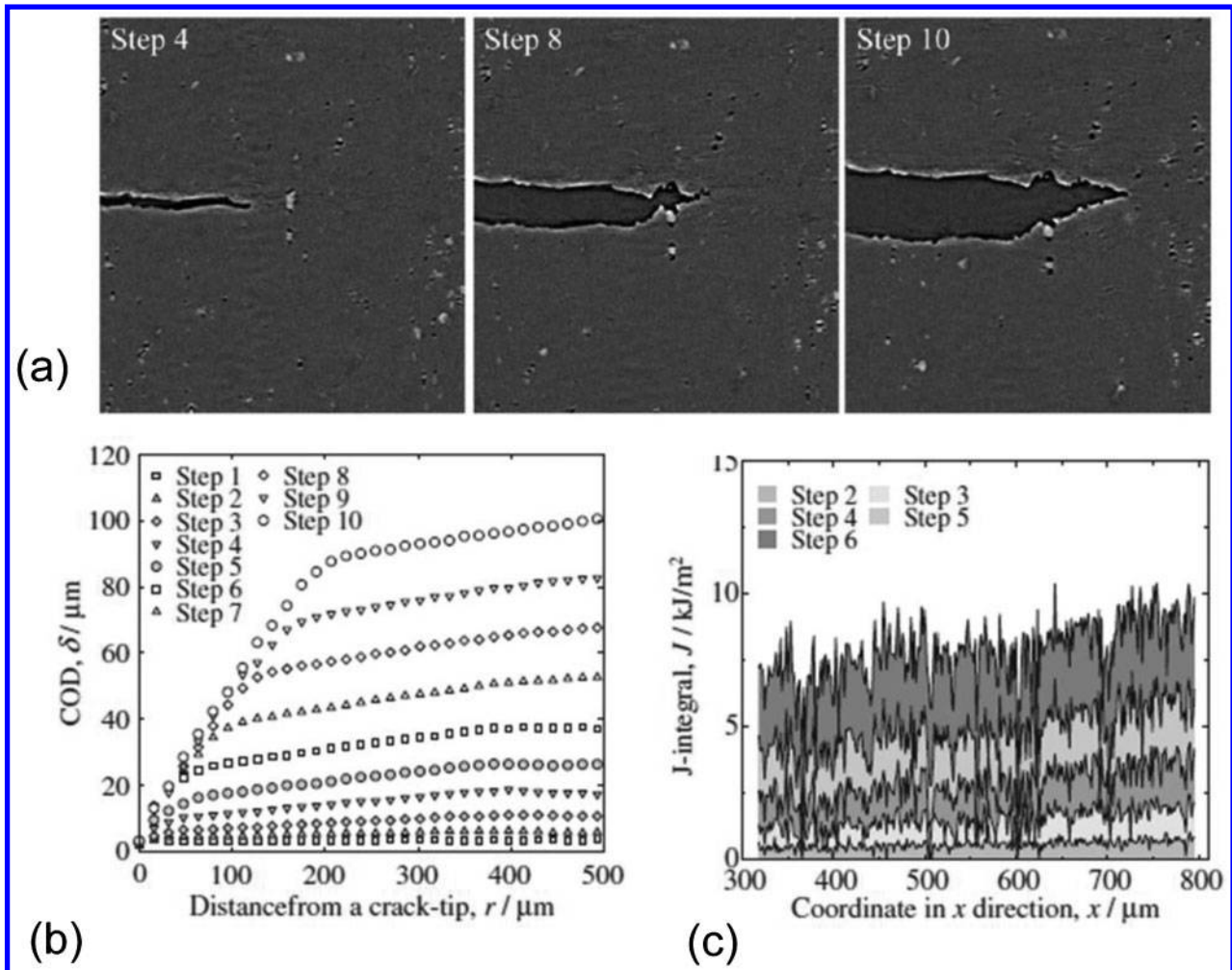
Regarding the level of damage that can be detected, provided they cover a number of pixels, round pores are relatively easy to observe. Determining the presence of cracks tends to be more troublesome. This is because a closed crack is not visible to tomography. Often this need not be a problem if there is an opportunity to study the sample under load so that any cracks are held open. If analysed using DVC or PT, the displacement field around such a loaded crack can also reveal its presence even if the crack is invisible in the image. Further, the fact that a crack is a planar defect means that, in contrast to point defects, they can often be detected even when they are narrower than the pixel size. As discussed by Stock,¹ the narrowest crack opening that can be

measured by tomography is a function of the pixel size and the contrast difference. Breunig *et al.*²⁹⁰ suggest that for aluminium a crack as small as 10% of the pixel size can be measured using a 40 keV lab, system with an Ag target. For a 2000 pixel wide sample this would represent a change in contrast as small as 5×10^{-5} in a given projection. For polymer composites illuminated with X-rays from a 100 kV tungsten source, a sensitivity to cracks 20% of the pixel size has been quoted²⁹¹ improving to 5% if dye penetrant is used to enhance the contrast. However, these values appear rather optimistic under all but the most favourable conditions. In recent years considerable attention has been focussed on using propagation phase contrast²⁹² to enhance the detectability of cracks.^{293,294} While this does aid crack detection, because of the Fresnel edge contrast, it can be more difficult to quantify the opening of the crack.²⁹⁵ Wright *et al.*¹⁰³ report a crack sensitivity of 14% of a pixel for polymer composites with phase contrast.

Quantitative 3D fracture mechanics

In traditional fracture mechanics approaches there are a number of metrics used to determine the propensity for crack growth including; the elastic energy release rate, G , the stress intensity factor, K , the J integral, the crack-tip opening displacement (CTOD) and the crack-tip opening angle (CTOA) as well as the identification of key mechanisms such as closure that can modify that conditions local to the crack-tip and thereby slow or accelerate crack growth relative to that which would be expected solely in terms of the global parameters. X-ray microtomography can provide a quantitative measure of many of these.²⁹⁶

Crack face closure: High resolution X-ray imaging can be used to determine when the faces of a crack close during fatigue crack cycling. So-called crack closure is an important mechanism in retarding fatigue crack growth.²⁹⁷ It has been studied by CT as long ago as 1995²⁹⁸ revealing how the topology of the fracture surface of Al–Li alloy determines the onset and extent of closure during unloading from the maximum load. In this case asperities hasten crack face contact during unloading prior to the ‘knee’ in the crack compliance curve. This ‘knee’ appeared to coincide with load bearing across a significant fraction of the crack faces.^{298,299} Subsequent work²⁸³ substantiates this showing that in many cases loss of crack face contact occurs gradually up to the maximum load rather than at a single definable opening level. For AA, Khor *et al.*²⁹⁴



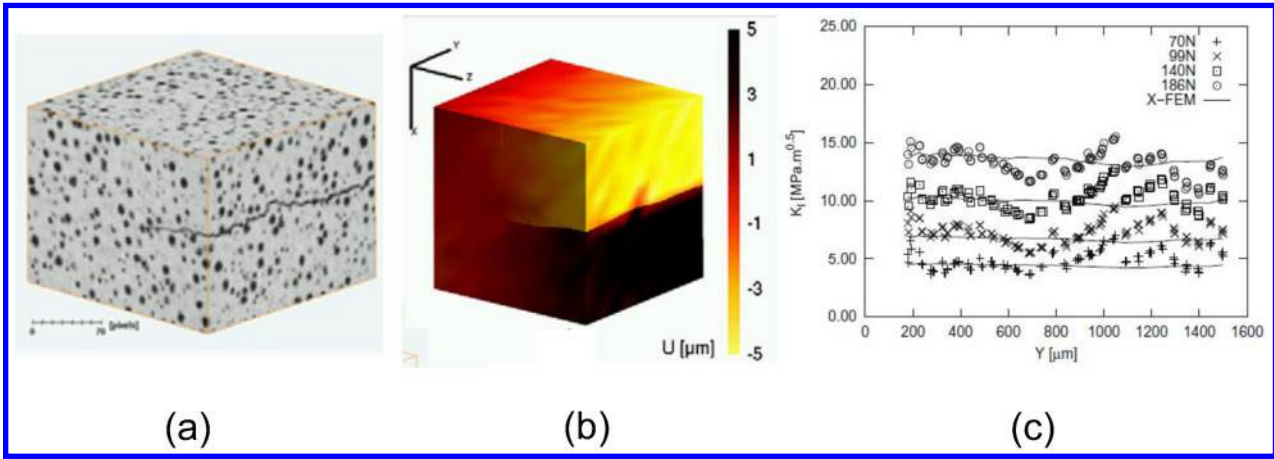
21 Particle tracking (PT) can be used to quantify some fracture mechanics parameters and their evolution during a fast *in situ* tensile fracture test.³¹⁰ *a* Virtual tomographic slices representing typical crack-tip morphology and its evolution at various steps to failure. The images are acquired using fast tomography during a continuous tensile test for a pre-cracked AA. *b* Crack opening displacement profiles averaged across the line of the crack obtained from tomograms such as in *a* and *c* Variations in the value of J along the crack front (x) for the first six steps, obtained by PT

observed the crack surface topology, bifurcation and tip geometry using gallium to delineate the grain boundaries (which are usually invisible to CT) to understand the interaction of the crack with the grain structure. A number of crack closure studies have followed for Al-SiC³⁰⁰ and Ti-SiC composites,³⁰¹ cast iron^{302,303} and AAs.³⁰⁴ It is important to remember that closure is believed to influence crack growth though the extent to which it shields the crack-tip from the full range of the stress intensity range. In many cases tomography suggests that the faces touch well before the conventional change in sample compliance during unloading normally associated with the onset of crack face contact.³⁰⁵ This is not by itself confirmation that closure will affect crack growth since tomography cannot determine whether significant loads are borne across the faces.

Crack-tip opening displacement: As well as its importance in determining crack face contact from the point of view of closure mechanisms, the degree of opening and closing of the crack can be related directly to the crack-tip driving force. There have been a number of ways in which the crack opening displacement has been measured which fall predominantly into two groups; namely those who have measured the crack opening

directly³⁰¹ as will later be explained in Fig. 23*a* and those who have used PT (Fig. 21)^{306–308} or digital volume correlation (Fig. 22)³⁰⁹ to study the crack displacements. Figure 21 shows as an example the fracture of an aluminium sample where a sharp fatigue crack was previously introduced. The tomographic images were recorded using fast tomography (20 s for acquiring a scan with a 1.6 μm voxel size) during a continuous tensile test and the fracture mechanics J integral parameter was thus determined.

Along similar lines, DVC analysis of the movement of graphite nodules in CT images of cast iron during crack opening have been coupled to the extended finite element method (X-FEM)^{311,312} to quantify the local crack driving force along non straight cracks.³⁰⁹ An example of this is shown in Fig. 22. This highlights the synergy between imaging experiments and state of the art numerical simulation. X-FEM is first shown to both improve the crack detection thanks to the enriched Finite Element basis used in the study. This approach has also led to the concept of X-DVC, which is based on a global approach to volume correlation (as opposed to standard local approaches where patterns are recognised one by one using the correlation of sub-volumes of the image). The finite element tools also have the advantage



22 The figure shows the displacement inferred by digital volume correlation (DVC) analysis of the combining synchrotron X-ray computer tomography (CT) images.³⁰⁹ *a* Tomogram of crack in nodular cast iron, *b* displacement field surrounding the crack at max load determined by DVC from images at minimum and maximum loading, by *c* comparing extended-FEM with the DVC displacement map can infer the variation in mode I stress intensity factor along the crack front after 45 000 cycles

that they can be used directly to post-process the measured displacement field (including the singular components) to extract stress intensity factors along the crack front.

Either way, the change in the crack opening displacement (COD) during the loading cycle can be used to quantify the local crack-tip driving force. For the Ti/SiC data shown in Fig. 23*a*, it was predicted that the COD would vary as \sqrt{r} depending on the effective stress intensity³¹³

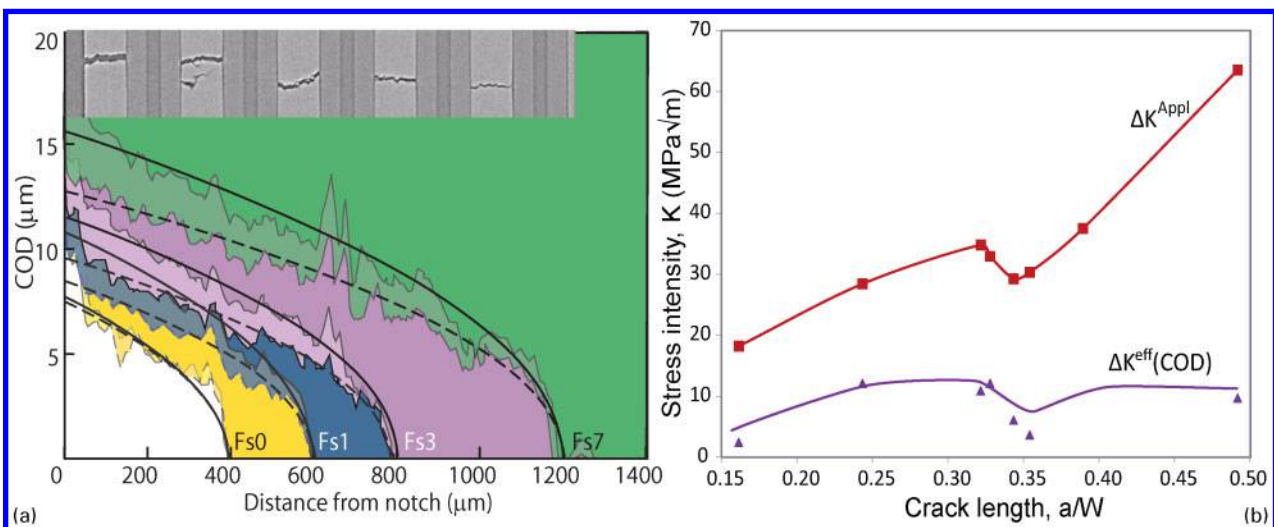
$$K^{eff} = \frac{\sqrt{2\pi}AE_cM}{8(1-v_m^2)}$$

Where, E_c is the composite stiffness, v_m the matrix Poisson's ratio, M the gradient in a linear plot of COD versus \sqrt{r} , and A an orthotropic factor (here approximately equal to 1.6). The inferred difference in stress intensity between nominal and effective ΔK is shown in

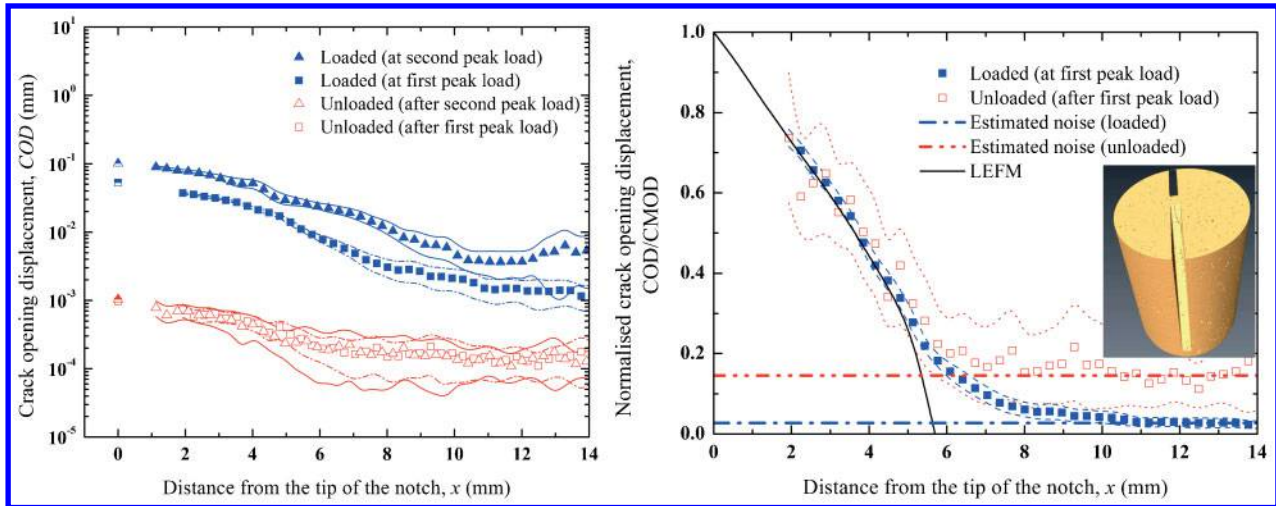
Fig. 23*b*. It is interesting to note that in this case the crack bridging SiC fibres hold the crack in the Ti matrix open at minimum load, K_{min} , because the fibres are residually in axial compression due to pre-existing thermal stresses that open the crack. At maximum load, K_{max} , the bridging fibres are in tension and hold the crack shut such that the ΔCOD is small, indicative of a very small crack driving force ΔK^{eff} compared to that nominally applied, ΔK^{AppI} (Fig. 23*b*).

Stress intensity factor: the PT and DVC methods can be used to provide a measure of the total displacement/strain field around a fatigue crack.^{256,314} This method was first used by Toda *et al.*³⁰⁶ to derive the local mode I, II and III crack driving forces K_I, K_{II}, K_{III} from the local displacement vector $u(x,y,z)$

$$K_I = \frac{1}{1+\nu} \sqrt{\frac{\pi}{2r}} \left(\frac{Eu_y h_{22} - Eu_z h_{12} - Trh_{41}}{h_{42}} \right)$$



23 *a* Crack opening displacement (COD) measured near the mid-plane for a fatigue crack observed intermittently at K_{max} (upper lines) and K_{min} (lower lines) during fatigue crack growth in a Ti-35 vol.-% 140 μm diameter SiC fibre composite along with the best fit $r^{1/2}$ curves, *b* variation in crack-tip driving force with increasing crack length compared to that nominally applied (ΔK_{AppI}) as inferred from the best fit $r^{1/2}$ curves for the COD data at K_{min} and K_{max} in a^{256}



24 **a** Distribution of crack opening displacements (COD) along crack in a chevron notched graphite sample under loaded and unloaded conditions: the bounds show the minimum and maximum values of COD along the crack front. **b** Comparison between the average COD measured by digital volume correlation (DVC) from CT images normalised by the crack mouth opening displacement (CMOD at the free surface) and finite element simulation prediction after the first loading stage: average crack length is 5.7 mm and peak load is $K_{\max}=1.60 \text{ MPa}\sqrt{\text{m}}$,³²⁴ tomogram of sample shown inset

$$K_{II} = \frac{1}{1+\nu} \sqrt{\frac{\pi}{2r}} \left(\frac{Eu_y h_{21} - Eu_z h_{11} - Tr h_{51}}{h_{52}} \right)$$

$$K_{III} = E \sqrt{\frac{\pi}{2r} \frac{u_x}{h_{31}}}$$

Where, h_{ij} are simple functions³⁰⁶ of the radial and angular distance from the crack-tip and the Poisson's ratio, ν of the solid, E is Young's modulus, T the T stress. Such displacement measurements can be compared directly with fields predicted by finite element models, for example around a crack in a notched sample of particle containing polyurethane.³¹⁵

While a great deal of the work to date has been focussed on metals and alloys, CT analyses of crack propagation are becoming more widespread in other areas, particularly with respect to more complex structured materials including 2D and 3D composite systems,^{103,291,316} self-healing systems^{111,317} and crack propagation in natural materials, e.g. bone,^{318–320} teeth,³²¹ wood,²⁶⁸ as well as graphite,³²² which is an important structural material for the nuclear industry. Mostafavi *et al.*³²³ found from surface DIC that unstable fracture is preceded by the sub-critical propagation of surface cracks having a scale similar to the microstructure. Using a chevron notch geometry to obtain straight cracks, the crack opening displacement was measured by DVC in 3D (see Fig. 24). The experimental values are consistent with the FE-predicted values and demonstrate the existence of a cohesive fracture process zone ahead of the crack-tip (Fig. 24b). This suggests that simulations of the fracture process require a material model capable of showing local softening behaviour.

Crack growth, crack bridging and crack path

Extrinsic toughening mechanisms act to slow the rate of crack growth by shielding cracks from the nominally applied crack-tip stress field. Two important mechanisms are crack deflection and bridging. It is relatively

easy to quantify the crack path and shape^{325,326} as well as the crack growth rate by incremental CT imaging.

Crack growth rate: Marrow³²⁷ measured the crack growth rate of short fatigue cracks initiating from graphite nodules in aus-tempered ductile iron by CT and found the crack growth rate to be very uneven with periods of fast growth rate, punctuated by periods when it is essentially arrested. Buffiere *et al.*^{191,325} have looked at the morphology of cracks and correlated this to the crack growth rate of longer cracks as a function of fatigue cycling. To quantify the relationship between crack growth and grain orientation³²⁸ or the nature of the grain boundaries¹⁵² it has been necessary to exploit the grain mapping methods summarised in the 'Crystal grain imaging' section¹⁵² or undertake post mortem electron back scattered analysis.³²⁹ Biroscia *et al.*^{330,331} created three types of microstructure for dual phase titanium alloy, namely lamellar, duplex and a heterogeneous combination of the two. Of these, the lamellar microstructure displayed the fastest and the duplex microstructure, the slowest crack growth rate. Computer tomography showed that a columnar lamellar microstructure creates a relatively smooth crack front while a basket-weave type microstructure forces the crack-tip to undulate on the lath width scale. Vast differences in the extent of crack growth rate between the interior and surface have been revealed by CT for nuclear grade graphite such that without CT, fracture mechanics analysis would be totally misleading.³²² The relationship between microcracking in alumina and grain orientation has been examined though a combination of conventional CT to identify the microcracking and DCT to map the grain orientations.³³²

Crack deflection and bridging: In many cases a key aspect in crack-tip shielding is the presence of bridging ligaments. While these can be imaged qualitatively in a straightforward manner, quantitative analysis is more difficult; Babout *et al.*³³³ have developed algorithms that allow the tracking of the location and extent of the bridging ligaments as they neck down while the main crack progresses further downstream. Other works have

focussed on crack deflection and crack bridging of both transgranular³²⁸ and intergranular crack growth.³³⁴

Many natural materials are extremely anisotropic giving rise to extensive crack deflection, e.g. wood, sea-shells, bone, enamel/dentin and elephant tusk. For example, for bone, three-dimensional imaging of cracks growing transverse to the length of the bone shows marked crack deflections and (out-of-plane) twists as it interacts with the underlying haversian structure.^{335,336} This is a major source of toughening for cracks grown in this orientation. For cracks growing along the length of the bone, microcracks tend to form ahead of the crack along the lines of the haversian canals, which then give rise to crack bridging as they join the primary crack. The increased osteonal density in older bone leads to smaller and less frequent crack bridges and correlates with the marked reduction in the slope of the *R* curves with age.^{319,337} This toughening mechanism is less effective than the crack deflection that arises when a crack grows transverse to the length of the bone.

Void/Damage evolution

There is an interest in the evolution of voids both in terms of their elimination during manufacturing of powder metallurgy components and their nucleation and growth in service leading up to failure. During manufacturing CT has been used to quantify the relationship between void size and morphology and densification and to understand the contribution of plastic flow, diffusion and other densification processes for metals,^{338,339} ceramics^{257,340} and even for ice.³⁴¹ During life, the growth rate of particular families of tension or creep cavities are of interest. Perhaps one of the first to quantify the evolution of damage during straining was Buffiere *et al.*²⁰⁵ later followed in the studies in Refs. 206 and 342 who found that in low strength aluminium alloy–zirconia/silica particle composites, matrix voiding and particle matrix decohesion were the dominant mechanisms of damage accumulation whereas for stronger matrices, particle cracking was more common (see Fig. 25).

The capability of 3D imaging to quantify separately the nucleation of new cavities,³⁴³ their growth³⁴⁴ and finally their coalescence³⁴⁵ has also renewed the interest of the experimental study of ductile damage during tensile deformation at room and high temperature in engineering materials.^{345–347} In a series of studies on ductile fracture of steels^{348,349} and AAs, it has, for instance, been shown that rather than tediously trying to follow each cavity in the entire population (sometimes amounting to thousands of individuals cavities), cavity growth was much more easily quantified using the average diameter of the largest cavities in the population. Cavity growth has then been experimentally quantified with some confidence and this is currently being compared with the prediction of various cavity growth models.

A number of *in situ* and *ex situ* creep studies have also been carried out. For instance, copper was tested at 50% of the melting temperature indicating that growth of voids with radii of a few microns is determined by a viscous flow mechanism.⁹⁹ By following the evolution of individual voids it was concluded that void coalescence follows two stable growth regimes involving the impingement of neighbouring primary voids, followed by the coalescence of secondary voids before final

rupture.³⁵⁰ For Al+Al₂O₃ particle containing composite, there is a change in the damage mechanism with matrix delamination and matrix voiding occurring at high temperature (300°C) but particle fracture contributing at 200°C.³⁵¹ The pore volumes and number increase linearly with strain but exponentially with time such that the average pore size remains essentially constant.

In an investigation of the creep of a brass alloy (Cu–40Zn–2Pb), the evolution of the shape and size of creep cavities was followed as a function of time by synchrotron X-ray tomography⁴⁹ (Fig. 26). Traditional metallographic observations suggested that their shape ranges from almost spherical to a crack-like morphology for comparatively large cavities depending on the loading conditions.³⁵² Four types of cavity were identified by CT.³⁵³ In the initial state, ellipsoidal cavities were dominant, but as creep progressed, while the total volume of all four types of cavities increased, the volume of spheres and rods grew far less rapidly than did ellipsoidal and complex shaped cavities. The predominance of ellipsoids and their total volume during primary and early stage of tertiary creep (a true secondary creep regime was not observed) suggests that surface diffusion around the cavity is rapid enough to maintain the shape of the growing cavity³⁵⁴ at this stage. A rapid increase in the volume of the complex cavities was noted when tertiary stage creep became more pronounced.

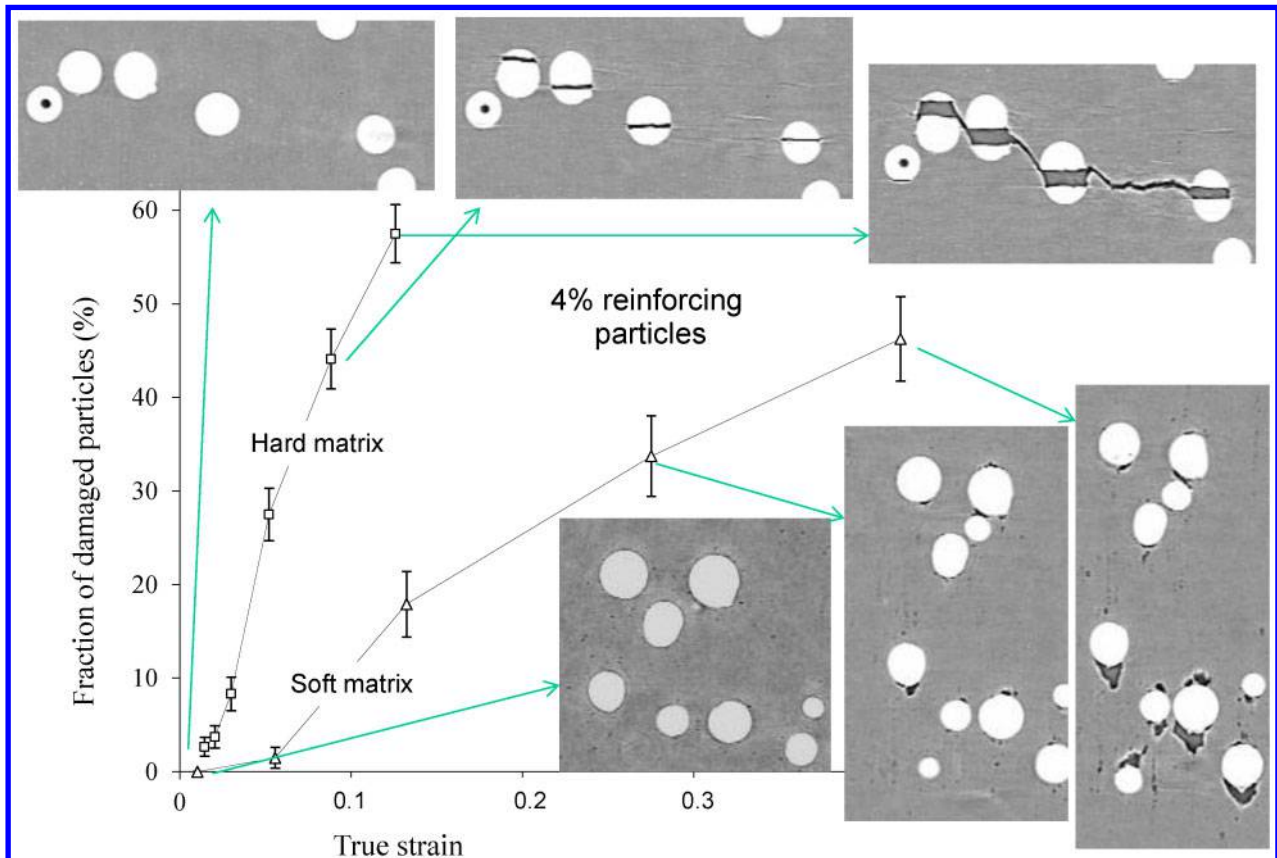
In this field, it is becoming clear that, allowing the observation of the interior of a sample without requiring a specific (and possibly biasing) preparation procedure, X-ray tomography is the best way to obtain reliable information on the evolution of cavities during loading (mechanical or thermal). This has enabled many, well established and widely used modelling theories in this field to be revisited. Some have been validated (e.g. the Huang model for damage growth during ductile fracture³⁴⁴) and the weaknesses of some of the others highlighted (e.g. Brown and Embury criterion for void coalescence in ductile fracture³⁴⁵).

This has to be applied with caution though, mainly because the resolution has to be high enough to allow the visualisation of all the cavities of interest many of which can be quite small.

Corrosion

X-ray tomography is finding increased application in the study of corrosion.^{355–358} This is in part because gross measures of corrosion such as weight gain and electrochemical activity tell one little about the location and extent of localised corrosion, which can often be the biggest concern and often because small features at the surface belie extensive sub-surface corrosion. Localised corrosion rates can be many orders of magnitude greater than for general corrosion. CT is particularly useful for pitting corrosion or other cases where a small entrance hole conceals extensive sub-surface corrosion. In this section we will concentrate on example cases where quantitative tomography has been applied.

The grain boundary relationships are critical to controlling intergranular stress corrosion cracking, for example of stainless steel. Conventional CT is an excellent way of following the growth of SCC cracks over time,³⁵⁶ but DCT provides a means of mapping the boundary orientations along the crack path. Through



25 Quantifying the extent of particle cracking and particle/matrix decohesion in high strength and low matrix strength Al metal matrix composites containing 4% spherical ceramic particles. Tomography is needed because the damage of near surface particles is not representative of the bulk. Re-arranged from Ref. 206

such a quantitative analysis it is possible to identify the nature of the grain boundaries that are resistant to SCC (see Fig. 27). King *et al.*^{152,359} have shown that a range of grain boundaries have 'special' properties and may be involved in crack bridging during SCC, not just low coincidence site twin variant grain boundaries ($\Sigma 3$). These include $\Sigma 1$, $\Sigma 3$, $\Sigma 9$ and $\Sigma 11$ boundaries with low hkl planes on either side.

Corrosion is not always something to be avoided; there is now a serious focus on biodegradable Mg implants for medical applications. However, the degradation process

needs careful control as magnesium corrosion creates H gas. If the local hydrogen saturation of blood and tissues are exceeded, hydrogen gas accumulates in tissue cavities. Witte *et al.*³⁶⁰ have studied the use of coatings to slow corrosion to acceptable rates (see Fig. 28) using thresholding techniques to quantify the volume lost to corrosion.

Modelling based on X-ray tomography images

The use of tomographic images, both to set up geometrical models of materials and also to validate their performance in predicting structural changes is an emerging trend in materials science. We first describe briefly the available procedures to mesh the tomograms before giving an extensive review of the recent papers using this technique.

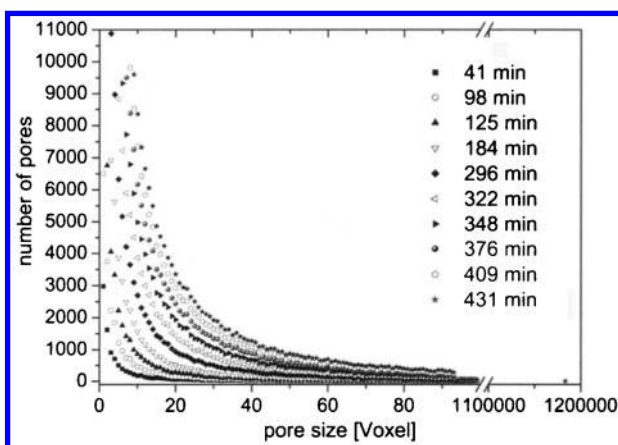
Mesh generation

It has been proposed in Ref. 361 to classify the different approaches for generating a mesh that is microstructurally faithful into three families:

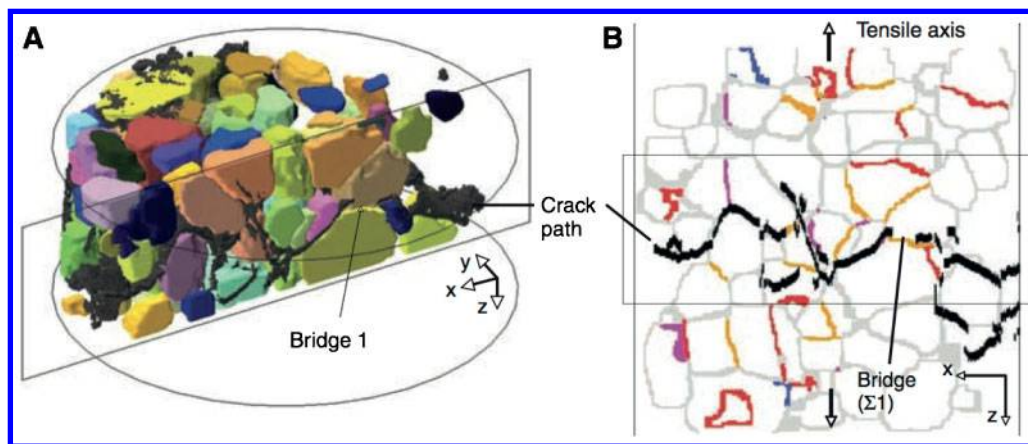
- Method 1: meshes using beam or shell elements,
- Method 2: voxel based quadratic meshes,
- Method 3: tetrahedral meshes filling a surface made of triangular elements

Figure 29 shows a visual sketch of this classification. It appears that the most popular method is the third type.

In all cases, one of the main issues is to capture sufficient geometrical detail to be faithful to the image



26 Quantification of the number and size of voids during creep for Brass (58 wt-% Cu; 40 wt-% Zn; 2 wt-% Pb) crept at 375°C under a load of 25 MPa⁴⁹



27 Combined use of diffraction contrast tomography (DCT) and computer tomography (CT) data to identify the nature of crack bridging grain boundary relationships during stress corrosion cracking of stainless steel. *a* Cracks obtained from CT data are shown in black, at the final step before sample failure, and compared with DCT data of 3D grain shapes. *b* 2D section of the grain boundaries identified by DCT (low angle $\Sigma 1$ orange; $\Sigma 3$ red; $\Sigma 9$ blue; other boundaries $\Sigma < 29$ purple) compared with the crack path (black) identified by CT¹⁵²

based microstructure, while at the same time keeping the number of finite elements computationally tractable. Overmeshing is the main limitation of these methods as the images are sometimes so big that the number of elements exceeds the capacity of the standard commercial codes. Four methods have been investigated to overcome this issue: down sampling (or binning) explored, for instance, in Refs. 255 and 362, the use of a dedicated FE code as suggested by Roberts and Garboczi,³⁶³ the parallelisation of standard FE codes such as paraFEM (www.parafem.org.uk), for example in Ref. 364 or in Madi *et al.*³⁶⁵ and finally techniques based on the Fast Fourier Transform (FFT) initially developed by Moulinec and Suquet.^{366–370} Figure 30 gives examples of several meshes published in the literature.

As an alternative to Finite Elements, Discrete Element methods are becoming increasingly applied, e.g. for asphalt³⁷³ for concrete³⁷⁴ and for packing of powders and beads.³⁷⁵

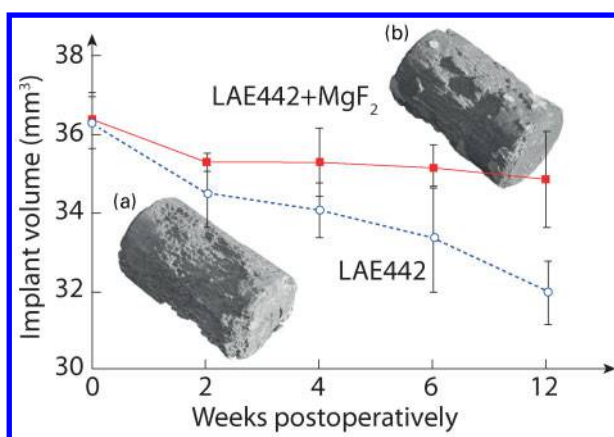
Image based modelling of cellular/porous materials

The literature on image based modelling of cellular materials is extensive, covering a wide range of morphologies, foams, honeycombs, felts, etc. FE has been shown to be an ideal method to analyse the stress distribution within such complex architectures. Most of the research focuses on the mechanical/deformation behaviour but other properties are also considered. Amongst the recent studies, some are dedicated to cellular materials in general,^{362,376–380} others focus on specific types of cellular materials including metals,^{372,381–390} ceramics,^{257,391–394} polymers,^{395–397} carbon,³⁹⁸ nuclear graphite³⁹⁹ and even bread.⁴⁰⁰ In some cases FE simulations have been run side by side with *in situ* deformation under CT observation to compare their predictive capability both locally on a strut-by-strut basis and globally in terms of Poisson's ratio and Young's modulus, for example for conventional versus auxetic open cell foams.¹⁹²

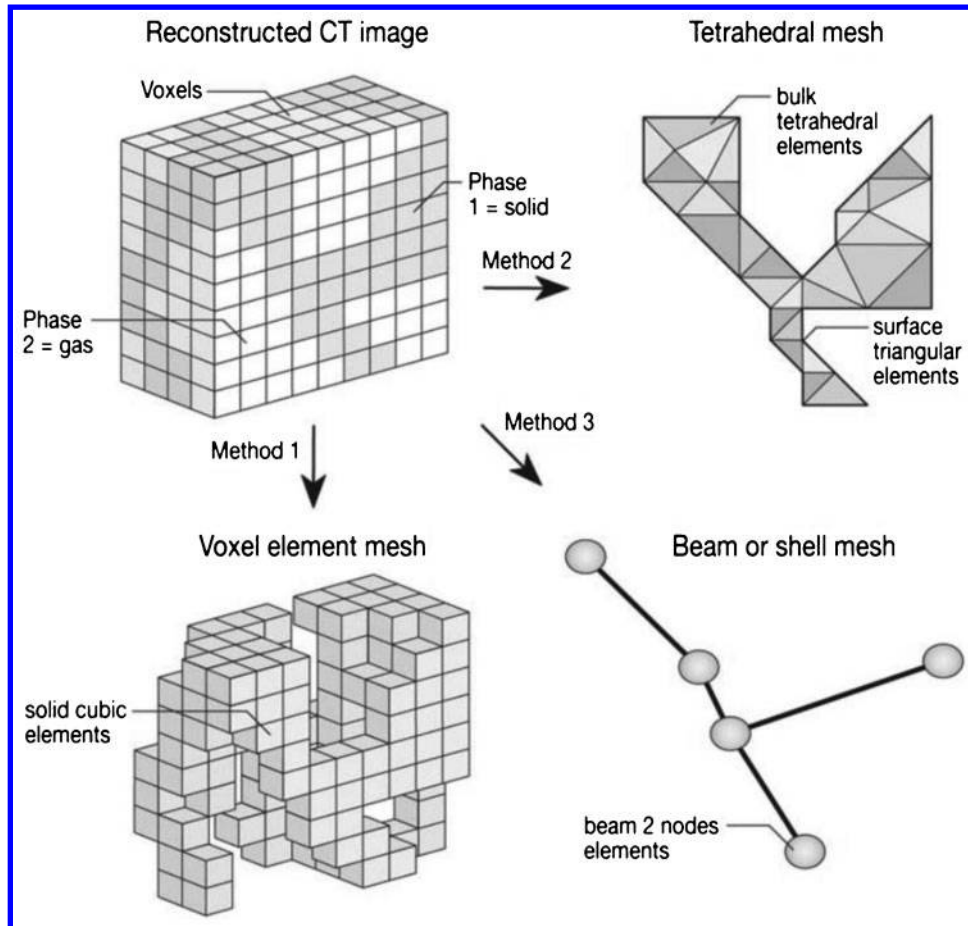
Fischer proposes an alternative to direct image based modelling.³⁷⁶ First, the size distribution of the foam pores was determined by CT and this was mimicked

using a tessellation of modified Kelvin cell units or truncated octahedrons of various cell sizes to build representative finite element meshes from which the compressive behaviour of the polymer foams could be predicted.

A key question for many porous systems, from building materials, fuel cells, bioglass scaffolds to oil containing rock, is their permeability to fluids. Transport properties can also efficiently be calculated, starting from the 3D reconstruction of the microstructure, either directly from the images using FE calculation (see Fig. 31), by a discrete volume method^{401–403} or by constructing a simplified network and using a lattice-Boltzmann (LB) method (see Fig. 16). This was achieved for cellular solids in Refs. 404 and 405, for asphalt concrete in Ref. 406, for porous alumina in Ref. 407 catalysts²³⁴ and for bioscaffold pores in Refs. 408 and 409. Network approaches to porous systems such as carbonates have also been developed.²²⁹



28 The implant volume of LAE442 and magnesium fluoride (MgF_2)-coated Mg alloy LAE442 at different post-operative intervals. Results were obtained from computer tomography (CT) images. The morphology of *in vivo* corroded *a* magnesium alloy LAE442 and *b* magnesium fluoride-coated LAE442, 12 weeks post-operatively are shown inset. The dominant corrosion morphology was pitting corrosion (*a* and *b*)³⁶⁰



29 Visual sketch of the different methods available for meshing 3D images, adapted from Ref. 361

Open cell metallic foams have great potential for removing heat. FE modelling can help to optimise the thermal transport *v.* weight *v.* mechanical properties *v.* geometry design challenge. Some studies have used actual reconstruction of microstructure as direct inputs for predicting thermal properties (mostly radiative and conductive properties). This has mainly been achieved for highly porous materials.^{410–413} The thermal properties of nuclear graphite are also of technological concern and have been predicted directly from CT images.⁴¹⁴

Image based modelling of composites and multiphase materials

Another important category of materials particularly suited to the image based modelling are composites. Here the 3D structure of the reinforcement plays a first order role on the properties, and the direct meshing of tomograms can provide a feast of information on how the local and global properties relate to the microstructure. Work has been carried out on metal matrix composites^{415–417} and fibre composites.^{418–421} For example, Fig. 32 shows the typical results obtained using this method for a woven C–C composite. The figure illustrates how such a calculation yields both local and global information.

Finally, many bulk multiphase materials have also been analysed by CT image based modelling. Asphalt has been treated in several studies,^{422–424} mortar by FFT in Ref. 368, multiphase ceramics in Refs. 365 and 425 and metals in Refs 370 and 426–430. In a recent study, Moulin *et al.*⁴³¹ suggest a physically based criterion for

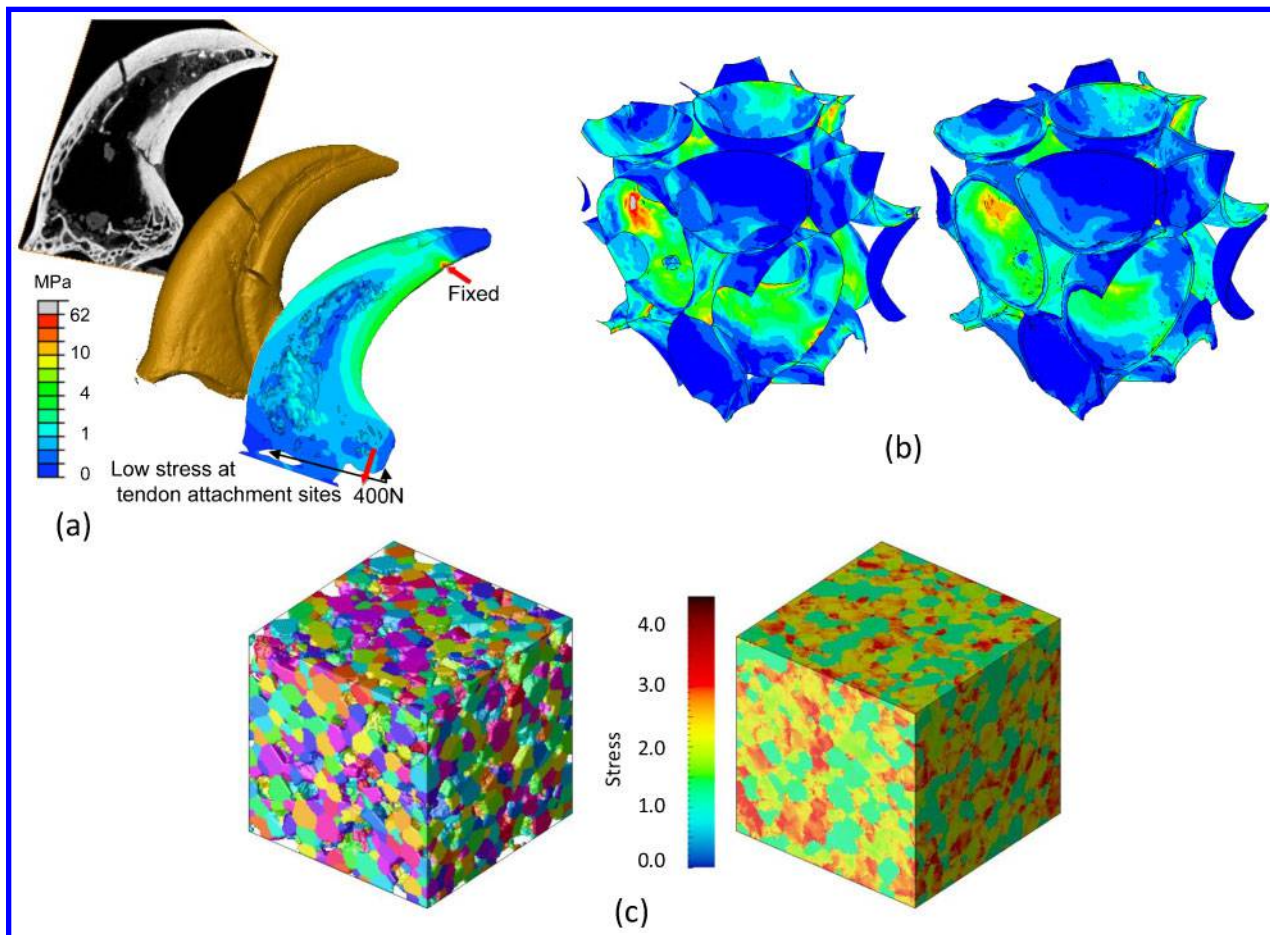
the fracture of complex shape inclusions embedded in a plastically deforming matrix. To apply this criterion, it is necessary to relate the stress concentration in the inclusions with the size of the volume over which this stress is reached.

In Berre *et al.*,⁴³² the local value of the grey levels in the reconstructed tomograms are used to measure the local density in a nuclear graphite and to generate a multiphase model. The density is then used to modulate the Young's modulus and resistance of the local element and a finite element calculation is performed to account for these fluctuations and calculate the macroscopic behaviour for samples with different structures.

Polycrystal properties

Currently there is a great deal of interest in developing numerical models of materials behaviour at the grain scale. In the past, representative microstructures have been generated numerically³⁶⁴ or by successive EBSD acquisition and destructive layer removal,^{433–437} but this is time consuming, destructive and can only map a small volume.

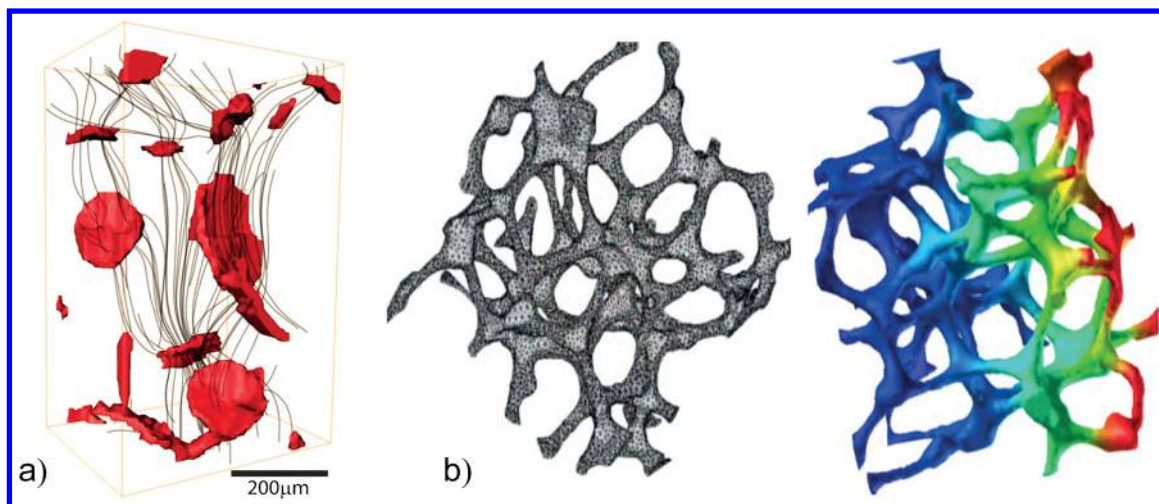
Techniques capable of mapping grain orientations in 3D such as DCT ('Crystal grain imaging' section) are beginning to find application as a means of developing image based polycrystalline models to predict, for example, plastic deformation, microcracking and inter-granular stress corrosion cracking. Further, in a number of cases it is possible to probe the micromechanical response of individual grains within a polycrystalline aggregate *in situ*.



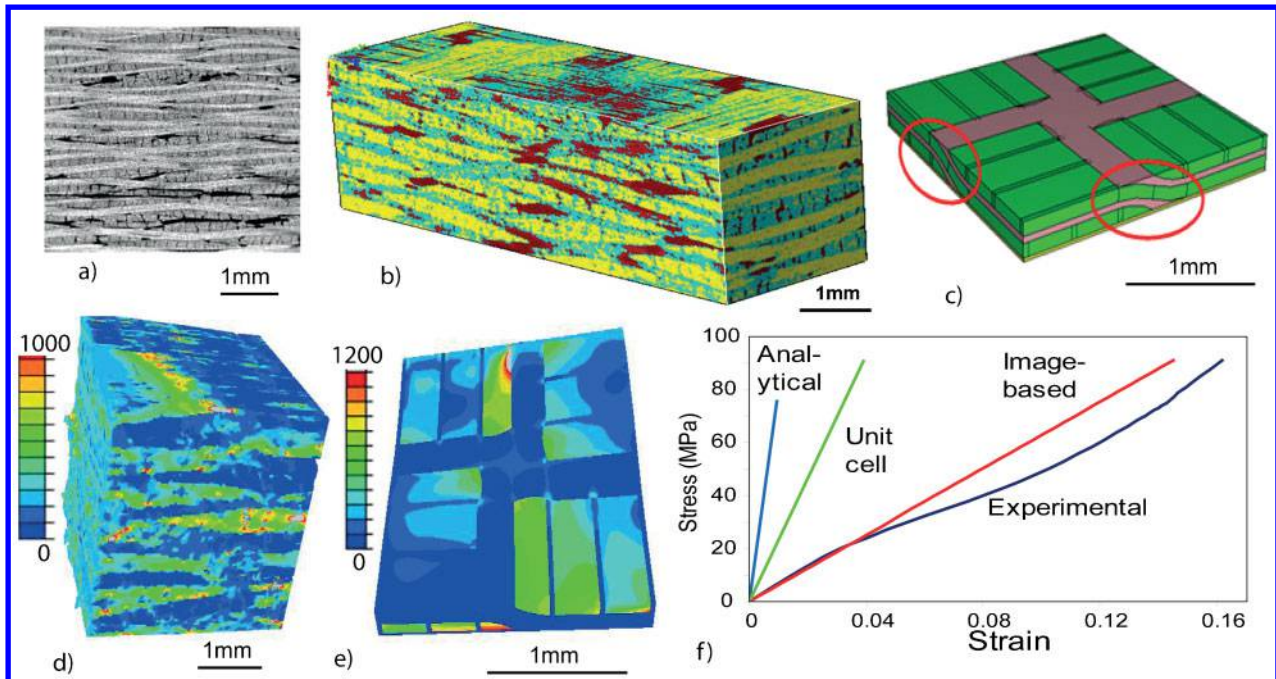
30 Examples of mesh geometries created from tomographic images; *a* tetrahedral mesh: contour map of Mises stress through the mid-section of a (repaired) velociraptor claw loaded at the tendon location and constrained at the tip;³⁷¹ *b* shell mesh: contour map of the Mises stress calculated with shell elements based on a tomogram of a steel hollow sphere structure (left); the result of the calculation is also compared with a mesh of the same tomogram with tetrahedral elements showing similar trends (right), adapted from Ref. 372; *c* Voxel mesh: Fast Fourier Transform (FFT) calculation of the elastic stress field (left). The mesh is generated from a numerical, two-phase digital material containing isotropically coarsened particles surrounded by a matrix phase, generated through a Kinetic Monte Carlo Potts model for Ostwald ripening (right)³⁷⁰

Full 3D polycrystalline models can be input directly into crystal plasticity finite element models to predict the heterogeneity of plastic deformation at the intergranular

level.^{154,438} Others have focussed primarily on capturing the local reorientations arising from polycrystalline deformation, for example Wang *et al.*⁴³⁹ have compared



31 Tomograms can act as the basis for subsequent finite element predictions of performance. In *a* fluid dynamics is used to predict flow through the pores of a bioscaffold⁴⁰⁹ and in *b* thermal transport through an open cell metallic foam (Alufoam) is computationally modelled (*b* courtesy P. M. Mummery)



32 **a** Fully graphitised woven C-C composite. **b** an image based mesh showing red=porosity, blue=fibres+matrix in direction 1, yellow=fibres+matrix in direction 2 (courtesy Mummery), **c** the unit cell model extends ($\sim 0.5 \times 2 \times 2$ mm) Von Mises stress maps (in MPa) for **d** the image based mesh ($\sim 2.5 \times 2.5 \times 2.5$ mm) and the **e** unit cell and **f** the corresponding comparison of the elastic loading response for the actual composite and the various models⁴¹⁹

image based crystal plasticity predictions with *in situ* measurements of local reorientation made by 3D X-ray microscopy. The grain orientations can also affect the elastic development of thermal contraction stresses for materials having non-cubic crystals systems. Using DCT to build a polycrystalline model of alumina, Gonzalez *et al.*³³² have been able to predict the intergranular stresses arising from a combination of thermal residual stresses and mechanically applied compression. These predictions have been compared with strains inferred from the DCT measurements as well as the onset and location of intergranular microcracking recorded by conventional CT.

Grain scale models can also be used for analysing corrosion resistance already exposed in 'Corrosion' section. For intergranular stress corrosion, the grain boundary nature is important in terms of the susceptibility to corrosion. Simonovski *et al.* have taken DCT measurements of a polycrystalline stainless steel wire as the basis of an image based model (see 'Polycrystal properties' section) of intergranular stress corrosion cracking^{440,441} and produced a mesh such as that shown in Fig. 33a. The experimentally determined lattice orientations were then employed to distinguish between resistant low-energy and susceptible high-energy grain boundaries in the model (Fig. 33b).

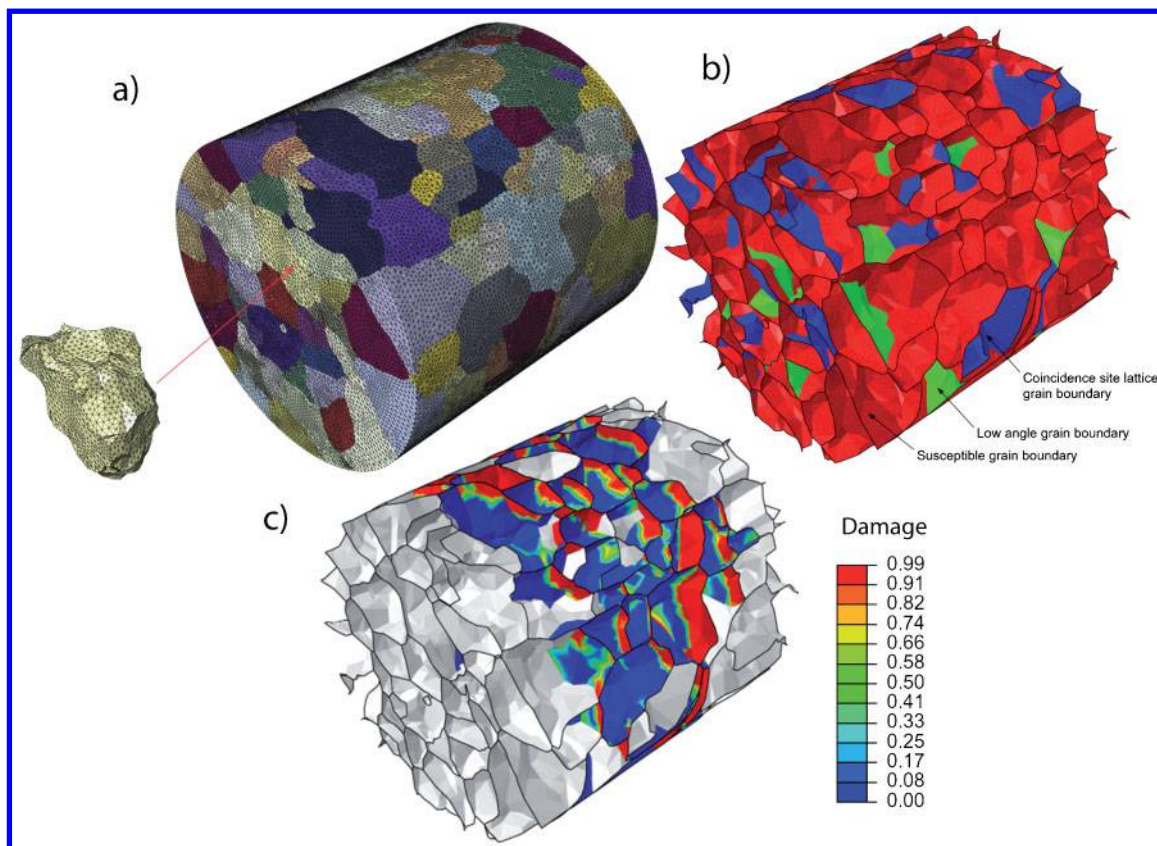
Concluding remarks and future trends

X-ray micro-CT has come a very long way over the last 20 years both in terms of spatial and temporal resolution, and the degree to which 3D images and 3D image sequences are quantified. It is now customary to spend 10–100 \times longer analysing datasets, compared to the time taken to capture them. Yet, many researchers are still only able to extract fairly rudimentary metrics to quantify the geometrical and temporal features of their

images. The availability of open source and proprietary software toolboxes for image quantification are likely to expand the degree to which users can extract useful information about their samples non-destructively. Further, correlative tomography⁸¹ analogous to correlative microscopy can bring together different measurements tools (e.g. X-ray tomography and fluorescence, scanning electron microscopy, etc) to image the same 3D features or tracking features over multiple length scales (e.g. the macroscopic and atomic nature of an intergranular crack) will become more common. Whether a laboratory source or a synchrotron X-ray source will be used in the future will probably be determined less by spatial resolution than by the timescale of the events that one wishes to follow.

Currently limitations still remain; the great proportion of images are reconstructed using FBP. In cases that involve very noisy data or too few projections they would be better suited to emerging iterative reconstruction techniques. In many situations prior knowledge of the object (e.g. the number of phases, morphologies, etc.) should be incorporated into the reconstruction algorithm as prior information. Indeed in some circumstances, it may be possible to introduce certain morphological and phase fraction metrics into the interactive reconstruction so as to quantify the desired metrics directly as a part of the reconstruction process, e.g. to identify the optimal size of the pores in the volume image that are most consistent with the projection data, rather than leaving the quantification to a post-reconstruction image analysis step. Similarly, at present images come without error bars; iterative methods would allow us to evaluate the probability that water would permeate a foam or a composite would conduct electrically.

The widespread use of iterative reconstructions is unlikely until instrument providers either provide other reconstruction codes, or at least the necessary forward



33 a FE mesh of the grain structure obtained by diffraction contrast tomography (DCT), b grain boundaries in the FE model: red: corrosion susceptible and green: low angle and blue: coincidence site lattice R3–R29 grain boundaries and c damage development in susceptible grain boundaries, red indicates fully developed crack⁴⁴¹

models, such that they can be seamlessly deployable on data collected on their instruments. Except for the simplest features (e.g. particle size, volume fraction, etc.), metrics obtained by image quantification such as permeability rarely come with error bars. Spatial resolutions of instruments are still on the whole poorly defined even for radiographs, let alone tomographs, and higher spatial resolutions are usually obtained at the sacrifice of small sample sizes. Region of interest tomography is still an emerging and underused strategy.¹⁸⁹

Nevertheless, looking back, there can be little doubt that the use and application of X-ray tomography is likely to grow significantly, especially for following structural evolution over time, whether during manufacturing, throughout service or in understanding the events leading to failure. In this respect, it promises to accelerate the materials design process and lead to safer, longer product lives.

Acknowledgement

The authors are particularly grateful to the instrument scientists and manufacturers who helped with compiling and discussing the form of Figs. 1 and 5 and comments from Profs. A. Mortensen, W. Lionheart and S. Stock as well as the referees. In addition PJW is grateful for funding from the BP International Centre for Advanced Materials, UoM and the EPSRC for funding the Manchester X-ray Imaging Facility under grants EP/F007906, EP/F028431 and EP/I02249X and for accommodation within the Research Complex at Harwell. New algorithms for the analysis of CT images are being

developed as part of the Collaborative Computational Project CCPi being funded by EPSRC under the grant EP/J010456/1.

References

1. S. R. Stock: 'X-ray microtomography of materials', *Int. Mat. Rev.*, 1999, **44**, 141–164.
2. S. R. Stock: 'Recent advances in X-ray microtomography applied to materials', *Int. Mater. Rev.*, 2008, **53**, (3), 129–181.
3. S. R. Stock: 'Microcomputed tomography: methodology and applications', 336; 2009, Boca Raton, FL, CRC Press.
4. J. Baruchel, J.-Y. Buffiere, E. Maire, P. Merie and G. Peix (eds.): 'X-ray tomography in material science', 204; 2000, Hermes Paris, France.
5. J. Banhart: 'Advanced tomographic methods in materials research and engineering', 490; 2008, OUP Oxford. 2008, Oxford, Oxford University Press.
6. C. Rau, A. Somogyi and A. Simionovici: 'Microimaging and tomography with chemical speciation', *Nucl. Instrum. Methods Phys. Res. B*, 2003, **200**, 444–450.
7. S. D. M. Jacques, C. K. Egan, M. D. Wilson, M. C. Veale, P. Seller and R. J. Cernik: 'A laboratory system for element specific hyperspectral X-ray imaging', *Analyst*, 2013, **138**, (3), 755–759.
8. S. W. Wilkins, T. E. Gureyev, D. Gao, A. Pogany and A. W. Stevenson: 'Phase-contrast imaging using polychromatic hard X-rays', *Nature*, 1996, **384**, 335–338.
9. P. C. Diemoz, A. Bravin and P. Coan: 'Theoretical comparison of three X-ray phase-contrast imaging techniques: propagation-based imaging, analyzer-based imaging and grating interferometry', *Opt. Express*, 2012, **20**, (3), 2789–2805.
10. P. Cloetens, R. Barrett, J. Baruchel, J.-P. Guigay and M. Schlenker: 'Phase objects in synchrotron radiation hard X-ray imaging', *J. Phys. D: Appl. Phys.*, 1996, **29**, 133–146.
11. S. C. Mayo, A. W. Stevenson and S. W. Wilkins: 'In-line phase-contrast X-ray imaging and tomography for materials science', *Materials*, 2012, **5**, (5), 937–965.

12. D. Paganin, S. C. Mayo, T. E. Gureyev, P. R. Miller and S. W. Wilkins: 'Simultaneous phase and amplitude extraction from a single defocused image of a homogeneous object', *J. Microsc.*, 2002, **206**, 33–40.
13. S. Sanchez, P. E. Ahlberg, K. M. Trinajstić, A. Mirone and P. Tafforeau: 'Three dimensional synchrotron virtual paleohistology: a new insight into the world of fossil bone', *Microsc. Microanal.*, 2012, **18**, (5), 1095–105.
14. M. Lak, D. Neraudeau, A. Nel, P. Cloetens, V. Perrichot and P. Tafforeau: 'Phase contrast X-ray synchrotron imaging: opening access to fossil inclusions in opaque amber', *Microsc. Microanal.*, 2008, **14**, (3), 251–259.
15. D. Penney, A. McNeil, D. I. Green, R. Bradley, Y. M. Marusik, P. J. Withers and R. F. Preziosi: 'A new species of anapid spider (Araneae: Araneoidea, Anapidae) in Eocene Baltic amber, imaged using phase contrast X-ray computed micro-tomography', *Zootaxa*, 2011, **2742**, 60–66.
16. J. A. Dunlop, S. Wirth, D. Penney, A. McNeil, R. S. Bradley, P. J. Withers and R. F. Preziosi: 'A minute fossil phoretic mite recovered by phase-contrast X-ray computed tomography', *Biol. Lett.*, 2012, **8**, (3), 457–460.
17. R. S. Bradley, A. McNeil and P. J. Withers: 'An examination of phase retrieval algorithms as applied to phase contrast tomography using laboratory sources', Developments in X-Ray tomography VII, *Proc.SPIE*, 2010, **7804**, 780404, doi:10.1117/12.860536.
18. T. J. Davis, D. Gao, T. E. Gureyev, A. W. Stevenson and S. W. Wilkins: 'Phase-contrast imaging of weakly absorbing materials using hard X-rays', *Nature*, 1995, **373**, (6515), 595–598.
19. D. Chapman, W. Thomlinson, R. E. Johnston, D. Washburn, E. Pisano, N. Gmur, Z. Zhong, R. Menk, F. Arfelli and D. Sayers: 'Diffraction enhanced X-ray imaging', *Phys. Med. Biol.*, 1997, **42**, (11), 2015–2025.
20. E. Forster, K. Goetz and P. Zaumseil: 'Double crystal diffractometry for the characterization of targets for laser fusion experiments', *Krist. Tech.*, 1980, **15**, (8), 937–945.
21. K. Goetz, M. P. Kalashnikov, Y. A. Mikhailov, G. V. Sklizkov, S. I. Fedotov, E. Foerster and P. Zaumseil: 'Measurement of parameters of shell targets for laser fusion with the use of X-ray schlieren technique', *Kvantovaya Elektron.*, 1979, **6**, (5), 1037–1042.
22. C. David, B. Nohammer, H. H. Solak and E. Ziegler: 'Differential X-ray phase contrast imaging using a shearing interferometer', *Appl. Phys. Lett.*, 2002, **81**, (17), 3287–3289.
23. T. Weitkamp, A. Diaz, C. David, F. Pfeiffer, M. Stampanoni, P. Cloetens and E. Ziegler: 'X-ray phase imaging with a grating interferometer', *Opt. Express*, 2005, **13**, (16), 6296–6304.
24. M. Bech, T. H. Jensen, R. Feidenhans'l, O. Bunk, C. David and F. Pfeiffer: 'Soft-tissue phase-contrast tomography with an X-ray tube source', *Phys. Med. Biol.*, 2009, **54**, (9), 2747–2753.
25. F. Pfeiffer, T. Weitkamp, O. Bunk and C. David: 'Phase retrieval and differential phase-contrast imaging with low-brilliance X-ray sources', *Nature Phys.*, 2006, **2**, (4), 258–261.
26. A. Tkachuk, F. Diewer, H. Cui, M. Feser, S. Wang and W. Yun: 'X-ray computed tomography in Zernike phase contrast mode at 8 keV with 50-nm resolution using Cu rotating anode X-ray source', *Z. Kristallogr.*, 2007, **222**, (11), 650–655.
27. C. Holzner, M. Feser, S. Vogt, B. Hornberger, S. B. Baines and C. Jacobsen: 'Zernike phase contrast in scanning microscopy with X-rays', *Nat. Phys.*, 2010, **6**, (11), 883–887.
28. J. C. Andrews, E. Almeida, M. C. H. van der Meulen, J. S. Alwood, C. Lee, Y. J. Liu, J. Chen, F. Meirer, M. Feser, J. Gelb, J. Rudati, A. Tkachuk, W. B. Yun and P. Pianetta: 'Nanoscale X-ray microscopic imaging of mammalian mineralized tissue', *Microsc. Microanal.*, 2010, **16**, (3), 327–336.
29. J. W. Miao, P. Charalambous, J. Kirz and D. Sayre: 'Extending the methodology of X-ray crystallography to allow imaging of micrometre-sized non-crystalline specimens', *Nature*, 1999, **400**, (6742), 342–344.
30. M. Di Michiel, J. M. Merino, D. Fernandez-Carreiras, T. Buslaps, V. Honkimaki, P. Falus, T. Martins and O. Svensson: 'Fast microtomography using high energy synchrotron radiation', *Rev. Sci. Instrum.*, 2005, **76**, (4), Art No. 043702.
31. L. Salvo, P. Cloetens, E. Maire, S. Zabler, J. J. Blandin, J. Y. Buffiere, W. Ludwig, E. Boller, D. Bellet and C. Jossier: 'X-ray micro-tomography an attractive characterisation technique in materials science', *Nucl. Instrum. Methods Phys. Res. B*, 2003, **200**, 273–286.
32. R. Mokso, F. Marone, D. Habertuer, J. C. Schittny, G. Mikuljan, A. Isenegger and M. Stampanoni: 'Following dynamic processes by X-ray tomographic microscopy with sub-second temporal resolution', in '10th International Conference on X-Ray Microscopy', (eds. I. McNulty, *et al.*), 38–41; 2011. Melville, NY, American Institute of Physics, 2011.
33. A. A. MacDowell, D. Y. Parkinson, A. Haboub, E. Schaible, J. R. Nasiatka, C. A. Yee, J. R. Jameson, J. B. Ajo-Franklin, C. R. Brodersen and A. J. McElrone: 'X-ray micro-tomography at the Advanced Light Source', Developments in X-Ray tomography VIII, *Proc.SPIE*, 2012, **8506**, 850618, doi:10.1117/12.930243.
34. O. Ludwig, M. Dimichiel, L. Salvo, M. Suery and P. Falus: 'In-situ three-dimensional microstructural investigation of solidification of an Al-Cu alloy by ultrafast X-ray microtomography', *Metall. Mater. Trans. A*, 2005, **36A**, (6), 1515–1523.
35. P. Babin, G. Della Valle, H. Chiron, P. Cloetens, J. Hozzowska, P. Pernot, A. L. Reguerre, L. Salvo and R. Dendievel: 'Fast X-ray tomography analysis of bubble growth and foam setting during breadmaking', *J. Cereal Sci.*, 2006, **43**, (3), 393–397.
36. S. Terzi, L. Salvo, M. Suery, A. K. Dahle and E. Boller: 'Coarsening mechanisms in a dendritic Al-10% Cu alloy', *Acta Mater.*, 2010, **58**, (1), 20–30.
37. N. Limodin, L. Salvo, M. Suery and M. DiMichiel: 'In situ investigation by X-ray tomography of the overall and local microstructural changes occurring during partial remelting of an Al-15.8 wt.% Cu alloy', *Acta Mater.*, 2007, **55**, (9), 3177–3191.
38. D. Tolnai, G. Requena, P. Cloetens, J. Lendvai and H. P. Degischer: 'Sub-micrometre holotomographic characterisation of the effects of solution heat treatment on an AlMg7-3Si3-5 alloy', *Mater. Sci. Eng. A Struct. Mater.*, 2012, **550**, 214–221.
39. K. Uesugi, M. Hoshino, A. Takeuchi, Y. Suzuki, N. Yagi and T. Nakano: 'Development of fast (sub-minute) micro-tomography', AIP Conference Proceedings, 2010, 47–50. Melville, NY, American Institute of Physics, 2010.
40. P. Lhuissier, M. Scheel, L. Salvo, E. Boller, M. D. Michiel and J. J. Blandin: '4D damage characterization during superplastic deformation of magnesium alloys', *Mat. Sci. Forum*, 2012, **735**, 61–66.
41. A. P. Merkle and J. Gelb: 'The ascent Of 3D microscopy in the laboratory', *Microsc. Today*, 2013, **21**, (1), 10–15.
42. K. Uesugi, M. Hoshino, A. Takeuchi, Y. Suzuki and N. Yagi: 'Development of fast and high throughput tomography using CMOS image detector at SPRing-8', Developments in X-Ray Tomography VIII, *Proc.SPIE*, 2012, **8506**, 850601.
43. P. J. Withers and F. De Carlo: 'Table of CT Imaging Times', 2013; Available from: https://docs.google.com/spreadsheets/ccc?key=0Ar8bW1AwveL_dHDa2VjYndRVl9ybnRkPckRrZUQ1alE.
44. D. S. Eastwood, V. Yufit, J. Gelb, A. Gu, R. S. Bradley, S. J. Harris, D. J. L. Brett, N. P. Brandon, P. D. Lee, P. J. Withers and P. Shearing: 'Lithiation induced dilation mapping in a Li-ion battery electrode by 3D X-ray microscopy and digital volume correlation', *Advanced Energy Materials*, 2013, in press.
45. T. Lowe, R. J. Garwood, T. J. Simonsen, R. S. Bradley and P. J. Withers: 'Metamorphosis revealed: time-lapse three-dimensional imaging inside a living chrysalis', *J.R. Soc. Interface*, 2013, **10**, (84), 20130304. doi:10.1098/rsif.2013.0304.
46. D. Weiss, A. Deffner and C. Kuhn: 'Einfluss der Quellung auf Reproduzierbarkeit und Antastabweichung im Röntgen-Computertomographen', Proc. Fachtagung Industrielle Computertomographie, 2010, Wels. Available online at NDT Database, <http://www.ndt.net/article/ctc2010/papers/227.pdf>.
47. J. Steffen and T. Fröba: 'Reducing the focal spot shift of microfocus X-ray tubes to increase the accuracy of CT-based dimensional measurement', International Symposium on Digital Industrial Radiology and Computed Tomography, 2011, Berlin, Germany.
48. P. Rockett: 'The development of a laboratory X-ray microtomography system for the study of soft-solids and cellular materials', PhD thesis, Oxford University, Oxford, 2008.
49. A. Pyzalla, B. Camin, T. Buslaps, M. Di Michiel, H. Kaminski, A. Kottar, A. Pernack and W. Reimers: 'Simultaneous tomography and diffraction analysis of creep damage', *Science*, 2005, **308**, (5718), 92–95.
50. A. Vagnon, O. Lame, D. Bouvard, M. Di Michiel, D. Bellet and G. Kapelski: 'Deformation of steel powder compacts during sintering: correlation between macroscopic measurement and *in situ* microtomography analysis', *Acta Mater.*, 2006, **54**, (2), 513–522.
51. E. Maire, V. Carmona, J. Courbon and W. Ludwig: 'Fast X-ray tomography and acoustic emission study of damage in metals during continuous tensile tests', *Acta Mater.*, 2007, **55**, (20), 6806–6815.

52. M. Suery, J. Adrien, C. Landron, S. Terzi, E. Maire, L. Salvo and J. J. Blandin: 'Fast *in situ* X-ray micro tomography characterisation of microstructural evolution and strain-induced damage in alloys at various temperatures', *Int. J. Mater. Res.*, 2010, **101**, (9), 1080–1088.
53. N. Limodin, L. Salvo, E. Boller, M. Suery, M. Felberbaum, S. Gaillieue and K. Madi: '*In situ* and real-time 3-D micro-tomography investigation of dendritic solidification in an Al-10 wt.% Cu alloy', *Acta Mater.*, 2009, **57**, (7), 2300–2310.
54. M. Suery, S. Terzi, B. Mireux, L. Salvo, J. Adrien and E. Maire: 'Fast *In Situ* X-ray microtomography observations of solidification and semisolid deformation of Al-Cu alloys', *JOM*, 2012, **64**, (1), 83–88.
55. C. Puncreobutr, P. D. Lee, R. W. Hamilton and A. B. Phillion: 'Quantitative 3D characterization of solidification structure and defect evolution in Al alloys', *JOM*, 2012, **64**, (1), 89–95.
56. S. Terzi, L. Salvo, M. Suery, N. Limodin, J. Adrien, E. Maire, Y. Pannier, M. Bornert, D. Bernard, M. Felberbaum, M. Rappaz and E. Bollerr: '*In situ* X-ray tomography observation of inhomogeneous deformation in semi-solid aluminium alloys', *Scr. Mater.*, 2009, **61**, (5), 449–452.
57. S. Deville, J. Adrien, E. Maire, M. Scheel and M. Di. Michiel: 'Time-lapse, three-dimensional *in situ* imaging of ice crystal growth in a colloidal silica suspension', *Acta Mater.*, 2013, **61**, (6), 2077–2086.
58. W. L. Li, K. Lu and J. Y. Walz: 'Freeze casting of porous materials: review of critical factors in microstructure evolution', *Int. Mater. Rev.*, 2012, **57**, (1), 37–60.
59. S. Zabler, C. Fella, A. Dietrich, F. Nachtrab, M. Salamon, V. Volland, T. Ebensperger, S. Oeckl, R. Hanke and N. Uhlmann: 'High-resolution and high-speed CT in industry and research', 2012, **8506**, 850617, doi:10.1117/12.964588 2012, 850617–850617.
60. U. Hampel, M. Speck, D. Koch, H. J. Menz, H. G. Mayer, J. Fietz, D. Hoppe, E. Schleicher, C. Zippe and H. M. Prasser: 'Experimental ultra fast X-ray computed tomography with a linearly scanned electron beam source', *Flow Meas. Instrum.*, 2005, **16**, (2–3), 65–72.
61. H. M. Prasser, M. Misawa and I. Tisceanu: 'Comparison between wire-mesh sensor and ultra-fast X-ray tomograph for an air-water flow in a vertical pipe', *Flow Meas. Instrum.*, 2005, **16**, (2–3), 73–83.
62. T. Sturzel, M. Bieberle, E. Laurien, U. Hampel, F. Barthel, H. J. Menz and H. G. Mayer: 'Experimental facility for two-and three-dimensional ultrafast electron beam X-ray computed tomography', *Rev. Sci. Instr.*, 2011, **82**, (2), 7.
63. K. Hori, T. Fujimoto and K. Kawanishi: 'Development of ultrafast X-ray computed tomography scanner system', *IEEE Trans. Nucl. Sci.*, 1998, **45**, (4), 2089–2094.
64. W. Thompson, W. R. B. Lionheart and Morton, E. J.: 'X-ray imaging apparatus of fast cone-beam computed tomography X-ray scanning system, has controller to cause emission of X-rays from source in accordance with firing pattern that causes even distribution of X-rays over virtual cylinder X-ray tomography inspection systems', patent number US7876879(B2).
65. Z. Zhang, M. Bieberle, F. Barthel, L. Szalinski, and U. Hampel: 'Investigation of upward cocurrent gas-liquid pipe flow using ultrafast X-ray tomography and wire-mesh sensor', *Flow Measurement and Instrumentation*, 2013, **32**, 111–118.
66. P. J. Withers: 'X-ray nanotomography', *Mater. Today*, 2007, **10**, (12), 23–34.
67. W. S. Haddad, I. McNulty, J. E. Trebes, E. H. Anderson, R. A. Levesque and L. Yang: 'Ultra-high-resolution X-ray tomography', *Science*, 1994, **266**, (5188), 1213–1215.
68. H. Toda, K. Uesugi, A. Takeuchi, K. Minami, M. Kobayashi and T. Kobayashi: 'Three-dimensional observation of nanoscopic precipitates in an aluminum alloy by microtomography with Fresnel zone plate optics', *Appl. Phys. Lett.*, 2006, **89**, 143112.
69. W. Chao, B. D. Harteneck, J. A. Liddle, E. H. Anderson and D. T. Attwood: 'Soft X-ray microscopy at a spatial resolution better than 15nm', *Nature*, 2005, **435**, 1210–1213.
70. G. C. Yin, M. T. Tang, Y. F. Song, F. R. Chen, K. S. Liang, F. W. Duerwer, W. B. Yun, C. H. Ko and H. P. D. Shieh: 'Energy-tunable transmission X-ray microscope for differential contrast imaging with near 60 nm resolution tomography', *Appl. Phys. Lett.*, 2006, **88**, (24), 241115.
71. R. P. Winarski, M. V. Holt, V. Rose, P. Fuesz, D. Carbaugh, C. Benson, D. Shu, D. Kline, G. B. Stephenson, I. McNulty and J. Maser: 'A hard X-ray nanoprobe beamline for nanoscale microscopy', *J. Synchrotron Radiat.*, 2012, **19**, (6), 1056–1060.
72. I. Snigireva, A. Snigirev, V. Kohn, V. Yunkin, M. Grigoriev, S. Kuznetsov, G. Vaughan and M. Di Michiel: 'Focusing high energy X-rays with stacked Fresnel zone plates', *Phys. Status Solidi A*, 2007, **204**, (8), 2817–2823.
73. A. Tkachuk, M. Feser, H. Cui, F. Duerwer, H. Chang and W. Yun: 'High-resolution X-ray tomography using laboratory sources', Developments in X-ray Tomography V, *Proc. SPIE*, 2006, **6318**, 63181D, doi: 10.1117/12.682383.
74. W. B. Yun, M. Feser, A. Lyon, F. W. Duerwer and Y. X. Wang: 'Pathways to sub-10 nm X-ray imaging using zone plate lens', Design and Microfabrication of Novel X-Ray Optics II, *Proc. SPIE*, 2004, 5539, 133–137.
75. R. Mokso, P. Cloetens, E. Maire, W. Ludwig and J. Y. Buffiere: 'Nanoscale zoom tomography with hard x rays using Kirkpatrick-Baez optics', *Appl. Phys. Lett.*, 2007, **90**, (14), 144104.
76. C. Rau, V. Crecea, C. P. Richter, K. M. Peterson, P. R. Jemian, U. Neuhaeusler, G. Schneider, X. Yu, P. V. Braun, T. C. Chiang and I. K. Robinson: 'A hard X-ray KB-FZP microscope for tomography with sub-100-nm resolution - art. no. 63181G', Developments in X-Ray Tomography V, *Proc. SPIE*, 2006, **6318**, 63181G, doi:10.1117/12.680975.
77. G. Requena, P. Cloetens, W. Altendorfer, C. Poletti, D. Tolnai, F. Warchomicka and H. P. Degischer: 'Sub-micrometer synchrotron tomography of multiphase metals using Kirkpatrick-Baez optics', *Scr. Mater.*, 2009, **61**, (7), 760–763.
78. H. R. F. Horn and H. G. Waltinger: 'How to obtain and use X-ray projection microscopy in the SEM', *Scanning*, 1978, **1**, 100–108.
79. S. C. Mayo, P. R. Miller, S. W. Wilkins, T. J. Davis, D. Gao, T. E. Gureyev, D. Paganin, D. J. Parry, A. Pogany and A. W. Stevenson: 'Quantitative X-ray projection microscopy: phase-contrast and multi-spectral imaging', *J. Microsc.*, 2002, **207**, 79–96.
80. S. C. Mayo, P. R. Miller, J. Sheffield-Parker, T. Gureyev and S. W. Wilkins: 'Attainment of <60nm Resolution in Phase-Contrast X-ray Microscopy using an add-on to an SEM', *Proc. 8th Int. Conf. X-ray Microscopy IPAP Conf. Series 7*, Himeji, Japan, 26–30 July, 343–345, 2005. Tokyo, Japan, IPAP, 2005.
81. T. L. Burnett, M. Curioni, T. Hashimoto, S. A. McDonald, G. E. Thompson, P. J. Withers, R. Guerts, M. Janus and C. V. Vilsteren: 'Correlative Tomography', in press, 2013.
82. S. Aoki and S. Kikuta: 'X-ray holographic microscopy', *Jpn. J. Appl. Phys.*, 1974, **13**, (9), 1385–1392.
83. B. Niemann, D. Rudolph and G. Schmahl: 'X-ray microscopy with synchrotron radiation', *Appl. Opt.*, 1976, **15**, (8), 1883–1884.
84. B. Niemann, D. Rudolph and G. Schmahl: 'The Gottingen X-ray microscopes', *Nucl. Instr. Meth. Phys. Res.*, 1983, **208**, (1–3), 367–371.
85. C. Jacobsen, S. Williams, E. Anderson, M. T. Browne, C. J. Buckley, D. Kern, J. Kirz, M. Rivers and X. Zhang: 'Diffraction-limited imaging in a scanning electron microscope', *Opt Commun.*, 1991, **86**, (3–4), 351–364.
86. G. Schneider, T. Schliebe and H. Aschoff: 'Cross-linked polymers for nanofabrication of high-resolution zone plates in nickel and germanium', *J. Vac. Sci. Technol. B*, 1995, **13**, (6), 2809–2812.
87. W. L. Chao, E. Anderson, G. P. Denbeaux, B. Harteneck, J. A. Liddle, D. L. Olynick, A. L. Pearson, F. Salmassi, C. Y. Song and D. T. Attwood: 'Soft 20-nm resolution X-ray microscopy demonstrated by use of multilayer test structures', *Opt. Lett.*, 2003, **28**, (21), 2019–2021.
88. W. Chao, P. Fischer, T. Tyliczszak, S. Rekowa, E. Anderson and P. Naulleau: 'Real space soft X-ray imaging at 10 nm spatial resolution', *Opt. Express*, 2012, **20**, (9), 9777–9783.
89. W. B. Yun, P. J. Viccaro, B. Lai and J. Chrzas: 'Coherent hard X-ray focusing optics and applications', *Rev. Sci. Instrum.*, 1992, **63**, (1), 582–585.
90. B. Lai, W. Yun, Y. Xiao, L. Yang, D. Legnini, Z. Cai, A. Krasnoperova, F. Cerrina, E. Difabrizio, L. Grella and M. Gentili: 'Development of a hard X-ray microscope', *Rev. Sci. Instrum.*, 1995, **66**, (2), 2287–2289.
91. B. Kaulich, S. Oestreich, M. Salome, R. Barrett, J. Susini, T. Wilhein, E. Di Fabrizio, M. Gentili and P. Charalambous: 'Feasibility of transmission X-ray microscopy at 4 keV with spatial resolutions below 150 nm', *Appl. Phys. Lett.*, 1999, **75**, (26), 4061–4063.
92. C. David, B. Kaulich, R. Barrett, M. Salome and J. Susini: 'High-resolution lenses for sub-100 nm X-ray fluorescence microscopy', *Appl. Phys. Lett.*, 2000, **77**, (23), 3851–3853.
93. Y. Feng, M. Feser, A. Lyon, S. Rishton, X. Zeng, S. Chen, S. Sassolini and W. Yun: 'Nanofabrication of high aspect ratio 24

- nm X-ray zone plates for X-ray imaging applications', *J. Vac. Sci. Technol. B*, 2007, **25**, (6), 2004–2007.
94. J. Vila-Comamala, Y. S. Pan, J. J. Lombardo, W. M. Harris, W. K. S. Chiu, C. David and Y. X. Wang: 'Zone-doubled Fresnel zone plates for high-resolution hard X-ray full-field transmission microscopy', *J. Synchrotron Radiat.*, 2012, **19**, 705–709.
 95. W. J. Liu, G. E. Ice, J. Z. Tischler, A. Khounsary, C. Liu, L. Assoufid and A. T. Macrander: 'Short focal length Kirkpatrick-Baez mirrors for a hard X-ray nanoprobe', *Rev. Sci. Instrum.*, 2005, **76**, (11), 10310–19.
 96. S. Matsuyama, N. Kidani, H. Mimura, Y. Sano, Y. Kohmura, K. Tamasaku, M. Yabashi, T. Ishikawa and K. Yamauchi: 'Hard-X-ray imaging optics based on four aspherical mirrors with 50 nm resolution', *Opt. Express*, 2012, **20**, (9), 10310–19.
 97. A. Snigirev, I. Snigireva, M. Grigoriev, V. Yunkin, M. Di Michiel, G. Vaughan, V. Kohn and S. Kuznetsov: 'High energy X-ray nanofocusing by silicon planar lenses', in '9th International Conference on X-Ray Microscopy', (eds. C. David, *et al.*), 2009, Bristol, Iop Publishing Ltd.
 98. J. Kirz and C. Jacobsen: 'The history and future of X-ray microscopy', in '9th International Conference on X-Ray Microscopy', (eds. C. David, *et al.*), 2009.
 99. K. Dzieciol, A. Borbély, F. Sket, A. Isaac, M. Di Michiel, P. Cloetens, T. Buslaps and A. R. Pyzalla: 'Void growth in copper during high-temperature power-law creep', *Acta Mater.*, 2011, **59**, (2), 671–677.
 100. H. Ostadi, P. Rama, Y. Liu, R. Chen, X. X. Zhang and K. Jiang: 'Threshold fine-tuning and 3D characterisation of porous media using X-ray nanotomography', *Curr. Nanosci.*, 2010, **6**, (2), 226–231.
 101. P. Trtik, M. Soos, B. Munch, A. Lamprou, R. Mokso and M. Stampanoni: 'Quantification of a single aggregate inner porosity and pore accessibility using hard X-ray phase-contrast nanotomography', *Langmuir*, 2011, **27**, (21), 12788–12791.
 102. Z. Asghar, G. Requena, H. P. Degischer and P. Cloetens: 'Three-dimensional study of Ni aluminides in an AlSi12 alloy by means of light optical and synchrotron microtomography', *Acta Mater.*, 2009, **57**, (14), 4125–4132.
 103. P. Wright, X. Fu, I. Sinclair and S. M. Spearing: 'Ultra high resolution computed tomography of damage in notched carbon fiber-epoxy composites', *J. Compos. Mater.*, 2008, **42**, (19), 1993–2002.
 104. W. K. Epting, J. Gelb and S. Litster: 'Resolving the three-dimensional microstructure of polymer electrolyte fuel cell electrodes using nanometer-scale X-ray computed tomography', *Adv. Funct. Mater.*, 2012, **22**, (3), 555–560.
 105. Y. Guan, Y. H. Gong, W. J. Li, J. Gelb, L. Zhang, G. Liu, X. B. Zhang, X. X. Song, C. R. Xia, Y. Xiong, H. Q. Wang, Z. Y. Wu and Y. C. Tian: 'Quantitative analysis of micro structural and conductivity evolution of Ni-YSZ anodes during thermal cycling based on nano-computed tomography', *J. Power Sources*, 2011, **196**, (24), 10601–10605.
 106. Y. Guan, W. J. Li, Y. H. Gong, G. Liu, X. B. Zhang, J. Chen, J. Gelb, W. B. Yun, Y. Xiong, Y. C. Tian and H. Q. Wang: 'Analysis of the three-dimensional microstructure of a solid-oxide fuel cell anode using nano X-ray tomography', *J. Power Sources*, 2011, **196**, (4), 1915–1919.
 107. P. R. Shearing, R. S. Bradley, J. Gelb, S. N. Lee, A. Atkinson, P. J. Withers and N. P. Brandon: 'Using synchrotron X-ray nano-CT to characterize SOFC electrode microstructures in three-dimensions at operating temperature', *Electrochem. Solid-State Lett.*, 2011, **14**, (10), B117–B120.
 108. P. R. Shearing, R. S. Bradley, J. Gelb, F. Tariq, P. J. Withers and N. P. Brandon: 'Exploring microstructural changes associated with oxidation in Ni-YSZ SOFC electrodes using high resolution X-ray computed tomography', *Solid State Ionics*, 2012, **216**, 69–72.
 109. C. Landron, E. Maire, J. Adrien, H. Suhonen, P. Cloetens and O. Bouaziz: 'Non-destructive 3-D reconstruction of the martensitic phase in a dual-phase steel using synchrotron holotomography', *Scripta Mater.*, 2012, **66**, (12), 1077–1080.
 110. H. Toda, K. Minami, M. Kobayashi, K. Uesugi, A. Takeuchi and T. Kobayashi: 'Observation of precipitates in aluminum alloys by sub-micrometer resolution tomography using Fresnel zone plate', *Aluminum alloys 2006*, Pts 1 and 2: research through innovation and technology, *Mater. Sci. Forum*, 2006, **519–521**, 1361–1366.
 111. S. D. Mookhoek, S. C. Mayo, A. E. Hughes, S. A. Furman, H. R. Fischer and S. van der Zwaag: 'Applying SEM-based X-ray microtomography to observe self-healing in solvent encapsulated thermoplastic materials', *Adv. Eng. Mater.*, 2010, **12**, (3), 228–234.
 112. P. J. Withers, G. E. Thompson, A. Gholinia, T. Hashimoto, X. R. Zhou, U. Bangert and S. Haigh: '3-D Materials Characterization over a range of time and length scales', *Adv. Mater. Processes*, 2012, **170**, (6), 28–32.
 113. H. F. Poulsen, S. F. Nielsen, E. M. Lauridsen, S. Schmidt, R. M. Suter, U. Lienert, L. Margulies, T. Lorentzen and D. J. Jensen: 'Three-dimensional maps of grain boundaries and the stress state of individual grains in polycrystals and powders', *J. Appl. Crystallogr.*, 2001, **34**, 751–756.
 114. B. C. Larson, W. Yang, G. E. Ice, J. D. Budai and J. Z. Tischler: 'Three-dimensional X-ray structural microscopy with submicrometre resolution', *Nature*, 2002, **415**, 887–890.
 115. X. Fu, H. F. Poulsen, S. Schmidt, S. F. Nielsen, E. M. Lauridsen and D. J. Jensen: 'Non-destructive mapping of grains in three dimensions', *Scripta Mater.*, 2003, **49**, (11), 1093–1096.
 116. K. Hannesson and D. J. Jensen: 'Three dimensional characterization of grain structures by EBSD and 3DXRD', *Materials Science Forum*, 2007, **558–559**, 751–756.
 117. E. Knudsen: '3D grainmap generation with the algebraic reconstruction technique from 3DXRD data', *Mater. Sci. Technol.*, 2005, **21**, (12), 1376–1378.
 118. B. C. Larson, W. Yang, J. Z. Tischler, G. E. Ice, J. D. Budai, W. Liu and H. Weiland: 'Micron-resolution 3-D measurement of local orientations near a grain-boundary in plane-strained aluminum using X-ray microbeams', *Int. J. Plast.*, 2004, **20**, (3), 543–560.
 119. H. F. Poulsen, E. M. Lauridsen, S. Schmidt, L. Margulies and J. H. Driver: '3D-characterisation of microstructure evolution during annealing of a deformed aluminum single crystal', *Acta Mater.*, 2003, **51**, (9), 2517–2529.
 120. N. Iqbal, N. H. van Dijk, S. E. Offerman, M. P. Moret, L. Katgerman and G. J. Kearley: 'Real-time observation of grain nucleation and growth during solidification of aluminium alloys', *Acta Mater.*, 2005, **53**, (10), 2875–2880.
 121. C. Gundlach, W. Pantleon, E. M. Lauridsen, L. Margulies, R. D. Doherty and H. F. Poulsen: 'Direct observation of subgrain evolution during recovery of cold-rolled aluminium', *Scripta Mater.*, 2004, **50**, (4), 477–481.
 122. E. M. Lauridsen, D. J. Jensen, H. F. Poulsen and U. Lienert: 'Kinetics of individual grains during recrystallization', *Scripta Mater.*, 2000, **43**, (6), 561–566.
 123. E. M. Lauridsen, H. F. Poulsen, S. F. Nielsen and D. J. Jensen: 'Recrystallization kinetics of individual bulk grains in 90% cold-rolled aluminium', *Acta Mater.*, 2003, **51**, (15), 4423–4435.
 124. S. S. West, G. Winther, L. Margulies, E. Knudsen, H. O. Sorensen, S. Schmidt and D. J. Jensen: 'Mapping partially recrystallised structures by 3DXRD', *Materials Science Forum*, 2007, **558–559**, 389–394.
 125. S. S. West, S. Schmidt, H. O. Sorensen, G. Winther, H. F. Poulsen, L. Margulies, C. Gundlach and D. J. Jensen: 'Direct non-destructive observation of bulk nucleation in 30% deformed aluminum', *Scripta Mater.*, 2009, **61**, (9), 875–878.
 126. G. Winther, L. Margulies, S. Schmidt and H. F. Poulsen: 'Lattice rotations of individual bulk grains Part II: correlation with initial orientation and model comparison', *Acta Mater.*, 2004, **52**, (10), 2863–2872.
 127. S. E. Offerman, N. H. van Dijk, J. Sietsma, E. M. Lauridsen, L. Margulies, S. Grigull, H. F. Poulsen and S. van der Zwaag: 'Phase transformations in steel studied by 3DXRD microscopy', *Nucl. Instrum. Methods Phys. Res. B*, 2006, **246**, (1), 194–200.
 128. V. I. Savran, S. E. Offerman, N. H. van Dijk, E. M. Lauridsen, L. Margulies and J. Sietsma: 'Growth of individual austenite grains measured with 3DXRD microscopy', *Materials Science Forum*, 2007, **561–565**, 2301–2304.
 129. S. Schmidt, U. L. Olsen, H. F. Poulsen, H. O. Sorensen, E. M. Lauridsen, L. Margulies, C. Maurice and D. J. Jensen: 'Direct observation of 3-D grain growth in Al-0.1% Mn', *Scripta Mater.*, 2008, **59**, (5), 491–494.
 130. Z.-G. Yang and M. Enomoto: 'Discussion on the nucleation rate of ferrite during continuous cooling in a lowcarbon steel measured by 3DXRD', in 'Solid-Solid Phase Transformations in Inorganic Materials '05', edited by Howe *et al.*, 2005, Warrendale, PA, TMS. Pages 47–52.
 131. A. W. Larsen, H. F. Poulsen, L. Margulies, C. Gundlach, Q. F. Xing, X. X. Huang and D. J. Jensen: 'Nucleation of recrystallization observed *in situ* in the bulk of a deformed metal', *Scripta Mater.*, 2005, **53**, (5), 553–557.
 132. S. Schmidt, S. F. Nielsen, C. Gundlach, L. Margulies, X. Huang and D. J. Jensen: 'Watching the Growth of Bulk Grains During

- Recrystallization of Deformed Metals,' *Science*, 2004, **305**, (5681), 229–232.
133. C. C. Aydiner, J. V. Bernier, B. Clausen, U. Lienert, C. N. Tome and D. W. Brown: 'Evolution of stress in individual grains and twins in a magnesium alloy aggregate', *Phys. Rev. B*, 2009, **80**, (2), 024113.
 134. U. Lienert, M. C. Brandes, J. V. Bernier, J. Weiss, S. D. Shastri, M. J. Mills and M. P. Miller: 'In situ single-grain peak profile measurements on Ti-7Al during tensile deformation', *Mater. Sci. Eng. A*, 2009, **524**, (1–2), 46–54.
 135. J. V. Bernier, N. R. Barton, U. Lienert and M. P. Miller: 'Far-field high-energy diffraction microscopy: a tool for intergranular orientation and strain analysis', *J. Strain Anal. Eng. Des.*, 2011, **46**, (7), 527–547.
 136. J. Oddershede, S. Schmidt, H. F. Poulsen, L. Margulies, J. P. Wright, M. Moscicki and W. Reimers: 'Measuring the elastic strain of individual grains in a polycrystalline material - extending a micro-scale technique to the nano-regime', in 'Nanostructured Metals: Fundamentals to Applications: Proceedings of the 30th Risø International Symposium on Materials Science', 2009, Roskilde, Denmark, Risoe National Laboratory for Sustainable Energy, Technical University of Denmark. Pages 277–283.
 137. J. Oddershede, S. Schmidt, H. F. Poulsen and W. Reimers: 'Measuring type II stresses using 3DXRD', *Materials Science Forum*, 2010, **652**, 63–69.
 138. J. Oddershede, S. Schmidt, H. F. Poulsen, H. O. Sorensen, J. Wright and W. Reimers: 'Determining grain resolved stresses in polycrystalline materials using three-dimensional X-ray diffraction', *J. Appl. Crystallogr.*, 2010, **43**, 539–549.
 139. J. Oddershede, S. Schmidt, H. F. Poulsen, L. Margulies, J. Wright, M. Moscicki, W. Reimers and G. Winther: 'Grain-resolved elastic strains in deformed copper measured by three-dimensional X-ray diffraction', *Mater. Charact.*, 2011, **62**, (7), 651–660.
 140. U. Lienert, S. F. Li, C. M. Hefferan, J. Lind, R. M. Suter, J. V. Bernier, N. R. Barton, M. C. Brandes, M. J. Mills, M. P. Miller, B. Jakobsen and W. Pantleon: 'High-energy diffraction microscopy at the advanced photon source', *JOM*, 2011, **63**, (7), 70–77.
 141. C. M. Hefferan, S. F. Li, J. Lind, U. Lienert, A. D. Rollett, P. Wynblatt and R. M. Suter: 'Statistics of High Purity Nickel Microstructure From High Energy X-ray Diffraction Microscopy', *CMC Comput. Mater. Continua*, 2009, **14**, (3), 209–219.
 142. C. M. Hefferan, S. F. Li, J. Lind and R. M. Suter: 'Tests of microstructure reconstruction by forward modeling of high energy X-ray diffraction microscopy data', *Powder Diffr.*, 2010, **25**, (2), 132–137.
 143. R. M. Suter, D. Hennessy, C. Xiao and U. Lienert: 'Forward modeling method for microstructure reconstruction using X-ray diffraction microscopy: Single-crystal verification', *Rev. Sci. Instrum.*, 2006, **77**, (12), 123905-1-123905-12.
 144. R. M. Suter, C. M. Hefferan, S. F. Li, D. Hennessy, C. Xiao, U. Lienert and B. Tieman: 'Probing microstructure dynamics with X-ray diffraction microscopy', *J. Eng. Mater.-T. ASME*, 2008, **130**, (2), 021007-1-021007-5.
 145. R. I. Barabash, H. Bei, G. E. Ice, Y. F. Gao and O. M. Barabash: '3-D X-ray strain microscopy in two-phase composites at submicron length scales', *J. Met.*, 2011, **63**, (3), 30–34.
 146. C. M. Hefferan, J. Lind, S. F. Li, U. Lienert, A. D. Rollett and R. M. Suter: 'Observation of recovery and recrystallization in high-purity aluminum measured with forward modeling analysis of high-energy diffraction microscopy', *Acta Mater.*, 2012, **60**, (10), 4311–4318.
 147. G. Johnson, A. King, M. G. Honnicke, J. Marrow and W. Ludwig: 'X-ray diffraction contrast tomography: a novel technique for three-dimensional grain mapping of polycrystals. II. The combined case', *J. Appl. Crystallogr.*, 2008, **41**, 310–318.
 148. W. Ludwig, S. Schmidt, E. M. Lauridsen and H. F. Poulsen: 'X-ray diffraction contrast tomography: a novel technique for three-dimensional grain mapping of polycrystals. I. Direct beam case', *J. Appl. Crystallogr.*, 2008, **41**, 302–309.
 149. W. Ludwig, P. Reischig, A. King, M. Herbig, E. M. Lauridsen, G. Johnson, T. J. Marrow and J. Y. Buffiere: 'Three-dimensional grain mapping by X-ray diffraction contrast tomography and the use of Friedel pairs in diffraction data analysis', *Rev. Sci. Instrum.*, 2009, **80**, (3), 033905.
 150. W. Ludwig, A. King, M. Herbig, P. Reischig, J. Marrow, L. Babout, E. M. Lauridsen, H. Proudhon and J. Y. Buffiere: 'Characterization of Polycrystalline Materials Using Synchrotron X-ray Imaging and Diffraction Techniques', *JOM*, 2010, **62**, (12), 22–28.
 151. M. Syha, W. Rheinheimer, M. Baeurer, E. M. Lauridsen, W. Ludwig, D. Weygand and P. Gumbsch: 'Three-dimensional grain structure of sintered bulk strontium titanate from X-ray diffraction contrast tomography', *Scripta Mater.*, 2012, **66**, (1), 1–4.
 152. A. King, G. Johnson, D. Engelberg, W. Ludwig and J. Marrow: 'Observations of intergranular stress corrosion cracking in a grain-mapped polycrystal', *Science*, 2008, **321**, (5887), 382–385.
 153. S. R. du Roscoat, A. King, A. Philip, P. Reischig, W. Ludwig, F. Flin and J. Meyssonier: 'Analysis of snow microstructure by means of X-ray diffraction contrast tomography', *Adv. Eng. Mater.*, 2011, **13**, (3), 128–135.
 154. D. Gonzalez, A. King, I. Simonovski, J. Quinta da Fonseca and P. J. Withers: 'Modelling & measurement of plastic deformation & grain rotation in 3D at the grain to grain level', 2013, in press.
 155. M. Herbig, A. King, P. Reischig, H. Proudhon, E. M. Lauridsen, J. Marrow, J.-Y. Buffiere and W. Ludwig: '3-D growth of a short fatigue crack within a polycrystalline microstructure studied using combined diffraction and phase-contrast X-ray tomography', *Acta Mater.*, 2011, **59**, (2), 590–601.
 156. F. Hofmann, B. Abbey, L. Connor, N. Baimpas, X. Song, S. Keegan and A. M. Korsunsky: 'Imaging of grain-level orientation and strain in thicker metallic polycrystals by high energy transmission micro-beam Laue (HETL) diffraction techniques', *Int. J. Mater. Res.*, 2012, **103**, (2), 192–199.
 157. A. C. Kak and M. Slaney: 'Principles of computerised tomographic imaging'; 1987, IEEE Press. New York.
 158. L. A. Feldkamp, L. C. Davis and J. W. Kress: 'Practical cone-beam algorithm', *J. Opt. Soc. Am. A Opt. Image Sci. Vis.*, 1984, **1**, (6), 612–619.
 159. H. K. Tuy: 'An inversion-formula for cone-beam reconstruction', *Siam J. Appl. Math.*, 1983, **43**, (3), 546–552.
 160. G. Davis, A. Evershed, J. Elliott and D. Mills: 'Quantitative X-ray microtomography with a conventional source', *Proc. SPIE*, 2010, **7804**, 78040I-78040I.
 161. S. Titarenko, V. Titarenko, A. Kyrieleis and P. J. Withers: 'A priori information in a regularized sinogram-based method for removing ring artefacts in tomography', *J. Synchrotron Rad.*, 2010, **17**, 540–549.
 162. R. A. Brooks and G. Dichiro: 'Beam hardening in X-ray reconstructive tomography', *Phys. Med. Biol.*, 1976, **21**, (3), 390–398.
 163. G. Van Gompel: 'Towards accurate image reconstruction from truncated X-ray CT projections', PhD thesis, Antwerp University, 2009. Antwerp.
 164. G. T. Herman and A. Kuba, (eds). *Advances in discrete tomography and its applications*, 392; 2007, Birkhäuser, Basel.
 165. K. J. Batenburg and J. Sijbers: 'DART: A Practical Reconstruction Algorithm for Discrete Tomography', *IEEE Trans. Image Process.*, 2011, **20**, (9), 2542–2553.
 166. G. H. Chen, J. Tang and S. H. Leng: 'Prior image constrained compressed sensing (PICCS): A method to accurately reconstruct dynamic CT images from highly undersampled projection data sets', *Med. Phys.*, 2008, **35**, (2), 660–663.
 167. A. K. Hara, R. G. Paden, A. C. Silva, J. L. Kujak, H. J. Lawder and W. Pavlicek: 'Iterative reconstruction technique for reducing body radiation dose at CT: feasibility study', *Am. J. Roentgenol.*, 2009, **193**, (3), 764–771.
 168. E. Y. Sidky, C. M. Kao and X. H. Pan: 'Accurate image reconstruction from few-views and limited-angle data in divergent-beam CT', *J. Xray Sci. Technol.*, 2006, **14**, (2), 119–139.
 169. D. Kazantsev, W. M. Thompson, K. J. Dobson, A. P. Kaestner, W. R. B. Lionheart, P. J. Withers, and P. D. Lee: 'Simultaneous 4D-CT reconstruction using higher order spatial regularization and global Gibbs-type temporal prior', *Inverse Problems and Imaging Journal*, 2013, (**submitted**).
 170. J. Zhou, A. Bousse, G. Yang and J.-J. Bellanger: 'A blob-based tomographic reconstruction of 3D coronary trees from rotational X-ray angiography', *Medical Imaging 2008: Physics of Medical Imaging*, *Proc. SPIE*, 2008, **6913**, 69132N, doi:10.1117/12.769478.
 171. J. Hsieh, B. Nett, Z. Yu, K. Sauer, J.-B. Thibault and C. A. Bouman: 'Recent advances in CT image reconstruction', *Current Radiology Reports*, 2013, **1**, (1), 39–51.
 172. F. Basile, P. Benito, S. Bugani, W. De Nolf, G. Fornasari, K. Janssens, L. Morselli, E. Scavetta, D. Tonelli and A. Vaccari: 'Combined use of synchrotron-radiation-based imaging techniques for the characterization of structured catalysts', *Adv. Funct. Mater.*, 2010, **20**, (23), 4117–4126.

173. P. Bleuet, A. Simionovici, L. Lemelle, T. Ferroir, P. Cloetens, R. Tucoulou and J. Susini: 'Hard X-rays nanoscale fluorescence imaging of earth and planetary science samples', *Appl. Phys. Lett.*, 2008, **92**, (21), 213111.
174. S. R. Stock, F. de Carlo and J. D. Almer: 'High energy X-ray scattering tomography applied to bone', *J. Struct. Biol.*, 2008, **161**, (2), 144–150.
175. P. Bleuet, E. Welcomme, E. Dooryhee, J. Susini, J. L. Hodeau and P. Walter: 'Probing the structure of heterogeneous diluted materials by diffraction tomography', *Nature Mat.*, 2008, **7**, (6), 468–472.
176. G. Harding, M. Newton and J. Kosanetzky: 'Energy-dispersive X-ray-diffraction tomography', *Phys. Med. Biol.*, 1990, **35**, (1), 33–41.
177. S. D. M. Jacques, M. Di Michiel, A. M. Beale, T. Sochi, M. G. O'Brien, L. Espinosa-Alonso, B. M. Weckhuysen and P. Barnes: 'Dynamic X-ray diffraction computed tomography reveals real-time insight into catalyst active phase evolution', *Angew. Chem. Int. Ed.*, 2011, **50**, (43), 10148–10152.
178. M. Alvarez-Murga, P. Bleuet and J. L. Hodeau: 'Diffraction/scattering computed tomography for three-dimensional characterization of multi-phase crystalline and amorphous materials', *J. Appl. Crystallogr.*, 2012, **45**, 1109–1124.
179. S. R. Stock and J. D. Almer: 'Diffraction microcomputed tomography of an Al-matrix SiC-monofilament composite', *J. Appl. Crystallogr.*, 2012, **45**, 1077–1083.
180. A. M. Korsunsky, W. J. J. Vorster, S. Y. Zhang, D. Dini, D. Latham, M. Golshan, J. Liu, Y. Kyriakoglou and M. J. Walsh: 'The principle of strain reconstruction tomography: Determination of quench strain distribution from diffraction measurements', *Acta Mater.*, 2006, **54**, (8), 2101–2108.
181. P. M. Mummery, B. Derby, P. Anderson, G. R. Davis and J. C. Elliott: 'X-Ray Microtomographic Studies of Metal-Matrix Composites Using Laboratory X-Ray Sources', *J. Microsc.*, 1995, **177**, 399–406.
182. C. Jacobsen, G. Flynn, S. Wirick and C. Zimba, *J. Microsc.*, 2000, **197**, 173–184.
183. B. Ohnesorge, T. Flohr, K. Schwarz, J. P. Heiken and K. T. Bae: 'Efficient correction for CT image artifacts caused by objects extending outside the scan field of view', *Med. Phys.*, 2000, **27**, 39–46.
184. A. Kyrieleis, M. Ibson, V. Titarenko and P. J. Withers: 'Image stitching strategies for tomographic imaging of large objects at high resolution at synchrotron sources', *Nucl. Instr. Meth. Phys. Res. A*, 2009, **607**, 677–684.
185. O. Nalcioglu, Z. H. Cho and R. Y. Lou: 'Limited field of view reconstruction in computerized tomography', *IEEE Trans. Nucl. Sci.*, 1979, **26**, (1), 546–551.
186. A. H. Delaney and Y. Bresler: 'Multiresolution tomographic reconstruction using wavelets', *IEEE Trans. Image Process.*, 1995, **4**, (6), 799–813.
187. F. Rashid Farrokhi, K. J. R. Liu, C. A. Berenstein and D. Walnut: 'Wavelet-based multiresolution local tomography', *IEEE Trans. Image Process.*, 1997, **6**, (10), 1412–1430.
188. X. Xiao, F. De Carlo and S. Stock: 'Practical error estimation in zoom-in and truncated tomography reconstructions', *Rev. Sci. Instrum.*, 2007, **78**, 063705.
189. A. Kyrieleis, V. Titarenko, M. Ibson, T. Connelly and P. J. Withers: 'Region-of-interest tomography using filtered back-projection: assessing the practical limits', *J. Microsc.*, 2011, **241**, 69–82.
190. H. Yu, Q. Xu, X. Mou and G. Wang: 'Recent progress in local reconstruction', Developments in X-ray tomography VII, Proc. SPIE, 2010, 7804, 78040V, doi:10.1117/12.859772.
191. J. Y. Buffiere, E. Maire, J. Adrien, J. P. Masse and E. Boller: 'In Situ experiments with X ray tomography: an attractive tool for experimental mechanics', *Exp. Mech.*, 2010, **50**, (3), 289–305.
192. S. A. McDonald, G. Dedreuil-Monet, Y. T. Yao, A. Alderson and P. J. Withers: 'In situ 3D X-ray microtomography study comparing auxetic and non-auxetic polymeric foams under tension', *Phys. Status Solidi B*, 2011, **248**, (1), 45–51.
193. M. Portmann: 'Laminography of the temporal bone', *Arch. Otolaryngol.*, 1963, **78**, 344–350.
194. T. A. Siewert, M. W. Austin, G. K. Lucey and M. J. Plott: 'Evaluation and qualification standards for an X-ray laminography system', *Mater. Eval.*, 1992, **50**, (9), 1027–1032.
195. K. Wakimoto, J. Blunt, C. Carlos, P. J. M. Monteiro, C. P. Ostertag and R. Albert: 'Digital laminography assessment of the damage in concrete exposed to freezing temperatures', *Cem. Concr. Res.*, 2008, **38**, (10), 1232–1245.
196. P. Krueger, S. Niese, E. Zschech, J. Gelb and M. Feser: 'Improved scanning geometry to collect 3D-geometry data in flat samples', 10th Conf on 'X-ray Microscopy', 258–260; 2011, Chicago. 2010, Melville, NY, American Institute of Physics.
197. T. F. Morgeneyer, L. Helfen, I. Sinclair, H. Proudhon, F. Xu and T. Baumbach: 'Ductile crack initiation and propagation assessed via *in situ* synchrotron radiation-computed laminography', *Scripta Mater.*, 2011, **65**, (11), 1010–1013.
198. D. J. Bull, L. Helfen, I. Sinclair, S. M. Spearing and T. Baumbach: 'A comparison of multi-scale 3D X-ray tomographic inspection techniques for assessing carbon fibre composite impact damage', *Compos. Sci. Technol.*, 2013, **75**, 55–61.
199. Z. Ma, J. Tavares, R. N. Jorge and T. Mascarenhas: 'A review of algorithms for medical image segmentation and their applications to the female pelvic cavity', *Comput. Methods Biomech. Biomed. Eng.*, 2010, **13**, (2), 235–246.
200. J. L. Kuhn, S. A. Goldstein, L. A. Feldkamp, R. W. Goulet and G. Jesion: 'Evaluation of a microcomputed tomography system to study trabecular bone-structure', *J. Orthop. Res.*, 1990, **8**, (6), 833–842.
201. R. C. Roche, R. A. Abel, K. G. Johnson and C. T. Perry: 'Quantification of porosity in *Acropora pulchra* (Brook 1891) using X-ray micro-computed tomography techniques', *J. Exp. Marine. Biol. Ecol.*, 2010, **396**, (1), 1–9.
202. W. S. Rasband. 'ImageJ,'1997–2012; Available from: imagej.nih.gov.
203. S. Carmignato, A. Pierobon, P. Rampazzo, M. Parisatto and E. Savio: 'CT for industrial metrology - accuracy and structural resolution of CT dimensional measurements', Conf Industrial Computed Tomography (ICT), 161–172; 2012, Aachen.
204. F. Leonard, S. B. Brown, P. M. Mummery, M. B. McCarthy and P. J. Withers: 'Accuracy and repeatability of X-ray computed tomography measurements', Sub Measurement Sci. Tech., 2013.
205. J. Y. Buffiere, E. Maire, P. Cloetens, G. Lormand and R. Fougères: 'Characterization of internal damage in a MMCp using X-ray synchrotron phase contrast microtomography', *Acta Mater.*, 1999, **47**, (5), 1613–1625.
206. L. Babout, E. Maire and R. Fougères: 'Damage initiation in model metallic materials: X-ray tomography and modelling', *Acta Mater.*, 2004, **52**, 2475–2487.
207. A. Borbely, P. Kenesei and H. Biermann: 'Estimation of the effective properties of particle-reinforced metal-matrix composites from microtomographic reconstructions', *Acta Mater.*, 2006, **54**, (10), 2735–2744.
208. I. G. Watson, M. F. Forster, P. D. Lee, R. J. Dashwood, R. W. Hamilton and A. Chirazi: 'Investigation of the clustering behaviour of titanium diboride particles in aluminium', *Compos. Part A Appl. Sci. Manuf.*, 2005, **36**, (9), 1177–1187.
209. H. Toda, T. Hidaka, M. Kobayashi, K. Uesugi, A. Takeuchi and K. Horikawa: 'Growth behavior of hydrogen micropores in aluminum alloys during high-temperature exposure', *Acta Mater.*, 2009, **57**, (7), 2277–2290.
210. C. Landron, E. Maire, J. Adrien, O. Bouaziz, M. Di Michiel, P. Cloetens and H. Suhonen: 'Resolution effect on the study of ductile damage using synchrotron X-ray tomography', *Nucl. Instrum. Methods Phys. Res. B*, 2012, **284**, 15–18.
211. E. Maire, J. C. Grenier, D. Daniel, A. Baldacci, H. Klocker and A. Bigot: 'Quantitative 3D characterization of intermetallic phases in an Al-Mg industrial alloy by X-ray microtomography', *Scripta Mater.*, 2006, **55**, (2), 123–126.
212. N. Moulin, E. Parra-Denis, D. Jeulin, C. Ducottet, A. Bigot, E. Boller, E. Maire, C. Barat and H. Klocker: 'Constituent Particle Break-Up During Hot Rolling of AA 5182', *Adv. Eng. Mater.*, 2010, **12**, (1–2), 20–29.
213. Z. Asghar, G. Requena and F. Kubel: 'The role of Ni and Fe aluminides on the elevated temperature strength of an AlSi12 alloy', *Mater Sci Eng A Struct Mater*, 2010, **527**, (21–22), 5691–5698.
214. Z. Asghar, G. Requena and E. Boller: 'Three-dimensional rigid multiphase networks providing high-temperature strength to cast AlSi10Cu5Ni1-2 piston alloys', *Acta Mater.*, 2011, **59**, (16), 6420–6432.
215. G. Requena and H. P. Degischer: 'Three-Dimensional Architecture of Engineering Multiphase Metals', *Annual Review of Materials Research*, 2012, **42**, 145–161.
216. J. P. Weiler, J. T. Wood, R. Klassen, E. Maire, R. Berkmortel and G. Wang: 'Relationship between internal porosity and fracture strength of die-cast magnesium AM60B alloy', *Mater. Sci. Eng. A Struct. Mater.*, 2005, **395**, (1–2), 315–322.

217. J. Y. Buffiere, S. Savelli, P. H. Jouneau, E. Maire and R. Fougères: 'Experimental study of porosity and its relation to fatigue mechanisms of model Al-Si7-Mg0.3 cast Al alloys', *Mater. Sci. Eng. A Struct. Mater.*, 2001, **316**, (1–2), 115–126.
218. N. Vanderesse, E. Maire, A. Chabod and J. Y. Buffiere: 'Microtomographic study and finite element analysis of the porosity harmfulness in a cast aluminium alloy', *Int. J. Fatigue*, 2011, **33**, (12), 1514–1525.
219. M. Shirami and G. Harkegard: 'Damage tolerant design of cast components based on defects detected by 3D X-ray computed tomography', *Int. J. Fatigue*, 2012, **41**, 188–198.
220. P. Li, P. D. Lee, D. M. Maijer and T. C. Lindley: 'Quantification of the interaction within defect populations on fatigue behavior in an aluminum alloy', *Acta Mater.*, 2009, **57**, (12), 3539–3548.
221. P. Li, P. D. Lee, T. C. Lindley, D. M. Maijer, G. R. Davis and J. C. Elliott: 'X-ray microtomographic characterisation of porosity and its influence on fatigue crack growth', *Adv. Eng. Mater.*, 2006, **8**, (6), 476–479.
222. N. Vanderesse, E. Maire, M. Darrieulat, F. Montheillet, M. Moreaud and D. Jeulin: 'Three-dimensional microtomographic study of Widmanstätten microstructures in an alpha/beta titanium alloy', *Scripta Mater.*, 2008, **58**, (6), 512–515.
223. L. A. Feldkamp, S. A. Goldstein, A. M. Parfitt, G. Jesion and M. Kleerekoper: 'The direct examination of 3-dimensional bone architecture *in vitro* by computed-tomography', *J. Bone Miner. Res.*, 1989, **4**, (1), 3–11.
224. E. Maire, P. Colombo, J. Adrien, L. Babout and L. Bassetto: 'Characterization of the morphology of cellular ceramics by 3D image processing of X-ray tomography', *J. Eur. Ceram. Soc.*, 2007, **27**, (4), 1973–1981.
225. L. Brabant, J. Vlassenbroeck, Y. De Witte, V. Cnudde, M. N. Boone, J. Dewanckele and L. Van Hoorebeke: 'Three-dimensional analysis of high-resolution X-ray computed tomography data with morpho+', *Microsc. Microanal.*, 2011, **17**, (2), 252–263.
226. D. Bauer, S. Youssef, M. Fleury, S. Bekri, E. Rosenberg and O. Vizika: 'Improving the estimations of petrophysical transport behavior of carbonate rocks using a dual pore network approach combined with computed microtomography', *Transp. Porous Med.*, 2012, **94**, 505–524.
227. J. R. Jones, R. C. Atwood, G. Poologasundarampillai, S. Yue and P. D. Lee: 'Quantifying the 3D macrostructure of tissue scaffolds', *J. Mater. Sci. Mater. Med.*, 2009, **20**, (2), 463–471.
228. W. B. Lindquist, A. Venkatarangan, J. Dunsluir and T. Wong: 'Pore and throat size distributions measured from synchrotron X-ray tomographic images of Fontainebleau sandstones', *J. Geophys. Res.*, 2000, **105**, 21508–21528.
229. A. P. Jivkov, C. Hollis, F. Etiese, S. A. McDonald and P. J. Withers: 'A novel architecture for pore network modelling with applications to permeability of porous media', *J. Hydrology*, 2013, **486**, 246–258.
230. S. Vasic, B. Grobety, J. Kuebler, T. Graule and L. Baumgartner: 'X-ray computed micro tomography as complementary method for the characterization of activated porous ceramic preforms', *J. Mater. Res.*, 2007, **22**, (5), 1414–1424.
231. V. Dattoma, N. I. Giannoccaro, A. Messina and R. Nobile: 'Prediction of residual fatigue life of aluminium foam through natural frequencies and damping shift', *Fatigue Fract. Eng. Mater. Struct.*, 2009, **32**, (7), 601–616.
232. Y. Hangai, Y. Ozeki, S. Kawano, T. Utsunomiya, O. Kuwazuru, M. Hasegawa, S. Koyama and N. Yoshikawa: 'Nondestructive Observation of Pore Structures of A1050 Porous Aluminum Fabricated by Friction Stir Processing', *Mater. Trans.*, 2010, **51**, (3), 548–552.
233. C. Ritzoulis, M. Strobl, C. Panayiotou, G. Choinka, C. Tsiptsias, C. Vasiladou, V. Vasilakos, F. Beckmann, J. Herzen and T. Donath: 'Ultra-small angle neutron scattering and X-ray tomography studies of caseinate-hydroxyapatite microporous materials', *Mater. Chem. Phys.*, 2010, **123**, (1), 77–82.
234. F. Tariq, P. D. Lee, R. Haswell and D. W. McComb: 'The influence of nanoscale microstructural variations on the pellet scale flow properties of hierarchical porous catalytic structures using multiscale 3D imaging', *Chem. Eng. Sci.*, 2011, **66**, (23), 5804–5812.
235. S. Van Bael, G. Kerckhofs, M. Moesen, G. Pyka, J. Schrooten and J. P. Kruth: 'Micro-CT-based improvement of geometrical and mechanical controllability of selective laser melted Ti6Al4V porous structures', *Mater. Sci. Eng. A Struct. Mater.*, 2011, **528**, (24), 7423–7431.
236. J. L. Fife, J. C. Li, D. C. Dunand and P. W. Voorhees: 'Morphological analysis of pores in directionally freeze-cast titanium foams', *J. Mater. Res.*, 2009, **24**, (1), 117–124.
237. B. B. Mandelbrot: 'How long is the coast of Britain? Statistical self-similarity and fractional dimension', *Science*, 1967, **155**, 636–638.
238. P. R. Shearing, N. P. Brandon, J. Gelb, R. Bradley, P. J. Withers, A. J. Marquis, S. Cooper and S. J. Harris: 'Multi length scale microstructural investigations of a commercially available li-ion battery electrode', *J. Electrochem. Soc.*, 2012, **159**, (7), A1023–A1027.
239. J. P. Masse, L. Salvo, D. Rodney, Y. Brechet and O. Bouaziz: 'Influence of relative density on the architecture and mechanical behaviour of a steel metallic wool', *Scripta Mater.*, 2006, **54**, (7), 1379–1383.
240. D. Tsarouchas and A. E. Markaki: 'Extraction of fibre network architecture by X-ray tomography and prediction of elastic properties using an affine analytical model', *Acta Mater.*, 2011, **59**, (18), 6989–7002.
241. R. Thiedmann, I. Manke, W. Lehnert and V. Schmidt: 'Random geometric graphs for modelling the pore space of fibre-based materials', *J. Mater. Sci.*, 2011, **46**, (24), 7745–7759.
242. T. E. Wilkes, S. R. Stock, F. De Carlo, X. Xiao and K. T. Faber: 'X-ray micro-computed tomography of beech wood and biomorphic C, SiC and Al/SiC composites', *Philos. Mag.*, 2009, **89**, (17), 1373–1389.
243. P. Badel, E. Maire, E. Vidal-Salle and P. Boisse: 'Mesoscopic Mechanical Analyses of Textile Composites: Validation with X-Ray Tomography', in 'Mechanics of Microstructured Solids 2: Cellular Materials, Fibre Reinforced Solids and Soft Tissues: Cellular Materials, Fibre Reinforced Solids and Soft Tissues', (eds. J. F. Ganghoffer, *et al.*), 71–78; 2010. Berlin, Springer Verlag.
244. S. R. du Roscoat, M. Decain, X. Thibault, C. Geindreau and J. F. Bloch: 'Estimation of microstructural properties from synchrotron X-ray microtomography and determination of the REV in paper materials', *Acta Mater.*, 2007, **55**, (8), 2841–2850.
245. J. C. Elliott and S. D. Dover: 'X-Ray Microtomography', *J. Microsc.*, 1982, **126**, 211–213.
246. J. A. Meganck, K. M. Kozloff, M. M. Thornton, S. M. Broski and S. A. Goldstein: 'Beam hardening artifacts in micro-computed tomography scanning can be reduced by X-ray beam filtration and the resulting images can be used to accurately measure BMD', *Bone*, 2009, **45**, (6), 1104–1116.
247. G. R. Davis and J. C. Elliott: 'X-ray microtomography scanner using time-delay integration for elimination of ring artefacts in the reconstructed image', *Nucl. Instr. Meth. A*, 1997, **394**, 157–162.
248. P. Rueggsegger, U. Elsasser, M. Anliker, H. Gnehm, H. Kind and A. Prader: 'Quantification of bone mineralization using computer tomography', *Radiology*, 1976, **121**, (1), 93–97.
249. S. E. P. Dowker, J. C. Elliott, G. R. Davis, R. M. Wilson and P. Cloetens: 'Synchrotron x-ray microtomographic investigation of mineral concentrations at micrometre scale in sound and carious enamel', *Caries Res.*, 2004, **38**, (6), 514–522.
250. D. H. Phillips and J. J. Lannutti: 'Measuring physical density with X-ray computed tomography', *NDT E Int.*, 1997, **30**, (6), 339–350.
251. N. Douarache, D. Rouby, G. Peix and J. M. Jouin: 'Relations between X-ray tomography, density and mechanical properties in carbon-carbon composites', *Carbon*, 2001, **39**, (10), 1455–1465.
252. D. Gastaldi, F. Canonico, L. Capelli, E. Boccaleri, M. Milanesio, L. Palin, G. Croce, F. Marone, K. Mader and M. Stampanoni: 'In situ tomographic investigation on the early hydration behaviors of cementing systems', *Constr. Build. Mater.*, 2012, **29**, 284–290.
253. L. Babout, P. M. Mummery, T. J. Marrow, N. Tzelepi and P. J. Withers: 'The effect of thermal oxidation on polycrystalline graphite studied by X-ray micro-tomography', *Carbon*, 2005, **43**, 765–774.
254. L. Babout, T. J. Marrow, P. M. Mummery and P. J. Withers: 'Mapping the evolution of density in 3D of thermally oxidised graphite for nuclear applications', *Scr. Mater.*, 2006, **54**, 829–834.
255. C. Berre, P. M. Mummery, B. J. Marsden, T. Mori and P. J. Withers: 'Application of a micromechanics model to the overall properties of heterogeneous graphite', *J. Nucl. Mater.*, 2008, **381**, (1–2), 124–128.
256. P. J. Withers, P. Lopez-Crespo, A. Kyrieleis and Y.-C. Hung: 'Evolution of crack-bridging and crack-tip driving force during the growth of a fatigue crack in a Ti/SiC composite', *Proc. R. Soc. A*, 2012, **468**, (2145), 2722–2743.

257. F. Tariq, R. Haswell, P. D. Lee and D. W. McComb: 'Characterization of hierarchical pore structures in ceramics using multiscale tomography', *Acta Mater.*, 2011, **59**, (5), 2109–2120.
258. L. M. Keller, P. Schuetz, R. Erni, M. D. Rossell, F. Lucas, P. Gasser and L. Holzer: 'Characterization of multi-scale microstructural features in Opalinus Clay', *Microporous Mesoporous Mat.*, 2013, **170**, 83–94.
259. P. J. Withers and P. D. Lee: 'Imaging in Four Dimensions', *Ingenia*, 2012, **51**, 40–45.
260. T. S. Smith and B. K. Bay: 'Experimental measurement of strains using digital volume correlation', in 'Nontraditional methods of sensing stress, strain and damage in materials and structures: second volume', (eds. G. F. Lucas, *et al.*), 117–126; 2001. 2001, West Conshohocken, PA: ASTM International.
261. T. S. Smith, B. K. Bay and M. M. Rashid: 'Digital volume correlation including rotational degrees of freedom during minimization', *Exp. Mech.*, 2002, **42**, (3), 272–278.
262. F. Hild and S. Roux: 'Digital image correlation: from displacement measurement to identification of elastic properties - a review', *Strain*, 2006, **42**, (2), 69–80.
263. B. K. Bay: 'Methods and applications of digital volume correlation', *J. Strain Anal. Eng. Des.*, 2008, **43**, (8), 745–760.
264. B. K. Bay, T. S. Smith, D. P. Fyhrie and M. Saad: 'Digital volume correlation: Three-dimensional strain mapping using X-ray tomography', *Exp. Mech.*, 1999, **39**, (3), 217–226.
265. S. Roux, F. Hild, P. Viot and D. Bernard: 'Three-dimensional image correlation from X-ray computed tomography of solid foam', *Compos. Part A Appl. Sci. Manuf.*, 2008, **39**, (8), 1253–1265.
266. S. Roux, J. Rethore and F. Hild: 'Digital image correlation and fracture: an advanced technique for estimating stress intensity factors of 2D and 3D cracks', *J. Phys. D Appl. Phys.*, 2009, **42**, (21), 214004.
267. H. Leclerc, J. N. Perie, S. Roux and F. Hild: 'Voxel-Scale Digital Volume Correlation', *Exp. Mech.*, 2011, **51**, (4), 479–490.
268. F. Forsberg, R. Mooser, M. Arnold, E. Hack and P. Wyss: '3D micro-scale deformations of wood in bending: Synchrotron radiation mu CT data analyzed with digital volume correlation', *J. Struct. Biol.*, 2008, **164**, (3), 255–262.
269. A. Germaneau, P. Doumalin and J. C. Dupre: 'Comparison between X-ray micro-computed tomography and optical scanning tomography for full 3D strain measurement by digital volume correlation', *NDT E Int.*, 2008, **41**, (6), 407–415.
270. M. Gates, J. Lambros and M. T. Heath: 'Towards high performance digital volume correlation', *Exp. Mech.*, 2011, **51**, (4), 491–507.
271. F. Pierron, S. A. McDonald, D. Hollis, P. J. Withers and A. Alderson: 'Assessment of the deformation of low density polymeric auxetic foams by X-ray tomography and digital volume correlation', *Appl. Mech. Mater.*, 2011, **70**, 93–98.
272. F. Hild, E. Maire, S. Roux and J. F. Witz: 'Three-dimensional analysis of a compression test on stone wool', *Acta Mater.*, 2009, **57**, (11), 3310–3320.
273. S. A. McDonald, L. C. R. Schreider, A. C. F. Cocks and P. J. Withers: 'Particle movement during the deep penetration of a granular material studied by X-ray microtomography', *Scripta Mater.*, 2006, **54**, 191–196.
274. S. A. Hall, M. Bornert, J. Desrues, Y. Pannier, N. Lenoir, G. Viggiani and P. Besuelle: 'Discrete and continuum analysis of localised deformation in sand using X-ray mu CT and volumetric digital image correlation', *Geotechnique*, 2010, **60**, (5), 315–322.
275. F. Tagliaferri, J. Waller, E. Ando, S. A. Hall, G. Viggiani, P. Besuelle and J. T. DeJong: 'Observing strain localisation processes in bio-cemented sand using X-ray imaging', *Granular Matter*, 2011, **13**, (3), 247–250.
276. S. A. McDonald, D. Harris and P. J. Withers: 'In-situ X-ray microtomography study of the movement of a granular material within a die', *Int. J. Mater. Res.*, 2012, **103**, (2), 162–169.
277. M. Bornert, J. M. Chaix, P. Doumalin, J. C. Dupre, T. D. Fournel, M. E. Jeulin, M. Moreaud and H. Moulinec: 'Mesure tridimensionnelle de champs cinématiques par imagerie volumique pour l'analyse des matériaux et des structures (in French)', *Instrum. Mes. Metrol.*, 2004, **88**, 49.
278. P. Besuelle, J. Desrues and S. Raynaud: 'Experimental characterisation of the localisation phenomenon inside a Vosges sandstone in a triaxial cell', *Int. J. Rock Mech. Min. Sci.*, 2000, **37**, (8), 1223–1237.
279. N. Lenoir, M. Bornert, J. Desrues, P. Besuelle and G. Viggiani: 'Volumetric digital image correlation applied to X-ray microtomography images from triaxial compression tests on argillaceous rock', *Strain*, 2007, **43**, (3), 193–205.
280. L. Salvo, P. Belestin, E. Maire, M. Jacquesson, C. Vecchionacci, E. Bollner, M. Bornert and P. Doumalin: 'Structure and mechanical properties of AFS sandwiches studied by *in situ* compression tests in X-ray microtomography', *Adv. Eng. Mater.*, 2004, **6**, (6), 411–415.
281. A. Seeger, U. Kertzscher, K. Affeld and E. Wellenhofer: 'Measurement of the local velocity of the solid phase and the local solid hold-up in a three-phase flow by X-ray based particle tracking velocimetry (XPTV)', *Chem. Eng. Sci.*, 2003, **58**, (9), 1721–1729.
282. D. M. Mueth, G. F. Debregeas, G. S. Karczmar, P. J. Eng, S. R. Nagel and H. M. Jaeger: 'Signatures of granular microstructure in dense shear flows', *Nature*, 2000, **406**, (6794), 385–389.
283. H. Toda, I. Sinclair, J. Y. Buffiere, E. Maire, T. Connolley, M. Joyce, K. H. Khor and P. Gregson: 'Assessment of the fatigue crack closure phenomenon in damage-tolerant aluminium alloy by *in situ* high-resolution synchrotron X-ray microtomography', *Philos. Mag.*, 2003, **83**, (21), 2429–2448.
284. S. F. Nielsen, H. F. Poulsen, F. Beckmann, C. Thorning and J. A. Wert: 'Measurements of plastic displacement gradient components in three dimensions using marker particles and synchrotron X-ray absorption microtomography', *Acta Mater.*, 2003, **51**, (8), 2407–2415.
285. C. B. Barber, D. P. Dobkin and H. T. Huhdanpaa: 'The Quickhull algorithm for convex hulls', *ACM Trans. Math. Softw.*, 1996, **22**, 469–483.
286. M. Kobayashi, H. Toda, Y. Kawai, M. Nakazawa, Y. Aoki, K. Uesugi and Y. Suzuki: 'Three-dimensional plastic strain mapping technique for X-ray micro-tomography', in 'MS&T 2010: Proceedings from the Materials Science & Technology Conference (October 17-21, 2010, Houston, Texas)', 2010, Warrendale, PA, MS&T Partner Societies, pp. 1037–1044.
287. M. Nakazawa, M. Kobayashi, H. Toda and Y. Aoki: 'Proposal of a method to analyze 3D deformation/fracture characteristics inside materials based on a stratified matching approach', *Mach. Vis. Appl.*, 2010, **21**, (5), 687–694.
288. E. Ando, S. A. Hall, G. Viggiani, J. Desrues and P. Besuelle: 'Grain-scale experimental investigation of localised deformation in sand: a discrete particle tracking approach', *Acta Geotechnica*, 2012, **7**, (1), 1–13.
289. T. J. Marrow, H. Çetinel, M. Al-Zalmah, S. MacDonald, P. J. Withers and J. Walton: 'Fatigue crack nuclei in austempered ductile cast iron', *Fatigue Fract. Engng. Mater. Struct.*, 2002, **25**, 635–648.
290. T. M. Breunig, S. R. Stock, A. Guvenilir, J. C. Elliott, P. Anderson and G. R. Davis: 'Damage in aligned-fibre SiC/Al quantified using a laboratory X-ray tomographic microscope', *Composites*, 1993, **24**, 209–214.
291. P. J. Schilling, B. P. R. Karedla, A. K. Tatiparthi, M. A. Verges and P. D. Herrington: 'X-ray computed microtomography of internal damage in fiber reinforced polymer matrix composites', *Compos. Sci. Technol.*, 2005, **65**, (14), 2071–2078.
292. P. Cloetens, M. Pateyron-Salome, J. Y. Buffiere, G. Peix, J. Baruchel, F. Peyrin and M. Schlenker: 'Observation of microstructure and damage in materials by phase sensitive radiography and tomography', *J. Appl. Phys.*, 1997, **81**, (9), 5878–5886.
293. K. I. Ignatiev, W. K. Lee, K. Fezzaa, F. De Carlo and S. R. Stock: 'Phase contrast stereometry: Fatigue crack mapping in 3D', Developments in X-ray tomography IV, *Proc. SPIE*, 2004, **5535**, 253–260.
294. K. H. Khor, J. Y. Buffiere, W. Ludwig, H. Toda, H. S. Ubhi, P. J. Gregson and I. Sinclair: 'In situ high resolution synchrotron X-ray tomography of fatigue crack closure micromechanisms', *J. Phys. Condens. Matter*, 2004, **16**, (33), S3511–S3515.
295. S. R. Stock, K. Ignatiev, G. R. Davis, J. C. Elliott, K. Fezzaa and W.-K. Lee: 'Fatigue cracks in Aluminum samples studied with X-ray phase contrast imaging and with absorption microtomography', in 'Advances in X-ray Analysis', 123–127; 2002, New York, JCPDS-International Centre for Diffraction Data.
296. P. J. Withers: '3D crack-tip microscopy: illuminating micro-scale effects on crack-tip behavior', *Adv. Eng. Mater.*, 2011, **13**, (12), 1096–1100.
297. W. Elber: 'Fatigue crack closure under cyclic tension', *Eng. Fract. Mech.*, 1970, **2**, 37–45.
298. S. R. Stock, A. Guvenilir, T. M. Breunig, J. H. Kinney and M. C. Nichols: 'Computed tomography.3. Volumetric, high-resolution X-ray-analysis of fatigue-crack closure', *JOM*, 1995, **47**, (1), 19–23.

299. A. Guvenilir and S. R. Stock: 'High resolution computed tomography and implications for fatigue crack closure modelling', *Fatigue Fract. Eng. Mater. Struct.*, 1998, **21**, (4), 439–450.
300. T. M. Breunig, J. H. Kinney and S. R. Stock: 'MicroCT (microtomography) Quantification of microstructure related to macroscopic behavior: II. Damage in Al/SiC monofilament composites tested in monotonic tension and fatigue', *Mat. Sci. Tech.*, 2006, **22**, (9), 1059–1067.
301. P. J. Withers, J. Bennett, Y.-C. Hung and M. Preuss: 'Crack opening displacements during fatigue crack growth in Ti-SiC fibre metal matrix composites by X-ray tomography', *Mat. Sci. Tech.*, 2006, **22**, 1052–1058.
302. N. Limodin, J. Rethore, J. Y. Buffiere, A. Gravouil, F. Hild and S. Roux: 'Crack closure and stress intensity factor measurements in nodular graphite cast iron using three-dimensional correlation of laboratory X-ray microtomography images', *Acta Materialia*, 2009, **57**, (14), 4090–4101.
303. N. Limodin, J. Rethore, J. Y. Buffiere, F. Hild, S. Roux, W. Ludwig, J. Rannou and A. Gravouil: 'Influence of closure on the 3D propagation of fatigue cracks in a nodular cast iron investigated by X-ray tomography and 3D volume correlation', *Acta Materialia*, 2010, **58**, (8), 2957–2967.
304. K. I. Ignatiev, G. R. Davis, J. C. Elliott and S. R. Stock: 'MicroCT (microtomography) quantification of microstructure related to macroscopic behaviour - Part I - Fatigue crack closure measured *in situ* in AA 2090 compact tension samples', *Mater. Sci. Technol.*, 2006, **22**, (9), 1025–1037.
305. A. Guvenilir, T. M. Breunig, J. H. Kinney and S. R. Stock: 'Direct observations of crack opening as a function of applied load in the interior of a notched tensile sample of Al-Li 2090', *Acta Mater.*, 1997, **45**, 1977–1987.
306. H. Toda, I. Sinclair, J. Y. Buffiere, E. Maire, K. H. Khor, P. Gregson and T. Kobayashi: 'A 3D measurement procedure for internal local crack driving forces via synchrotron X-ray microtomography', *Acta Mater.*, 2004, **52**, (5), 1305–1317.
307. K. H. Khor, J. Y. Buffiere, W. Ludwig and I. Sinclair: 'High resolution X-ray tomography of micromechanisms of fatigue crack closure', *Scripta Mater.*, 2006, **55**, (1), 47–50.
308. P. Qu, H. Toda, H. Zhang, Y. Sakaguchi, L. Qian, M. Kobayashi and K. Uesugi: 'Local crack driving force analysis of a fatigue crack by a microstructural tracking method', *Scripta Mater.*, 2009, **61**, (5), 489–492.
309. J. Rannou, N. Limodin, J. Rethore, A. Gravouil, W. Ludwig, M. C. Baitto-Dubourg, J. Y. Buffiere, A. Combescure, F. Hild and S. Roux: 'Three dimensional experimental and numerical multiscale analysis of a fatigue crack', *Comput. Meth. Appl. Mech. Eng.*, 2010, **199**, (21–22), 1307–1325.
310. H. Toda, E. Maire, S. Yamauchi, H. Tsuruta, T. Hiramatsu and M. Kobayashi: 'In situ observation of ductile fracture using X-ray tomography technique', *Acta Mater.*, 2011, **59**, (5), 1995–2008.
311. J. Rethore, J. P. Tinnes, S. Roux, J. Y. Buffiere and F. Hild: 'Extended three-dimensional digital image correlation (X3D-DIC)', *C. R. Mec.*, 2008, **336**, (8), 643–649.
312. J. Rethore, N. Limodin, J. Y. Buffiere, F. Hild, W. Ludwig and S. Roux: 'Digital volume correlation analyses of synchrotron tomographic images', *J. Strain Anal. Eng. Des.*, 2011, **46**, (7), 683–695.
313. B. Budiansky and J. C. Amazigo: 'Toughening by aligned, frictionally constrained fibres', *J. Mech. Phys. Solids*, 1989, **37**, 93–109.
314. A. Steuwer, M. Rahman, A. Shterenlikht, M. E. Fitzpatrick, L. Edwards and P. J. Withers: 'The evolution of crack-tip stresses during a fatigue overload event', *Acta Mater.*, 2010, **58**, (11), 4039–4052.
315. Y. Barranger, P. Doumalin, J. C. Dupre, A. Germaneau, S. Hedan and V. Valle: 'Evaluation of three-dimensional and two-dimensional full displacement fields of a single edge notch fracture mechanics specimen, in light of experimental data using X-ray tomography', *Eng. Fract. Mech.*, 2009, **76**, (15), 2371–2383.
316. F. Xu, L. Helfen, A. J. Moffat, G. Johnson, I. Sinclair and T. Baumbach: 'Synchrotron radiation computed laminography for polymer composite failure studies', *J. Synchrotron Radiat.*, 2010, **17**, 222–226.
317. G. P. McCombe, J. Rouse, R. S. Trask, P. J. Withers and I. P. Bond: 'X-ray damage characterisation in self-healing fibre reinforced polymers', *Compos. Part A Appl. Sci. Manuf.*, 2012, **43**, (4), 613–620.
318. J. W. Ager, G. Balooch and R. O. Ritchie: 'Fracture, aging and disease in bone', *J. Mater. Res.*, 2006, **21**, (8), 1878–1892.
319. R. K. Nalla, J. J. Kruzic, J. H. Kinney, M. Balooch, J. W. Ager and R. O. Ritchie: 'Role of microstructure in the aging-related deterioration of the toughness of human cortical bone', *Mater. Sci. Eng C Biomim Supramol. Syst.*, 2006, **26**, (8), 1251–1260.
320. P. J. Thurner, P. Wyss, R. Voide, M. Stauber, M. Stambanoni, U. Sennhauser and R. Muller: 'Time-lapsed investigation of three-dimensional failure and damage accumulation in trabecular bone using synchrotron light', *Bone*, 2006, **39**, (2), 289–299.
321. J. Kruzic, R. K. Nalla, J. H. Kinney and R. O. Ritchie: 'Crack blunting, crack bridging and resistance-curve fracture mechanics in dentin: effect of hydration', *Biomaterials*, 2003, **24**, (28), 5209–5221.
322. A. Hodgkins, T. J. Marrow, P. Mummery, B. Marsden and A. Fok: 'X-ray tomography observation of crack propagation in nuclear graphite', *Mater. Sci. Technol.*, 2006, **22**, (9), 1045–1051.
323. M. Mostafavi, S. A. McDonald, H. Çetinel, P. M. Mummery and T. J. Marrow: 'Flexural strength and defect behaviour in a quasi-brittle material (polygranular graphite) under different states of stress', *Carbon*, 2013, In press.
324. M. Mostafavi, S. A. McDonald, P. M. Mummery and T. J. Marrow: 'Observation and quantification of three-dimensional crack propagation in poly-granular graphite', *Engineering Fracture Mechanics*, Available online 12 January 2013, ISSN 0013-7944, <http://dx.doi.org/10.1016/j.engfracmech.2012.11.023>. (<http://www.sciencedirect.com/science/article/pii/S0013794413000052>).
325. J. Y. Buffiere, E. Ferrie, H. Proudhon and W. Ludwig: 'Three-dimensional visualisation of fatigue cracks in metals using high resolution synchrotron X-ray micro-tomography', *Mater. Sci. Technol.*, 2006, **22**, (9), 1019–1024.
326. J.-Y. Buffiere, N. Limodin, J. Rethore, W. Ludwig, F. Hild, A. Gravouil and S. Roux: '3D Characterisation of fatigue cracks using X-ray tomography from synchrotron to laboratory sources', in '139th Annual Meeting & Exhibition - Supplemental Proceedings, Vol 2: Materials Characterization, Computation and Modeling and Energy', 705–712; 2010, TMS. Warrendale, PA.
327. T. J. Marrow, L. Babout, B. J. Connolly, D. Engelberg, G. Johnson, J.-Y. Buffiere, P. J. Withers and R. C. Newman: 'High-resolution, *in situ*, tomographic observations of stress corrosion cracking', in 'Environment-induced cracking of metals, volume 2: Prediction, industrial developments and evaluation', edited by S. A. Shipilov et al., 2008, Amsterdam, Elsevier, pages 439–447.
328. A. King, W. Ludwig, M. Herbig, J. Y. Buffiere, A. A. Khan, N. Stevens and T. J. Marrow: 'Three-dimensional *in situ* observations of short fatigue crack growth in magnesium', *Acta Mater.*, 2011, **59**, (17), 6761–6771.
329. W. Ludwig, J. Y. Buffiere, S. Savelli and P. Cloetens: 'Study of the interaction of a short fatigue crack with grain boundaries in a cast Al alloy using X-ray microtomography', *Acta Mater.*, 2003, **51**, (3), 585–598.
330. S. Biroasca, J. Y. Buffiere, F. A. Garcia-Pastor, M. Karadge, L. Babout and M. Preuss: 'Three-dimensional characterization of fatigue cracks in Ti-6246 using X-ray tomography and electron backscatter diffraction', *Acta Mater.*, 2009, **57**, (19), 5834–5847.
331. S. Biroasca, J. Y. Buffiere, M. Karadge and M. Preuss: '3-D observations of short fatigue crack interaction with lamellar and duplex microstructures in a two-phase titanium alloy', *Acta Mater.*, 2011, **59**, (4), 1510–1522.
332. D. Gonzalez, A. King, M. Mostafavi, P. Reischig, S. R. d. Roscoat, W. Ludwig, J. Q. d. Fonseca, P. J. Withers, and T. J. Marrow: 'Three-dimensional observation and image-based modelling 3 of thermal strains in polycrystalline alumina', *Acta Materialia*, 2013, In press.
333. L. Babout, M. Janaszewski, T. J. Marrow and P. J. Withers: 'A method for the 3-D quantification of bridging ligaments during crack propagation', *Scripta Mater.*, 2011, **65**, 131–134.
334. S. Zabler, A. Rack, I. Manke, K. Thermann, J. Tiedemann, N. Harthill and H. Riesemeier: 'High-resolution tomography of cracks, voids and micro-structure in greywacke and limestone', *J. Struct. Geol.*, 2008, **30**, (7), 876–887.
335. H. Leng, X. Wang, R. D. Ross, G. L. Niebur and R. K. Roeder: 'Micro-computed tomography of fatigue microdamage in cortical bone using a barium sulfate contrast agent', *J. Mech. Behav. Biomed. Mater.*, 2008, **1**, (1), 68–75.
336. K. J. Koester, J. W. Ager and R. O. Ritchie: 'The true toughness of human cortical bone measured with realistically short cracks', *Nature Mater.*, 2008, **7**, (8), 672–677.
337. E. A. Zimmermann, E. Schaible, H. Bale, H. D. Barth, S. Y. Tang, P. Reichert, B. Busse, T. Alliston, J. W. Ager, III and R. O.

- Ritchie: 'Age-related changes in the plasticity and toughness of human cortical bone at multiple length scales', *Proc. Nat. Acad. Sci. U.S.A.*, 2011, **108**, (35), 14416–14421.
338. O. Lame, D. Bellet, M. Di Michiel and D. Bouvard: 'Bulk observation of metal powder sintering by X-ray synchrotron microtomography', *Acta Mater.*, 2004, **52**, (4), 977–984.
339. D. Bernard, D. Gendron, J. M. Heintz, S. Bordere and J. Etourneau: 'First direct 3D visualisation of microstructural evolutions during sintering through X-ray computed microtomography', *Acta Mater.*, 2005, **53**, (1), 121–128.
340. F. Xu, X. F. Hu, H. Miao and J. H. Zhao: 'In situ investigation of ceramic sintering by synchrotron radiation X-ray computed tomography', *Opt. Lasers Eng.*, 2010, **48**, (11), 1082–1088.
341. J. R. Blackford: 'Sintering and microstructure of ice: a review', *J. Phys. D Appl. Phys.*, 2007, **40**, (21), R355–R385.
342. L. Babout, E. Maire, J.-Y. Buffiere and R. Fougères: 'Characterisation by X-ray computed tomography of decohesion, porosity growth & coalescence in model metal matrix composites', *Acta Mater.*, 2001, **49**, 2055–2063.
343. C. Landron, O. Bouaziz, E. Maire and J. Adrien: 'Characterization and modeling of void nucleation by interface decohesion in dual phase steels', *Scripta Mater.*, 2010, **63**, (10), 973–976.
344. C. Landron, E. Maire, O. Bouaziz, J. Adrien, L. Lecarme and A. Bareggi: 'Validation of void growth models using X-ray microtomography characterization of damage in dual phase steels', *Acta Mater.*, 2011, **59**, (20), 7564–7573.
345. A. Weck, D. S. Wilkinson, E. Maire and H. Toda: 'Visualization by X-ray tomography of void growth and coalescence leading to fracture in model materials', *Acta Mater.*, 2008, **56**, (12), 2919–2928.
346. C. F. Martin, C. Jossierond, L. Salvo, J. J. Blandin, P. Cloetens and E. Boller: 'Characterisation by X-ray micro-tomography of cavity coalescence during superplastic deformation', *Scripta Mater.*, 2000, **42**, 375–381.
347. E. Rosenberg, N. Brusselle-Dupend and T. Epsztein: 'A mesoscale quantification method of cavitation in semicrystalline polymers using X-ray microtomography', *Mater. Sci. Eng. A Struct. Mater.*, 2011, **528**, (21), 6535–6544.
348. E. Maire, O. Bouaziz, M. Di Michiel and C. Verdu: 'Initiation and growth of damage in a dual-phase steel observed by X-ray microtomography', *Acta Mater.*, 2008, **56**, (18), 4954–4964.
349. E. Maire, S. X. Zhou, J. Adrien and M. Dimichiel: 'Damage quantification in aluminium alloys using *in situ* tensile tests in X-ray tomography', *Eng. Fract. Mech.*, 2011, **78**, (15), 2679–2690.
350. A. Borbely, K. Dzieciol, F. Sket, A. Isaac, M. di Michiel, T. Buslaps and A. R. Kaysser-Pyzalla: 'Characterization of creep and creep damage by *in situ* microtomography', *JOM*, 2011, **63**, (7), 78–84.
351. M. Huppmann, B. Camin, A. R. Pyzalla and W. Reimers: 'In-situ observation of creep damage evolution in Al-Al₂O₃ MMCs by synchrotron X-ray microtomography', *Int. J. Mater. Res.*, 2010, **101**, (3), 372–379.
352. T. S. Liu, D. G. Harlow and T. J. Delph: 'Stereological analysis of creep cavities on polished sections', *Metallography*, 1988, **21**, (1), 55–76.
353. A. Isaac, F. Sket, W. Reimers, B. Camin, G. Sauthoff and A. R. Pyzalla: 'In situ 3D quantification of the evolution of creep cavity size, shape and spatial orientation using synchrotron X-ray tomography', *Sci. Eng. A Struct. Mater.*, 2008, **478**, (1–2), 108–118.
354. R. Raj and M. F. Ashby: 'Intergranular Fracture at elevated Temperature', *Acta Metall.*, 1975, **23**, 653–666.
355. B. J. Connolly, D. A. Horner, S. J. Fox, A. J. Davenport, C. Padovani, S. Zhou, A. Turnbull, M. Preuss, N. P. Stevens, T. J. Marrow, J. Y. Buffiere, E. Boller, A. Groso and M. Stamparoni: 'X-ray microtomography studies of localised corrosion and transitions to stress corrosion cracking', *Mater. Sci. Technol.*, 2006, **22**, (9), 1076–1085.
356. L. Babout, T. J. Marrow, D. Engelberg and P. J. Withers: 'X-ray microtomographic observation of intergranular stress corrosion cracking in sensitised austenitic stainless steel', *Mat. Sci. Tech.*, 2006, **22**, 1068–1075.
357. S. P. Knight, M. Salagaras and A. R. Trueman: 'The study of intergranular corrosion in aircraft aluminium alloys using X-ray tomography', *Corros. Sci.*, 2011, **53**, (2), 727–734.
358. G. E. Thompson, T. Hashimoto, X. L. Zhong, M. Curioni, X. Zhou, P. Skeldon, P. J. Withers, J. A. Carr and A. G. Monteith: 'Revealing the three dimensional internal structure of aluminium alloys', *Surf. Interface Anal.*, 2013, doi: 10.1002/sia.5221.
359. A. King, W. Ludwig, D. Engelberg and T. J. Marrow: 'Diffraction contrast tomography for the study of polycrystalline stainless steel microstructures and stress corrosion cracking', *Rev. Metall. Cah. D Inf. Tech.*, 2011, **108**, (1), 47–50.
360. F. Witte, J. Fischer, J. Nellesen, C. Vogt, J. Vogt, T. Donath and F. Beckmann: 'In vivo corrosion and corrosion protection of magnesium alloy LAE442', *Acta Biomater.*, 2010, **6**, (5), 1792–1799.
361. J.-Y. Buffière, P. Cloetens, W. Ludwig, E. Maire and L. Salvo: 'In Situ X-ray Tomography Studies of Microstructural Evolution Combined with 3D Modeling', *MRS Bull.*, 2008, **33**, 611–619.
362. E. Maire, A. Fazekas, L. Salvo, R. Dendievel, S. Youssef, P. Cloetens and J. M. Letang: 'X-ray tomography applied to the characterization of cellular materials. Related finite element modeling problems', *Compos. Sci. Tech.*, 2003, **63**, (16), 2431–2443.
363. A. P. Roberts and E. J. Garboczi: 'Elastic properties of a tungsten-silver composite by reconstruction and computation', *J. Mech. Phys. Solids*, 1999, **47**, (10), 2029–2055.
364. F. Barbe, L. Decker, D. Jeulin and G. Cailletaud: 'Intergranular and intragranular behavior of polycrystalline aggregates. Part I: FE model', *Int. J. Plast.*, 2001, **17**, (4), 513–536.
365. K. Madi, S. Forest, M. Boussuge, S. Gailliege, E. Latate, J.-Y. Buffiere, D. Bernard and D. Jeulin: 'Finite element simulations of the deformation of fused-cast refractories based on X-ray computed tomography', *Comput. Mater. Sci.*, 2007, **39**, (1), 224–229.
366. H. Moulinec and P. Suquet: 'A fast numerical method for computing the linear and nonlinear mechanical properties of composites', *C.R. Acad. Sci. Paris II*, 1994, **318**, 1417–1423.
367. H. Moulinec and P. Suquet: 'A numerical method for computing the overall response of nonlinear composites with complex microstructure', *Comput. Methods Appl. Mech. Eng.*, 1998, **157**, 69–94.
368. J. Escoda, F. Willot, D. Jeulin, J. Sanahuja and C. Toulemonde: 'Estimation of local stresses and elastic properties of a mortar sample by FFT computation of fields on a 3D image', *Cem. Concr. Res.*, 2011, **41**, (5), 542–556.
369. A. Jean, F. Willot, S. Cantournet, S. Forest and D. Jeulin: 'Large-scale computations of effective elastic properties of rubber with carbon black fillers', *Int. J. Multiscale Comput. Eng.*, 2011, **9**, (3), 271–303.
370. S. B. Lee, R. A. Lebensohn and A. D. Rollett: 'Modeling the viscoplastic micromechanical response of two-phase materials using Fast Fourier Transforms', *Int. J. Plast.*, 2011, **27**, (5), 707–727.
371. P. L. Manning, L. Margetts, M. R. Johnson, P. J. Withers, W. I. Sellers, P. L. Falkingham, P. M. Mummery, P. M. Barrett and D. R. Raymont: 'Biomechanics of Dromaeosaurid Dinosaur claws: application of X-ray microtomography, nanoindentation and finite element analysis', *Anat. Rec. (Hoboken)*, 2009, **292**, (9), 1397–1405.
372. O. Caty, E. Maire, S. Youssef and R. Bouchet: 'Modeling the properties of closed-cell cellular materials from tomography images using finite shell elements', *Acta Mater.*, 2008, **56**, (19), 5524–5534.
373. Z. P. You and Y. Liu: 'Three-dimensional discrete element simulation of asphalt concrete subjected to haversine loading an application of the frequency-temperature superposition technique', *Road Mater. Pavement Des.*, 2010, **11**, (2), 273–290.
374. L. B. Wang, J. Y. Park and Y. R. Fu: 'Representation of real particles for DEM simulation using X-ray tomography', *Constr. Build. Mater.*, 2007, **21**, (2), 338–346.
375. G. W. Delaney, T. Di Matteo and T. Aste: 'Combining tomographic imaging and DEM simulations to investigate the structure of experimental sphere packings', *Soft Matter*, 2010, **6**, (13), 2992–3006.
376. F. Fischer, G. T. Lim, U. A. Handge and V. Altstadt: 'Numerical Simulation of Mechanical Properties of Cellular Materials Using Computed Tomography Analysis', *J. Cell. Plast.*, 2009, **45**, (5), 441–460.
377. A. P. Roberts and E. J. Garboczi: 'Elastic moduli of model random three-dimensional closed-cell cellular solids', *Acta Mater.*, 2001, **49**, (2), 189–197.
378. A. P. Roberts and E. J. Garboczi: 'Elastic properties of model random three-dimensional open-cell solids', *J. Mech. Phys. Solids*, 2002, **50**, (1), 33–55.

379. Y. M. Youssef, A. Chaijaruwanich, R. W. Hamilton, H. Nagaumi, R. J. Dashwood and P. D. Lee: 'X-ray microtomographic characterisation of pore evolution during homogenisation and rolling of Al-6Mg', *Mater. Sci. Technol.*, 2006, **22**, (9), 1087–1093.
380. R. Moreno-Atanasio, R. A. Williams and X. D. Jia: 'Combining X-ray microtomography with computer simulation for analysis of granular and porous materials', *Particuology*, 2010, **8**, (2), 81–99.
381. C. Betts: 'Benefits of metal foams and developments in modelling techniques to assess their materials behaviour: a review', *Mater. Sci. Technol.*, 2012, **28**, (2), 129–143.
382. T. Dillard, F. N'Guyen, E. Maire, L. Salvo, S. Forest, Y. Bienvenu, J. D. Bartout, M. Croset, R. Dendievel and P. Cloetens: '3D quantitative image analysis of open-cell nickel foams under tension and compression loading using X-ray microtomography', *Philos. Mag.*, 2005, **85**, (19), 2147–2175.
383. I. Jeon and T. Asahina: 'The effect of structural defects on the compressive behavior of closed-cell Al foam', *Acta Mater.*, 2005, **53**, (12), 3415–3423.
384. I. Jeon, T. Asahina, K.-J. Kang, S. Im and T. J. Lu: 'Finite element simulation of the plastic collapse of closed-cell aluminum foams with X-ray computed tomography', *Mech. Mater.*, 2010, **42**, (3), 227–236.
385. N. Michailidis, F. Stergioudi, H. Omar, D. Papadopoulos and D. N. Tsiapas: 'Experimental and FEM analysis of the material response of porous metals imposed to mechanical loading', *Colloids Surf. A Physicochem. Eng. Asp.*, 2011, **382**, (1–3), 124–131.
386. R. Singh, P. D. Lee, J. R. Jones, G. Poologasundarampillai, T. Post, T. C. Lindley and R. J. Dashwood: 'Hierarchically structured titanium foams for tissue scaffold applications', *Acta Biomater.*, 2010, **6**, (12), 4596–4604.
387. H. Toda, T. Ohgaki, K. Uesugi, M. Kobayashi, N. Kuroda, T. Kobayashi, M. Niinomi, T. Akahori, K. Makii and Y. Aruga: 'Quantitative assessment of microstructure and its effects on compression behavior of aluminum foams via high-resolution synchrotron X-ray tomography', *Metall. Mater. Trans. A*, 2006, **37A**, (4), 1211–1219.
388. C. Veyhl, I. V. Belova, G. E. Murch and T. Fiedler: 'Finite element analysis of the mechanical properties of cellular aluminium based on micro-computed tomography', *Mater. Sci. Eng. A*, 2011, **528**, (13–14), 4550–4555.
389. N. K. Bourne, K. Bennett, A. M. Milne, S. A. MacDonald, J. J. Harrigan and J. C. F. Millett: 'The shock response of aluminium foams', *Scripta Mater.*, 2008, **58**, (2), 154–157.
390. A. D. Brydon, S. G. Bardenhagen, E. A. Miller and G. T. Seidler: 'Simulation of the densification of real open-celled foam microstructures', *J. Mech. Phys. Solids*, 2005, **53**, (12), 2638–2660.
391. N. Tsafnat, N. Amanat and A. S. Jones: 'Analysis of coke under compressive loading: A combined approach using micro-computed tomography, finite element analysis and empirical models of porous structures', *Fuel*, 2011, **90**, (1), 384–388.
392. A. P. Roberts and E. J. Garboczi: 'Elastic properties of model porous ceramics', *J. Am. Ceram. Soc.*, 2000, **83**, (12), 3041–3048.
393. E. P. Rocha, R. B. Anchieta, A. C. Freitas Junior, E. O. de Almeida, P. M. Cattaneo and C. C. Ko: 'Mechanical behavior of ceramic veneer in zirconia-based restorations: a 3-dimensional finite element analysis using microcomputed tomography data.', *J. Prosthet. Dent.*, 2011, **105**, (1), 14–20.
394. G. Tozzi, Q. H. Zhang and J. Tong: '3D real-time micromechanical compressive behaviour of bone-cement interface: Experimental and finite element studies', *J. Biomech.*, 2012, **45**, (2), 356–363.
395. J. A. Elliott, A. H. Windle, J. R. Hobdell, G. Eeckhaut, R. J. Oldman, W. Ludwig, E. Boller, P. Cloetens and J. Baruchel: 'In-situ deformation of an open-cell flexible polyurethane foam characterised by 3D computed microtomography', *J. Mater. Sci.*, 2002, **37**, (8), 1547–1555.
396. S. A. McDonald, N. Ravirala, P. J. Withers and A. Alderson: 'In situ three-dimensional X-ray microtomography of an auxetic foam under tension', *Scripta Mater.*, 2009, **60**, 232–235.
397. J. G. F. Wismans, L. E. Govaert and J. A. W. Van Dommelen: 'X-Ray computed tomography-based modeling of polymeric foams: the effect of finite element model size on the large strain response', *J. Polym. Sci. B Polym. Phys.*, 2010, **48**, (13), 1526–1534.
398. M. D. Sarzynski, S. Schaefer and O. O. Ochoa: 'Microstructure-based models for multi-functional material systems', *Mech. Adv. Mater. Struct.*, 2012, **19**, (6), 421–430.
399. C. Berre, S. L. Fok, P. M. Mummery, J. Ali, B. J. Marsden, T. J. Marrow and G. B. Neighbour: 'Failure analysis of the effects of porosity in thermally oxidised nuclear graphite using finite element modelling', *J. Nucl. Mater.*, 2008, **381**, (1–2), 1–8.
400. P. Babin, G. Della Valle, R. Dendievel, N. Lassoued and L. Salvo: 'Mechanical properties of bread crumbs from tomography based Finite Element simulations', *J. Mater. Sci.*, 2005, **40**, (22), 5867–5873.
401. D. Bernard, L. Salvo and O. Nielsen: 'Permeability calculations on real Al-Cu microstructures assessed by 3D microtomography', Chapter is from - 'Modeling of Casting, Welding, and Advanced Solidification Processes X', edited by Doru Stefanescu, James Warren, Mark Jolly, and Matthew Krane, 750 pages, 2003, Warrendale, PA, TMS, 175–182; 2003.
402. D. Bernard, O. Nielsen, L. Salvo and P. Cloetens: 'Permeability assessment by 3D interdendritic flow simulations on microtomography mappings of Al-Cu alloys', *Mater. Sci. Eng. A Struct. Mater.*, 2005, **392**, (1–2), 112–120.
403. E. Plougonven, D. Bernard and N. Combaret: 'On pore space partitioning in relation to network model building for fluid flow computation in porous media', in 'Advances in computed tomography for geomaterials', 320–327; 2010, John Wiley & Sons, Inc. Hoboken, NJ, USA.
404. M. Knackstedt, C. Arns, M. Saadatfar, T. Senden, A. Sakellariou, A. Sheppard, R. Sok and W. S. H. Steininger: 'Virtual materials design: Properties of cellular solids derived from 3D tomographic images', *Adv. Eng. Mater.*, 2005, **7**, (4), 238–243.
405. C. H. Arns: 'Computation of linear elastic properties from microtomographic images: Methodology and agreement between theory and experiment', *Geophysics*, 2002, **67**, 1396.
406. E. Masad, A. Al Omari and H. C. Chen: 'Computations of permeability tensor coefficients and anisotropy of asphalt concrete based on microstructure simulation of fluid flow', *Comput. Mater. Sci.*, 2007, **40**, (4), 449–459.
407. L. Andersson, A. C. Jones, M. A. Knackstedt and L. Bergstrom: 'Permeability, pore connectivity and critical pore throat control of expandable polymeric sphere templated macroporous alumina', *Acta Mater.*, 2011, **59**, (3), 1239–1248.
408. R. C. Atwood, J. R. Jones, P. D. Lee and L. L. Hench: 'Analysis of pore interconnectivity in bioactive glass foams using X-ray microtomography', *Scripta Mater.*, 2004, **51**, (11), 1029–1033.
409. J. R. Jones, G. Poologasundarampillai, R. C. Atwood, D. Bernard and P. D. Lee: 'Non-destructive quantitative 3D analysis for the optimisation of tissue scaffolds', *Biomaterials*, 2007, **28**, (7), 1404–1413.
410. M. Loretz, E. Maire and D. Baillis: 'Analytical modelling of the radiative properties of metallic foams: Contribution of X-ray tomography', *Adv. Eng. Mater.*, 2008, **10**, (4), 352–360.
411. B. Zeghondy, E. Iacona and J. Taine: 'Determination of the anisotropic radiative properties of a porous material by radiative distribution function identification (RDFI)', *Int. J. Heat. Mass. Transf.*, 2006, **49**, (17–18), 2810–2819.
412. M. Loretz, R. Coquard, D. Baillis and E. Maire: 'Metallic foams: radiative properties/comparison between different models', *J. Quant. Spectrosc. Radiat. Transf.*, 2008, **109**, (1), 16–27.
413. M. Bai and J. N. Chung: 'Analytical and numerical prediction of heat transfer and pressure drop in open-cell metal foams', *Int. J. Therm. Sci.*, 2011, **50**, (6), 869–880.
414. L. Babout, B. J. Marsden, P. M. Mummery and T. J. Marrow: 'Three-dimensional characterization and thermal property modelling of thermally oxidized nuclear graphite', *Acta Mater.*, 2008, **56**, (16), 4242–4254.
415. I. G. Watson, P. D. Lee, R. J. Dashwood and P. Young: 'Simulation of the mechanical properties of an aluminum matrix composite using X-ray microtomography', *Metall. Mater. Trans. A*, 2006, **37A**, (3), 551–558.
416. G. Geandier, A. Hazotte, S. Denis, A. Mocellin and E. Maire: 'Microstructural analysis of alumina chromium composites by X-ray tomography and 3-D finite element simulation of thermal stresses', *Scripta Mater.*, 2003, **48**, (8), 1219–1224.
417. F. D. Silva, J. J. Williams, B. R. Muller, M. P. Hentschel, P. D. Portella and N. Chawla: 'Three-dimensional microstructure visualization of porosity and Fe-rich inclusions in SiC particle-reinforced Al alloy matrix composites by X-Ray synchrotron tomography', *Metall. Mater. Trans. A*, 2010, **41A**, (8), 2121–2128.
418. E. Totry, C. Gonzalez and J. Llorca: 'Prediction of the failure locus of C/PEEK composites under transverse compression and longitudinal shear through computational micromechanics', *Compos. Sci. Tech.*, 2008, **68**, (15–16), 3128–3136.

419. J. Ali, J. K. Farooqi, D. Buckthorpe, A. Cheyne and P. Mummery: 'Comparative study of predictive FE methods for mechanical properties of nuclear composites', *J. Nucl. Mater.*, 2009, **383**, (3), 247–253.
420. R. Sharma, P. Mahajan and R. K. Mittal: 'Fiber bundle push-out test and image-based finite element simulation for 3D carbon/carbon composites', *Carbon*, 2012, **50**, (8), 2717–2725.
421. B. M. Zhang, Z. Yang, X. Y. Sun and Z. W. Tang: 'A virtual experimental approach to estimate composite mechanical properties: Modeling with an explicit finite element method', *Comput. Mater. Sci.*, 2010, **49**, (3), 645–651.
422. T. S. You, R. K. Abu Al-Rub, M. K. Darabi, E. A. Masad and D. N. Little: 'Three-dimensional microstructural modeling of asphalt concrete using a unified viscoelastic-viscoplastic-viscous-damage model', *Constr. Build. Mater.*, 2012, **28**, (1), 531–548.
423. X. N. Zhang, C. Wan, D. Wang and L. F. He: 'Numerical simulation of asphalt mixture based on three-dimensional heterogeneous specimen', *J. Cent. South Univ. Technol.*, 2011, **18**, (6), 2201–2206.
424. E. Coleri, J. T. Harvey, K. Yang and J. M. Boone: 'Development of a micromechanical finite element model from computed tomography images for shear modulus simulation of asphalt mixtures', *Constr. Build. Mater.*, 2012, **30**, 783–793.
425. Q. Dai: 'Two- and three-dimensional micromechanical viscoelastic finite element modeling of stone-based materials with X-ray computed tomography images', *Constr. Build. Mater.*, 2011, **25**, (2), 1102–1114.
426. M. Milesi, P. O. Bouchard, P. H. Cornuault, Y. Chastel, M. Bernacki and E. Hachem: 'Advanced numerical method for generation of three-dimensional particles and its application in microstructure-based simulation of fatigue behavior', *Comput. Mater. Sci.*, 2011, **50**, (10), 2836–2847.
427. E. Padilla, V. Jakkali, L. Jiang and N. Chawla: 'Quantifying the effect of porosity on the evolution of deformation and damage in Sn-based solder joints by X-ray microtomography and microstructure-based finite element modeling', *Acta Mater.*, 2012, **60**, (9), 4017–4026.
428. D. Fuloria and P. D. Lee: 'An X-ray microtomographic and finite element modeling approach for the prediction of semi-solid deformation behaviour in Al-Cu alloys', *Acta Mater.*, 2009, **57**, (18), 5554–5562.
429. E. Ferrie, J. Y. Buffiere, W. Ludwig and A. Gravouil: 'X-ray micro-tomography coupled to the extended finite element method to investigate microstructurally short fatigue cracks', *Mater. Struct. Micromech. Fract.*, 2008, **567–568**, 301–304.
430. A. Stenon, A. Fazekas, J. Y. Buffiere, A. Vincent, P. Daguier and F. Merchi: 'A new methodology based on X-ray micro-tomography to estimate stress concentrations around inclusions in high strength steels', *Mater. Sci. Eng. A Struct. Mater.*, 2009, **513–14**, 376–383.
431. N. Moulin, D. Jeulin and H. Klocker: 'Stress concentrations in non-convex elastic particles embedded in a ductile matrix', *Int. J. Eng. Sci.*, 2009, **47**, (2), 170–191.
432. C. Berre, S. L. Fok, B. J. Marsden, P. M. Mummery, T. J. Marrow and G. B. Neighbour: 'Microstructural modelling of nuclear graphite using multi-phase models', *J. Nucl. Mater.*, 2008, **380**, (1–3), 46–58.
433. M. A. S. Qidwai, A. C. Lewis and A. B. Geltmacher: 'Using image-based computational modeling to study microstructure-yield correlations in metals', *Acta Mater.*, 2009, **57**, (14), 4233–4247.
434. A. C. Lewis and A. B. Geltmacher: 'Image-based modeling of the response of experimental 3D microstructures to mechanical loading', *Scripta Mater.*, 2006, **55**, (1), 81–85.
435. D. Cedat, O. Fandeur, C. Rey and D. Raabe: 'Polycrystal model of the mechanical behavior of a Mo-TiC30 vol.% metal-ceramic composite using a three-dimensional microstructure map obtained by dual beam focused ion beam scanning electron microscopy', *Acta Mater.*, 2012, **60**, (4), 1623–1632.
436. K. Haldrup, F. Beckmann, S. F. Nielsen and J. A. Wert: 'Experimental determination of strain partitioning among individual grains in the bulk of an aluminium multicrystal', *Mater. Charact.*, 2008, **59**, (7), 842–851.
437. N. Zaafarani, D. Raabe, F. Roters and S. Zaeferrer: 'On the origin of deformation-induced rotation patterns below nanoincidents', *Acta Mater.*, 2008, **56**, (1), 31–42.
438. D. Gonzalez, J. F. Kelleher, J. Q. da Fonseca and P. J. Withers: 'Macro and intergranular stress responses of austenitic stainless steel to 90 degrees strain path changes', *Mater. Sci. Eng. A Struct. Mater.*, 2012, **546**, 263–271.
439. L. Wang, R. I. Barabash, Y. Yang, T. R. Bieler, M. A. Crimp, P. Eisenlohr, W. Liu and G. E. Ice: 'Experimental Characterization and Crystal Plasticity Modeling of Heterogeneous Deformation in Polycrystalline alpha-Ti', *Mater. Sci. Eng. A Struct. Mater.*, 2011, **42A**, (3), 626–635.
440. I. Simonovski, L. Cizelj, T. J. Marrow, J. Q. da Fonseca and A. King: 'Towards modelling intergranular stress-corrosion cracks using experimentally obtained grain topologies', in 'Asme Pressure Vessels and Piping Conference 2009, Vol. 3: Design and Analysis', 543–550; 2009. New York, ASME.
441. I. Simonovski and L. Cizelj: 'Computational multiscale modeling of intergranular cracking', *J. Nucl. Mater.*, 2011, **414**, (2), 243–250.